Doctoral Dissertation

博士論文

Shear Rate-dependent Behaviors and Decomposition Characteristics of Methane Hydrate-bearing Sediments

（メタンハイドレート胚胎砂のせん断速度依存挙動および分解特性）

September 2021

2021 年 9 月

Qi Wu

山口大学大学院創成科学研究科

Graduate School of Sciences and Technology for Innovation,
Yamaguchi University

Content

Abstract

The development of society has increased the demand for energy consumption year by year, and the exploitation and utilization of new energy are urgent and necessary. At present, a large number of natural gas hydrates have been found in permafrost and marine sediments around the world. It has been estimated that the carbon content in the natural gas hydrate is about twice the sum of the carbon content in all currently proven fossil fuels (including coal, oil, and natural gas), so it is a promising energy resource in the future. The ultimate aim of this thesis is to provide an experimental basis for the realization of safe and efficient exploitation of natural gas hydrate.

Firstly, before realizing the safe exploitation of natural gas hydrate, it is necessary to study the influence mechanism of different factors on the mechanical properties of hydrate-bearing sediments by the laboratory's mechanical experiments. Sediments have various stress conditions in the natural gas hydrate reservoir. However, most of the current studies about the mechanical properties of hydrate-bearing sediments under general stress conditions and then established corresponding constitutive models. The failure of hydrate-bearing sediments under plane strain conditions is always accompanied by significant local strain and eventually formed a clear shear band. Even under the same experimental conditions, the stress-strain relationship of hydrate-bearing sediments is different in the triaxial shear and plane strain shear experiments. Moreover, the local strain may cause changes in the local permeability of the reservoir, which can also affect the gas production efficiency. As in the plane strain experiment, the failure of the specimen is affected by the development of the shear band. In particular, the angle and thickness of the shear band are considered to be related to the strength of the specimen. The study of the development of the shear band is helpful to understand the development process of the shear band in different

stress-strain stages and to establish the relationship between the development of the shear band and the stress-strain in the future.

Secondly, to the long-term accurate prediction of the changes in the mechanical properties of natural gas hydrate reservoirs, the time dependence of hydrate-bearing sediments must also be considered. The shear rate dependence experiment is an effective method to study the time dependence of materials, but only a few relevant research results have been reported. The shear rate dependence characteristics of the hydrate-bearing sediments under plane strain conditions have also been studied in this thesis. The research results will help to introduce time parameters into the constitutive model of hydrate sediments in the future, and then achieve long-term accurate prediction of the mechanical characteristics of natural gas hydrate reservoirs.

Finally, understanding the decomposition characteristics of hydrates in the sand is the basis for developing methods to improve gas production efficiency. Therefore, the effect of the content of fine particles on the decomposition characteristics of hydrates in the sand under local thermal stimulation conditions has been studied firstly. And then considering the mechanical properties of the reservoir are closely related to the decomposition properties of hydrates, under different stress conditions, the stress-strain relationship of hydrate-bearing sediments and the decomposition characteristics of hydrates during local thermal stimulation and depressurization have been studied. The experimental results are helpful to understand the interaction mechanism between the decomposition of hydrates and the stress-strain behavior of sediments under different conditions.

The content of this thesis as follows:

In chapter 1, the research background about the natural gas hydrate has been introduced. The current exploitation progress of natural gas hydrate and the related problems were also reviewed.

And then the mechanical properties and the decomposition characteristics of hydrate-bearing sediments have been discussed. Finally, the aim and organization of this thesis were shown.

In chapter 2, it has shown the image information and some basic physical properties of the experimental materials that used in this thesis. And then, with the plane strain shear tests on the host sand and hydrate-bearing sediment, the development of the shear band has been studied.

In chapter 3, the shear rate-dependent characteristics of hydrate-bearing sediments have been studied. After confirming that hydrate-bearing sediment also has shear rate-dependent characteristics under plane strain conditions, three different shear rates have been selected to study the effects of hydrate saturation and fines content on shear rate dependence.

In chapter 4, the decomposition of hydrate in sands has been studied. Firstly, the decomposition characteristics of hydrate-bearing sediments with different fine particle contents by local thermal stimulation were researched. And then, combined with different stress conditions, the decomposition characteristics of hydrate in the sediments by local thermal stimulation and depressurization have been studied.

In chapter 5, the summary of this thesis and future work has been shown.

Chapter 1 Introduction and literature reviews

1. Introduction

Energy consumption is increasing year by year with the development of society, while traditional fossil energy still occupies the leading position of the world's energy structure, the development and utilization of new energy resources is urgent and necessary [*Chong, Z. R et al*., 2016a].

After the discovery of a large number of natural gas hydrates that exist in permafrost and marine sediments were reported, more and more related researches have been studied [*Sloan, E. D*. 1998]. The natural gas hydrate has been considered a promising energy resource. However, disputes about the environmental impact, engineering problems, and geological disaster risks of the exploitation of natural gas hydrate also cannot be ignored.

The exploitation of natural gas hydrates is accompanied by engineering and geological risks [*Lijith, K et al*., 2019]. The decomposition of natural gas hydrates may cause uneven settlement of the seafloor, which in turn triggers submarine landslides. Changes in the stress conditions of natural gas hydrate reservoirs may also cause engineering accidents such as wellbore instability. Besides, the massive uncontrollable decomposition of natural gas from the reservoirs that enter the ocean and atmosphere will damage the marine ecological environment and the atmospheric ozone layer. Therefore, it is particularly important to study the mechanical properties of natural gas hydrate-bearing sediments and to accurately predict the mechanical behavior of natural gas hydrate reservoirs during exploitation activities.

On the other hand, traditional exploitation technologies cannot be directly applied to the exploitation activities of natural gas hydrate resources. Some new exploitation methods, such as depressurization method, thermal stimulation method, and inhibitor injection method, have been proposed [*Chong, Z. R et al*., 2016a]. All of these methods require the natural gas hydrate to be decomposed in the reservoir before the natural gas resources are extracted. The decomposition of natural gas hydrate in the reservoir and the migration of decomposed gas and water are needed to be studied to improve the efficiency of natural gas hydrate exploitation. At present, there is still a big gap between the exploitation rate of natural gas hydrate and commercial requirements. Depressurization is an economical exploitation method, while thermal stimulation can increase the rate of natural gas hydrate production. Studying the decomposition characteristics of hydrates in sediments under different test conditions is the basis for the development of efficient methods for the exploitation of natural gas hydrates.

In this chapter, section 2 introduces the research background of this research. The natural gas hydrate, the exploitation of natural gas hydrate, the mechanical properties of hydrate-bearing sediments, and the decomposition characteristics of hydrate sediments are explained in detail. Section 3 shows the aim and organization of this thesis.

2. Research background

2.1 Natural gas hydrate

Figure 1-1. The image of NGH [*Siažik et al.*, 2017; *Macdonald et al*., 2005; *Winters et al*., 2011; *Miller et al*., 2015; *Zhang et al*., 2015; *Xie, Y et al*., 2020].

Natural gas hydrate (NGH), also referred to as fiery ice, is a clathrate crystal formed by gas (mainly methane gas) and water at low temperature and high pressure [*Sloan*, 1998]. **Figure 1-1** shows the image of NGH. **Figure 1-2** shows the crystal structure of methane gas hydrate. Methane gas molecules and water form a cubic structure, there are two dodecahedron and six tetradecahedron (12 pentagonal faces and two hexagonal faces) water cage structures in each unit cell ($5^{12}6^2$). Methane gas molecules are located in the cage structure composed of water molecules. The general composition of methane gas hydrate is $CH_4 \cdot 5.75H_2O$, that is, one mole of methane hydrate is composed of one mole of methane and 5.75 moles of water, but this ratio depends on the number of methane molecules in the various cage structures of the water lattice. As shown in **Figure 1-3**, one cubic meter of methane hydrate can be decomposed into 168 cubic meters of methane gas at a standard state (273.15 K and 1 atm).

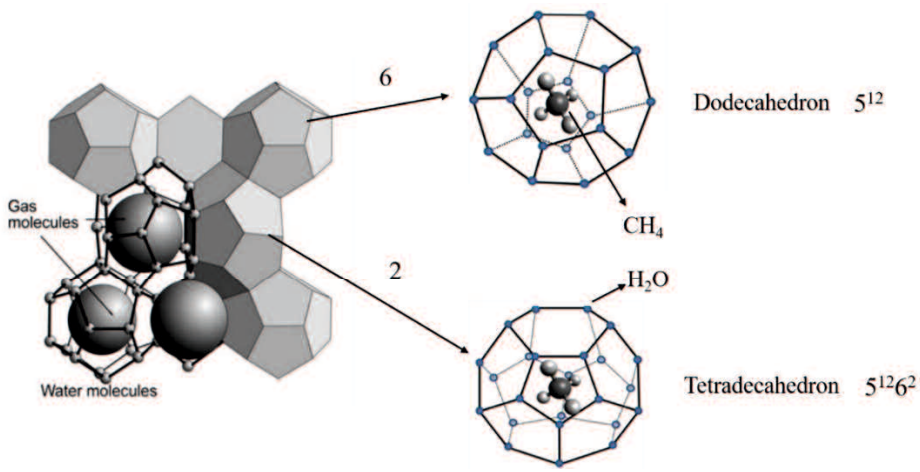

Figure 1-2. The crystal structure of methane gas hydrate (modified from [*Bohrmann and Torres*, 2006] and [*Palodkar and Jana*, 2019]).

The stable existence of natural gas hydrate requires a low-temperature and high-pressure environment, and a large amount of natural gas hydrate has been found in permafrost and marine sediments around the world. **Figure 1-4** shows the temperature and pressure conditions in the areas where permafrost and seabed NGH are stable. Compared with methane hydrate, NGH (mixed hydrate) can remain stable with higher temperature and lower pressure, so NGH exists in a wider area whether in permafrost or deep seabed sediments.

NGH distribution area is shown in **Figure 1-5**. It can be seen that a large amount of natural gas hydrate exists in marine sediments [*Klauda and Sandler*, 2005]. It has been reported that the NGH in the deep sea marine sediments is estimated to outnumbers that in the permafrost by more than 2 orders of magnitude. Natural gas resources contained in NGH are about 1000 to 5000 trillion cubic meters [*Chong et al.*, 2016a]. **Figure 1-6** compares the estimated amounts of different resources, it can be seen that NGH is a future energy resource with considerable reserves.

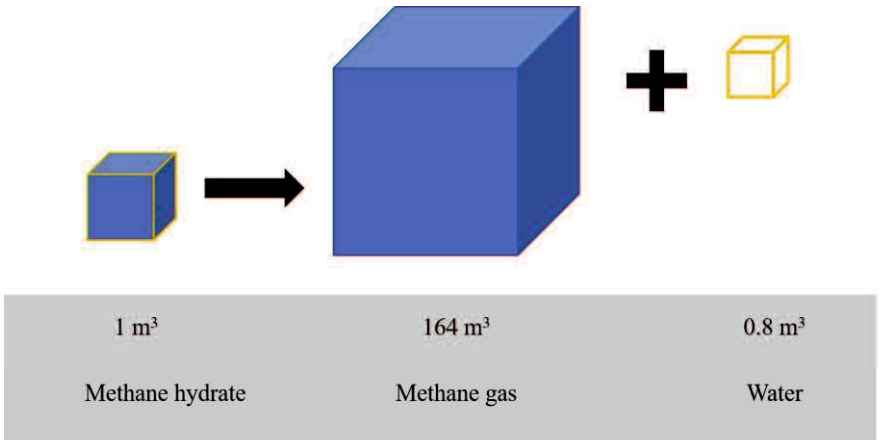

Figure 1-3. One cubic meter of methane hydrate contains about 164 cubic meters of methane gas at a standard state (modified from [*Kvenvolden*, 1993]).

At present, with the rapid development of society, the consumption of energy is increasing year by year, and the energy demand is also increasing. NGH is a low-carbon, renewable and clean energy. It burns fully and does not leave behind pollutants. Exploit NGH resources safely, efficiently, and sustainably is very meaningful and necessary.

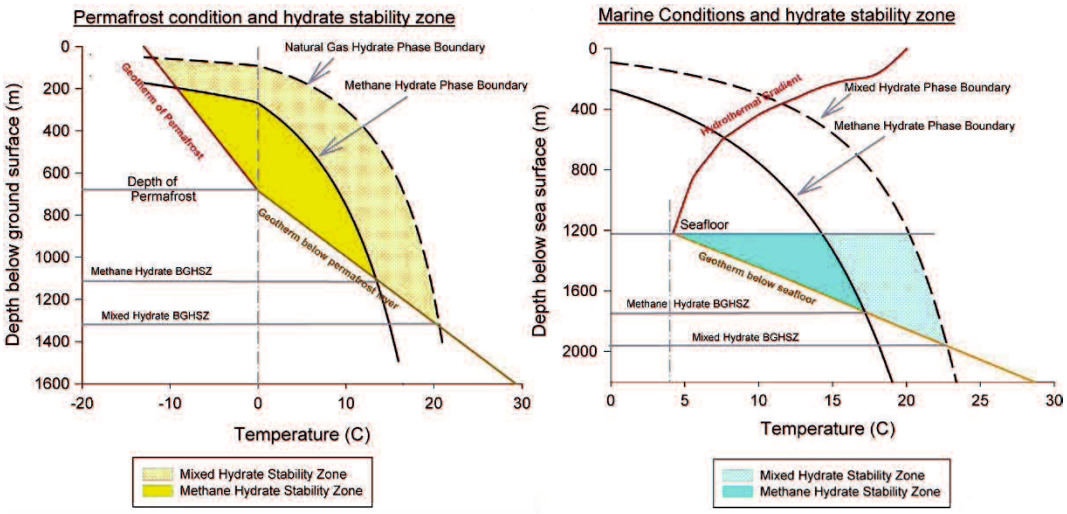

Figure 1-4. Permafrost and marine conditions and hydrate stability zone ([*Sloan* .,2008; *Holder et al* ., 1984; *Birchwood et al*., 2005; *Chong et al.*, 2016a]).

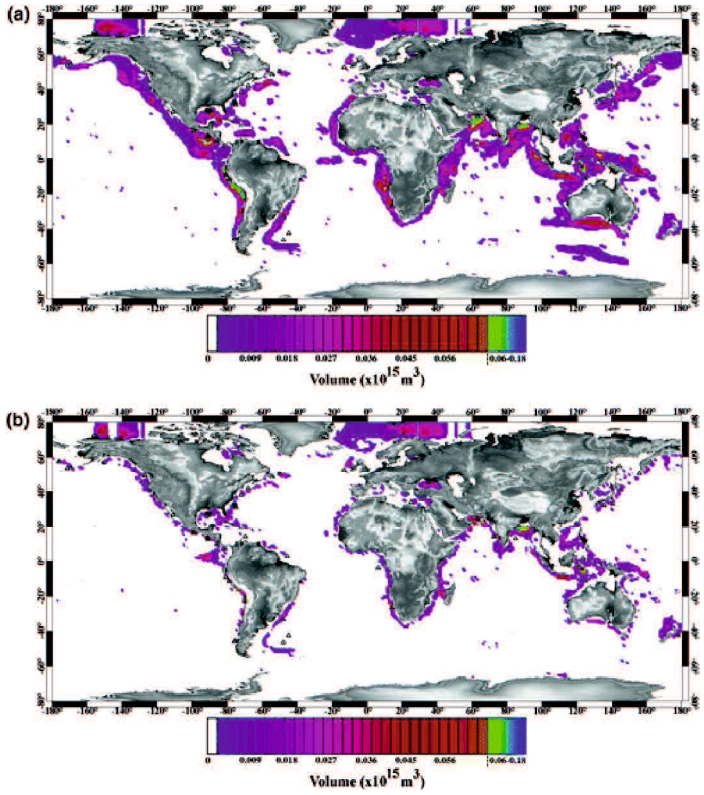

Figure 1-5. Global volume distribution of methane in the natural gas hydrate. (a) all seafloor locations; (b) seafloor depths of < 3000 m ([*Klauda and Sandler*, 2005]).

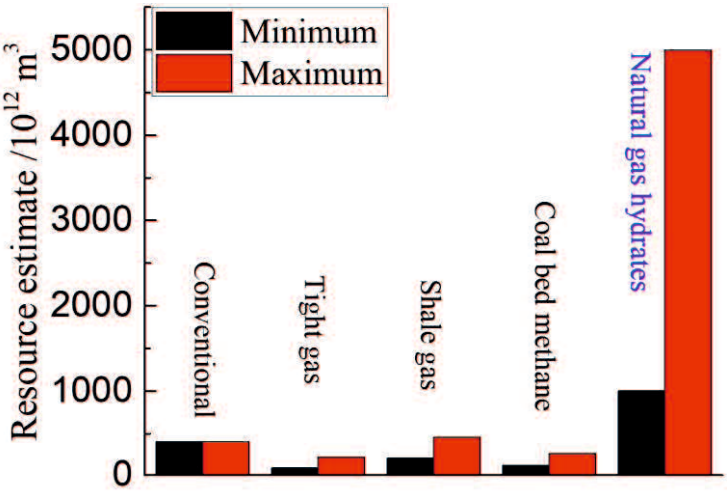

Figure 1-6. Summary of resource estimates (Modified from [*Chong et al.*, 2016a]).

2.2 Exploitation of natural gas hydrate

Due to the specific geological conditions of NGH reservoirs, traditional exploitation methods for fossil energy cannot fully satisfy the successful exploitation of NGH. Some new exploitation methods have been proposed to obtain natural gas from the NGH reservoirs. At present, there four different methods have been most discussed: depressurization method, thermal stimulation method, chemical inhibitor injection method, and gas (carbon dioxide) replacement method [*Xu and Li*, 2015]. **Figure 1-7** shows the schematic diagram of different proposed NGH exploitation methods.

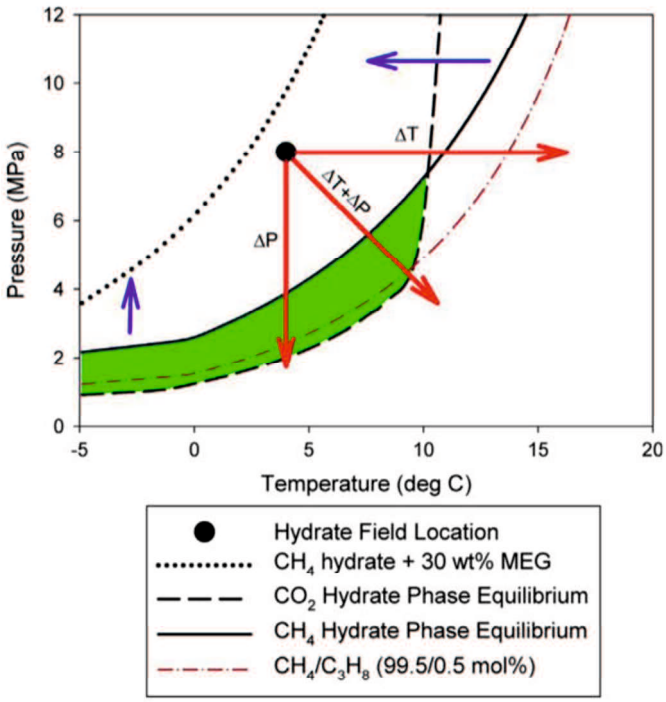

Figure 1-7. The schematic diagram of different proposed NGH exploitation methods [*Chong et al.*, 2016a]. (MEG is the abbreviation name of the inhibitor: mono-ethylene glycol)

The depressurization method has been considered to be a mostly economic exploitation method [*Moridis et al.*, 2009]. **Figure 1-8** (left) shows the principle diagram of the depressurization method. NGH usually exists in the marine sediments at a depth of several hundred meters to

several kilometers below the seafloor. By reducing the pressure of the NGH reservoir, the NGH can be decomposed directly, and then extract the natural gas from the production wellbore at the same time. The biggest advantage of the depressurization method is that it does not require continuous excitation, and it is suitable for large-area NGH exploitation at a low cost. On the other hand, this method has some special requirements for the geological environment of NGH reservoirs. For example, when the NGH reservoir with low permeability and the temperature-pressure conditions are far away from the phase equilibrium line of NGH, the depressurization method is no longer economical. Furthermore, it cannot meet the requirements of sustainable and efficient production of the NGH. Finally, the depressurization method changes the pressure conditions for the NGH reservoirs, so that the decomposition of the NGH may more easily cause geological disasters such as irregular submarine subsidence and submarine landslides.

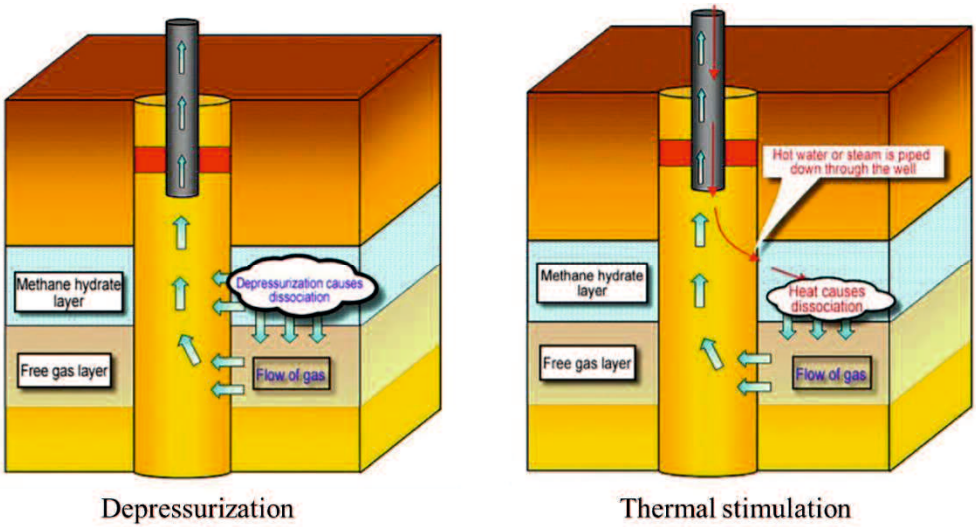

Figure 1-8. The schematic diagram of depressurization and thermal stimulation mehtods[*Cui et al.*, 2019].

The principle diagram of the thermal stimulation method is shown in **Figure 1-8** (right). This method can increase the temperature of the NGH reservoirs and then increase the decomposition efficiency of NGH. At present, a variety of thermal stimulation ideas have been reported such as

heat fluid injection [*Li et al.*, 2008; *Sakamoto et al.*, 2004], electromagnetic heating [*Wang et al.*, 2018a], microwave heating [*He et al.*, 2010], etc. The thermal stimulation method improves the decomposition efficiency of NGH without greatly changing the pressure condition of the reservoirs. It is very important for the efficient exploitation of NGH. However, the biggest problem of the current thermal stimulation method is that it does not solve the problem of heat utilization efficiency well, and more related research needs to be done.

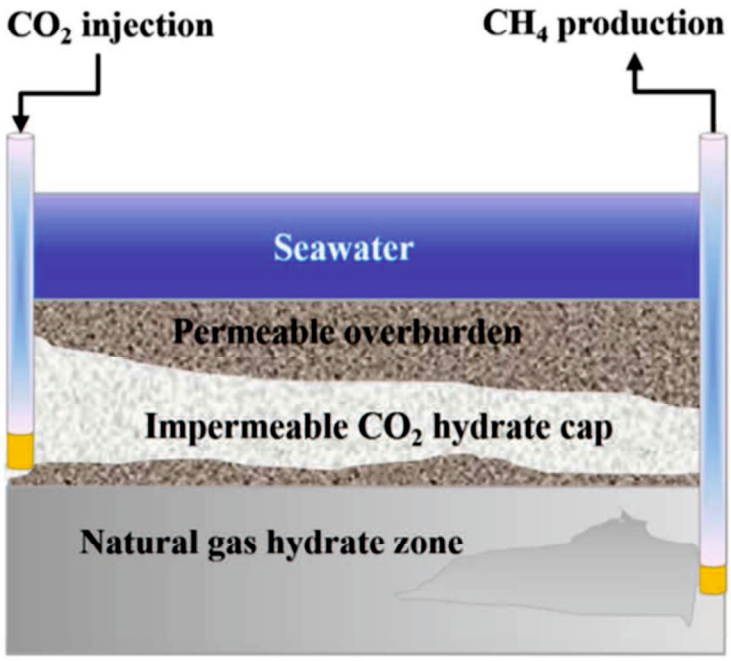

Figure 1-9. The schematic diagram of the carbon dioxide replacement method ([*Sun et al.*, 2019]).

The chemical inhibitor injection method is always combined with the thermal stimulation or pressurization method, which is essentially a means to improve the decomposition efficiency of NGH [*Urdahl et al.*, 1995]. As shown in **Figure 1-7**, carbon dioxide hydrate and methane gas hydrate have different phase equilibrium curves. Under the same temperature conditions, the pressure required for methane gas hydrate to remain stable is higher than that of carbon dioxide hydrate. Therefore, under certain conditions of temperature and pressure, while methane gas

hydrate is decomposed, carbon dioxide hydrate can be formed and remain stable. **Figure 1-9** shows the schematic diagram of the carbon dioxide replacement method. The disadvantage of this method is that it will increase the expenditure, and the inhibitor may cause environmental pollution. **Table 1-1** summarized the advantages and disadvantages of different exploitation methods.

Table 1-1. The advantages and disadvantages of different exploitation methods[*Rossi et al.*, 2019; *Yang et al.*, 2017].

Method	Advantages	Shortcomings
Thermal stimulation	Can recycling Fast effect	Efficiency is low Only local heating
Depressurization	Don't need a continuous trigger Low cost Suitable for large-scale mining	Tempreature limitations Located in the pressure balance boundary
Inhibitor injection	Can reduce the initial energy input	Cost is expensive Slow Pollute the environment
Gas replacement	Deposit stability Carbon dioxide storage	Efficiency is low

Table 1-2. Summary of filed production tests of NGH[*Jianliang*, 2020; *Yin et al.*, 2018].

Location	Time	Method	Production duration (day)	Cumulative gas production volume (m^3)	Average gas production rate (m^3/day)
Mallik (Permafrost)	Mar 2002	Thermal stimulation	5	515	103
	Apr 2007	Depressurization	1	830	830
	Mar 2008	Depressurization	5.5	13,200	2400
Ignik Sikumi (Permafrost)	May 2012	Gas replacement	38	24,210	637
Nankai Trough (Marine)	Jan 2013	Depressurization	6	120,000	20,000
	April 2017	Depressurization	12	35,000	2917
	June 2017	Depressurization	24	200,000	8333
Shenhu Area (Marine)	May 2017	Depressurization	60	300,000	5000
	April 2020	Depressurization	30	861,400	28,700

Some exploitation methods have been applied in the field production tests of NGH, and successfully obtained the natural gas. **Table 1-2** summarizes the current NGH field production tests, it can be found that the depressurization method has been widely adopted. At the same time, it must be noted that the current exploitation efficiency is still far from the requirements (340,000 m^3/day) of commercial exploitation [*Sloan Jr*, 2003]. **Figure 1-10** shows the proposed road map of different countries for the development of NGH resources. It can be seen that long-term field production tests and commercial production have been put on the agenda. However, before that, some necessary research needs to be done to ensure that the NGH can be exploited efficiently and safely. Next, the research progress of these two points will be explained separately.

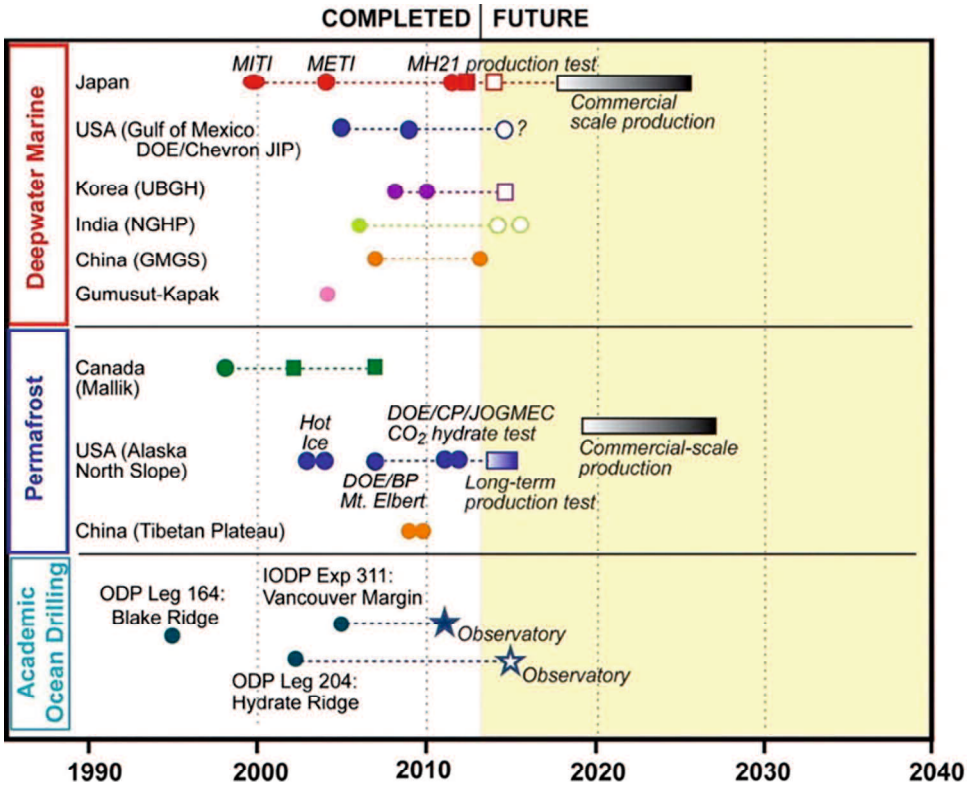

Figure 1-10. The proposed road map of different countries for the development of NGH resources[map courtesy of the US Geological Survey; *Chong et al.*, 2016a].

2.3 Mechanical properties of hydrate-bearing sediments

The success of different exploitation methods in field production tests has verified the possibility of large-scale commercial exploitation of natural gas hydrate resources. However, due to the special geological environment of NGH reservoirs, the exploitation of NGH may cause a series of geological disasters. The realization of commercial exploitation requires a deeper understanding of the mechanical properties of hydrate-bearing sediments to ensure the safety of exploitation. **Table 1-3** lists some of the risks associated with the exploitation of NGH. To avoid the risk of exploitation activities, laboratory experiments and numerical calculations of the mechanical properties of hydrate-bearing sediments are necessary.

Table 1-3. Hydrate exploitation risks [*Yang et al.*, 2017].

Accident	Consequence	Cause
Block pipeline Kill line	Pipeline pressure-out affect production	Gather temperature-pressure field changes in hydrate
Block subsea blowout preventer	Well control problems	Gather temperature-pressure field changes in hydrate
Destroy the guide base and subsea production equipment	Drilling rig equipment damage	Cold work
Deep thermal fluid into the shalllow hydrate formation	Decomposition to kick or lost circulation	Drilling interzone
Decomposition result in borehole wall instability	Hole enlargement, casing deformation, flattening, wellhead wellhead wellhead settlement, even wall collapsed	The drilling result in hydrate decomposition is out of control
Hydrate change drilling fluid wall-building properties	Cause blowout and sidewall instability	Reduce annulus pressure decomposition

2.3.1 Laboratory experiments

The low-temperature and high-pressure triaxial shear apparatus are widely used to study the mechanical properties of methane hydrate-bearing sediments, and through which the effects of many different test conditions have been studied.

Hyodo et al., [2013] conducted a series of triaxial shear tests on synthetic methane hydrate-bearing sediments. It has been found that the increase in methane hydrate saturation increased the

stiffness and shear strength of the hydrate-bearing sediments, and a high hydrate saturation also resulted in the more significantly shear dilation behavior. Besides, the stiffness and failure strength of the hydrate-bearing sediments were also increased under a higher effective confining pressure or lower temperature. *Wang et al*., [2017] conducted triaxial shear tests with different effective confining pressures on hydrate-bearing sediments obtained from the Pearl River Mouth of China. The test results showed that the shape of the stress-strain curves of all samples can be described by hyperbolic. During the shearing process, the hydrate-bearing sediments exhibited three different stages: elastic, elastic-plastic, and the end plastic stage.

There are some studies [*Li et al*., 2018; *Soga et al.*, 2006; *Waite et al.*, 2009; *Yun et al.*, 2007] that found that the effect of the methane hydrate on the mechanical properties of hydrate-bearing sediments was different with the range of the hydrate saturation. **Figure 1-11** shows the possible mechanisms controlling the stiffness and shear strength of hydrate-bearing sediments. It can be found that when the hydrate saturation was very low, hydrate particles mostly existed in the pores of sediment particles. By preventing the relative movement of the sediment particles, the hydrate can slightly increase the shear strength of the hydrate-bearing sediments. When the hydrate saturation was between 25% and 40%, the hydrate not only existed between the pores of the sediment particles but also a small amount of hydrate was attached to the surface of the particles. In this case, the effect of hydrate on the shear strength of hydrate-bearing sediments was more significant. Furthermore, during the shear test, the hydrate on the surface of the sediment particles was detached, and the hydrate particles in the pores may also be crushed, which then resulted in the dilation behaviors. When the hydrate saturation was very high, such as 80%, the hydrate formed a new structure around the sediment particles, which wrapped the sediment particles. In this case, the stiffness and shear strength of the hydrate-bearing sediments were increased significantly [*Lijith et al.*, 2019; *Waite et al.*, 2009; *Yun et al.*, 2007].

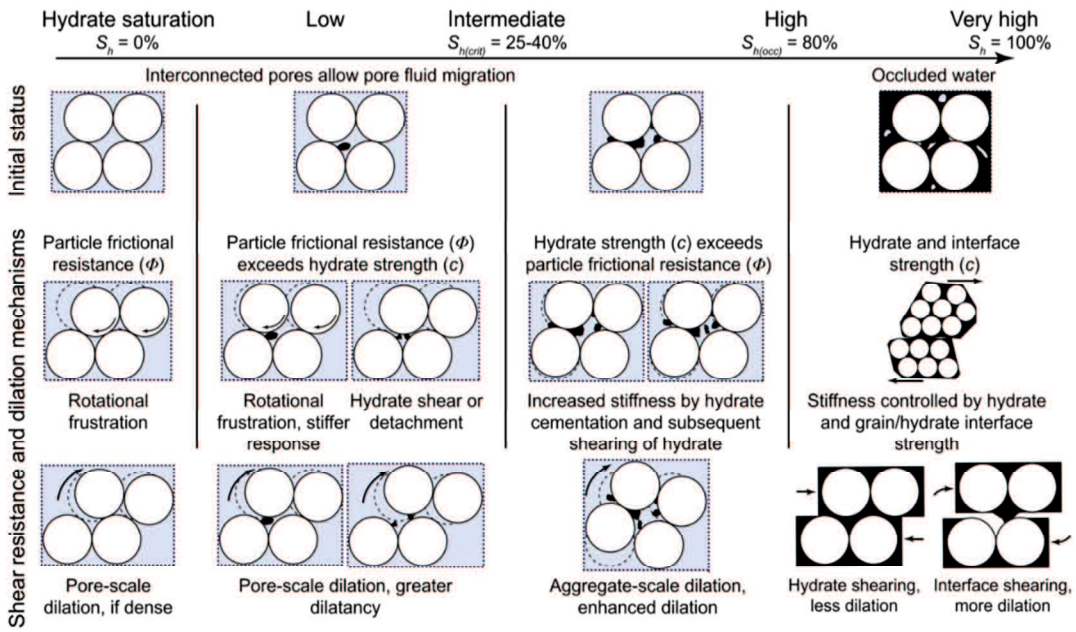

Figure 1-11. Possible mechanisms controlling the stiffness and shear strength of hydrate-bearing sediments [*Waite et al.*, 2009].

The content of fine particles and the shape of sediment particles also affected the mechanical properties of methane hydrate-bearing sediments [*Hyodo et al.*, 2015; *Hyodo et al.*, 2017; *Kajiyama et al.*, 2017]. Current marine core NGH sample analysis showed that NGH reservoirs have unique characteristics in different locations, Such as the different particle size distribution and hydrate saturation [*Yamamoto*, 2015; *J. Yoneda et al.*, 2017; *J. Yoneda et al.*, 2018].

More importantly, through triaxial shear tests on synthetic and cored NGH samples, it was found that the mechanical properties of hydrate-bearing sediments have significantly time dependence characteristics. For example, the stiffness and shear strength of methane hydrate-bearing sediments increased with the increase of the shear rate [*Iwai et al.*, 2018; *Miyazaki et al.*, 2017; *Miyazaki et al.*, 2011; *J. Yoneda et al.*, 2018]. At present, there is no uniform standard for mechanical testing of hydrate-bearing sediments, and the shear rates adopted by different researchers are not consistent. Systematic research on the shear rate dependence of hydrate-

bearing sediments can improve the accuracy of the prediction of the geomechanical behavior of NGH reservoirs.

However, there are few studies on the time-dependent behavior of the mechanical characteristics of hydrate-bearing sediments, and most of the experimental conditions were under triaxial undrained conditions. Some geological disasters, such as submarine landslides, are plane strain problems and testing under plane strain conditions has been considered important in the study of geomechanical problems [*Alshibli and Sture*, 2000]. Therefore, studying different conditions under plane strain conditions, such as different fine particle content (different particle size distribution), hydrate saturation, is very important for the understanding of the shear rate dependence properties of hydrate-bearing sediments.

2.3.2 Numerical calculation

Numerical calculation or simulation is an important and efficient means to predict the mechanical behavior of the reservoir to design a safer and more efficient production strategy.

The models based on Mohr-Coulomb or Duncan-Chang theory, as well as the Critical State models, have been revised to suit the description of the mechanical behavior of hydrate-bearing sediments. Some assumptions have been proposed to simplify or describe the stress-strain characteristics of hydrate-bearing sediments, and all of them have some limitations. **Table 1-4** lists the assumptions and limitations of different models [*Klar et al.*, 2010; *Lijith et al.*, 2019; *Lin et al.*, 2015; *Miyazaki et al.*, 2012; *Pinkert*, 2017; *Uchida et al.*, 2012; *Yu et al.*, 2011].

Mohr-Coulomb is a very classic theory describing the shear strength of soils. The models based on this theory require relatively few parameters and are easily obtained from the triaxial shear test. The problem is that this model incorporates the volumetric yielding of hydrate-bearing

sediments and the changes in the cementation between hydrate and sediment particles during the shearing process. **Figure 1-12** shows the calculation based on the Mohr-Coulomb model and experimental stress-strain results of hydrate-bearing sediments. It can be seen that the Mohr-Coulomb model can well describe the stiffness and the peak shear strength of the hydrate-bearing sediments changing with the hydrate saturation. However, the stress and strain in the elastic and plastic phases are in a simple linear relationship, which is inconsistent with reality.

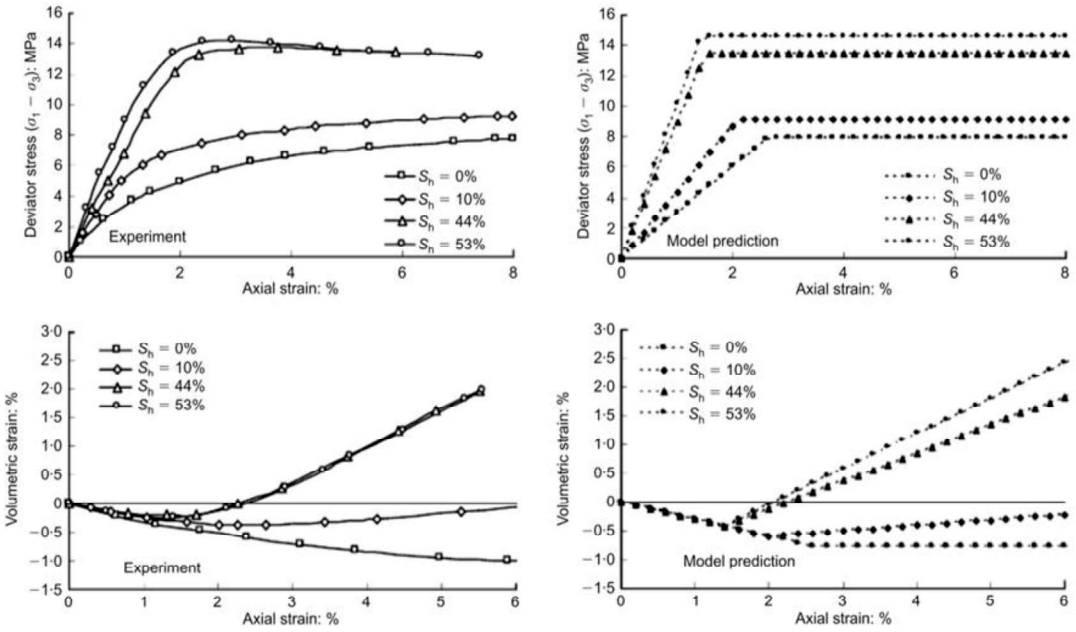

Figure 1-12. The calculation that based on the Mohr-Coulomb model and experimental stress-strain results of hydrate-bearing sediments [*Klar et al.*, 2010].

The Duncan-Chang model is an incremental elastic model based on the hyperbolic stress-strain relationship. This model also requires few parameters. Although many new parameters and corrections have been introduced into the Duncan-Chang model, the model can not describe the strain-softening and volumetric strain behavior of the hydrate-bearing sediments. **Figure 1-13** shows the calculation based on the Duncan-Chang model and experimental stress-strain results of hydrate-bearing sediments. It can be seen that the calculation results of this model match the

experimental results very well, and the transition of the elastoplastic stress-strain relationship is also similar to the actual situation. However, this model cannot describe the volumetric strain behavior of hydrate-bearing sediments. The influence of hydrate saturation cannot be reflected in this model either.

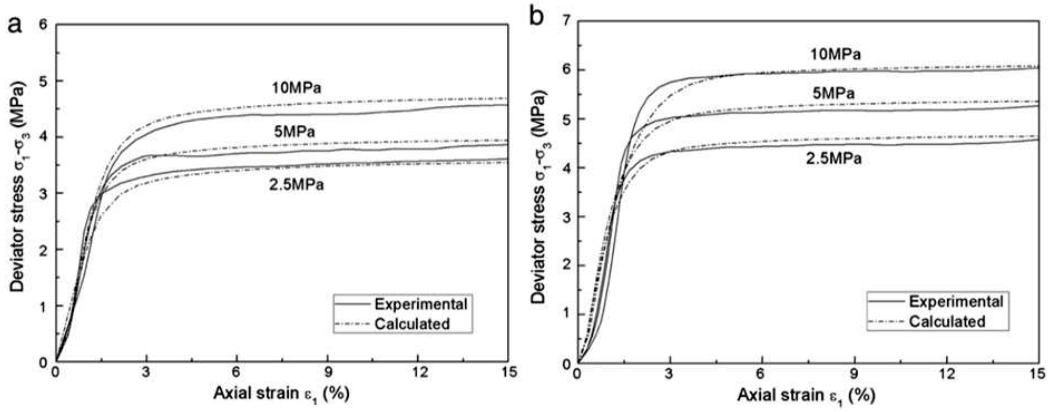

Figure 1-13. The calculation that based on the Duncan-Chang model and experimental stress-strain results of hydrate-bearing sediments [*Yu et al.*, 2011].

Figure 1-14 shows the calculation based on the Critical State model and experimental stress-strain results of hydrate-bearing sediments. It can be found that the critical state model can well reflect the stress and strain characteristics of hydrate-bearing sediments, and the strain-softening characteristics can also be described. The critical state model is an elastoplastic model, and which can reflect the deformation mechanism of hydrate-bearing sediments, as well as the hardening, softening, and dilatancy properties. However, this kind of model has many parameters. It is difficult to obtain these parameters from the experiments, and the calculation process is also very complicated.

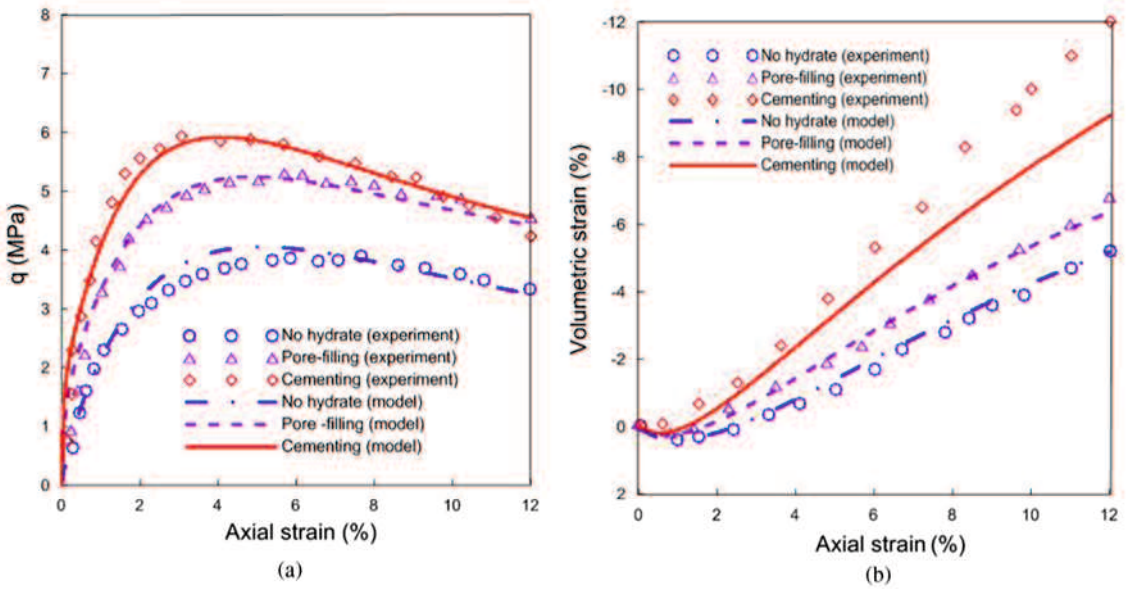

Figure 1-14. The calculation that based on the Critical State model and experimental stress-strain results of hydrate-bearing sediments [*Sánchez et al.*, 2017].

As mentioned earlier, the time-dependent characteristics of the mechanical properties of hydrate-bearing sediments are very important, but only a few models include this feature [*Miyazaki et al.*, 2008; *Yoneda, J et al.*, 2008]. More relevant experiments need to be done to establish and modify models that include time-dependent characteristics and then improve the accuracy of the model for predicting the mechanical behavior of hydrate-bearing sediments.

Table 1-4. Assumptions and limitations of different models. (Modified from *Lijith et al.*, 2019)

Researchers	Models	Assumptions/Description	Main limitations
Klar et al. (2010)	Mohr-Coulomb	1) c', E, and $Sin\ \psi$ vary linearly with S_H. 2) v is assumed to be independent of S_H. 3) Elastic and plastic strains in the native sediments and GHBS are equal.	1) Volumetric yielding could not be predicted precisely, which is important for quantifying the deformation of GHBS when subjected to mechanical loads. 2) Can not to simulate the strain-softening behavior of GHBS.
Pinkert. (2017)	Mohr-Coulomb	1) The presence of hydrate on shear strength and deformation of GHBS by using Rowe's stress dilatancy theory. 2) The behavior of hydrate sediments has been considered without improvement in c', although the model is able to predict stress-strain characteristics of GHBS.	1) The model does not incorporate plastic deformation and dilation.
Yu et al. (2011)	Duncan-Chang	1) Modified the D-C model to incorporate the effect of T and σ_3' on the shear strength and E_i of GHBS. 2) Introduced damage ratio (ω) to accommodate the effect of structural damage of hydrates due to shearing of GHBS. 3) The stress-strain characteristic of GHBS has been divided into two stages, viz., rapid structural damage of hydrates which is expected at low ε_a ($\leq$2%) and complete structural damage of hydrates ($\geq$2%).	1) S_H is not considered in the model. 2) Model does not address the volumetric behavior of GHBS.
Miyazaki et al. (2012)	Duncan-Chang	1) D-C model considering the effect of σ_3' and S_H on the mechanical properties of GHBS. 2) Failure shear strength and E was assumed to increase non-linearly with S_H	1) Volumetric strains are not considered in the study.
Uchida et al. (2012)	Critical State	1) Proposed Methane Hydrate Critical State Model (MHCS Model) for GHBS by adding five extra parameters to Modified Cam Clay model. 2) The model was able to capture enhancement in c', E, ψ, strain-softening, and volumetric behavior of GHBS. 3) The yield curve of GHBS was modified by including two hardening parameters for addressing the enhancement in c' (p_c') and ψ (p_d') and the sub-loading surface ratio (R) which is provided for a smooth transition between the elastic to the plastic behavior of soil.	1) Lack of experimental results limited the model to verify a limited range of S_H. 2) Limitation in using Modified Cam Clay Model (MCCM) for sands (viz., use of elliptical failure envelope).
Lin et al. (2015)	Critical State	1) The model based on C-S framework using spatially mobilized plane concept (SMP) and the sub loading framework. 2) The model was able to show enhancement in E, ψ, and strain-softening with hydrate formation by incorporating three additional parameters to the SMP model.	1) Though the model was able to simulate the stress-strain characteristics, it was not able to determine the volumetric behavior accurately.
Sánchez et al. (2017)	Critical State	1) Proposed a constitutive mechanical model for GHBS incorporating different geomechanical properties of GHBS including E, σ_{dp}, strain-softening, and ψ. 2) The model considered partitioning of the mechanical loads between hydrate and soil. 3) Hydrates were modeled using a damage model (induced by shearing) and the sediment was modeled based on critical state soil mechanics (based on HISS framework). 4) The study assumes that hydrates undergo logarithmic isotropic damage with shearing and load taken by hydrates assumed to decrease logarithmically with shearing. 5) The model was able to show the effect of S_H, HM, and hydrate dissociation on mechanical properties.	1) The volumetric behavior was found to be under-predicted, especially at higher S_H.

c': Effective cohesion; E: Stiffness; E_i: Initial tangent modulus; Ψ: Dilation angle; S_H: Hydrate saturation; σ_3': Effective confining pressure; p_c': Hardening parameter for cohesion; p_d': Hardening parameter for dilation; σ_{dp}: Peak deviatoric stress;

2.4 Decomposition characteristics of hydrate-bearing sediments

To obtain natural gas resources, NGH needs to be decomposed in the reservoir first. Understanding the decomposition characteristics of NGH under different experimental conditions is the key to improving gas production efficiency.

The depressurization method can reduce the pore pressure of the reservoir to decompose the hydrate, and the decomposed natural gas can be transferred to the wellbore under the drive of the high-pressure difference. In the initial stage of depressurization, the natural gas produced by the decomposition of NGH near the wellbore can be quickly obtained, and the gas production efficiency rapidly increases and reaches its peak. However, a large number of studies have shown that the gas production efficiency of the depressurization method dropped rapidly after reaching a peak in the initial stage, and eventually continued to produce natural gas at a very low efficiency [*Yu, T et al*., 2018; *Konno, Y et al*., 2010; *Lu, J et al*., 2018; *Walsh, M. R et al*., 2009]. The following factors may be the cause of this phenomenon. Since the transmission of pressure drop inside the reservoir is limited by the permeability of the reservoir, especially in areas with a high content of fine particles, the range of pressure drop transmission is significantly restricted. Moreover, since hydrate decomposition is an endothermic reaction, the temperature around the decomposition area gradually decreases during the exploitation process [*Yu, M et al*., 2018; *Wang, Y et al*., 2019]. The decomposition gas may be formed hydrate again due to the low temperature and then block the gas migration channel. *Han, G et al*., [2018b] have also shown that the depressurization method can cause the migration of fine particles, which in turn affects the flow of gas and liquid in the pores. All of these can reduce the efficiency of gas production. Increasing the pressure reduction range can significantly improve the initial gas production efficiency, but the risk of wellbore instability and large-area sand production will also increase [*Jin, G et al*., 2018;]. Moreover, this

method cannot solve the problem of the continued decline of gas production efficiency in the later stage of depressurization.

As an auxiliary means of exploitation, thermal stimulation is effective and necessary for improving the decomposition rate of MGH and the gas production efficiency. *Chong et al*., [2016b] introduced a framework to analyze the impact of thermal stimulation on energy recovery with water-saturated marine hydrate sediments. It emphasized the importance of thermal stimulation on the rate of hydrate dissociation, as well as the significance of water management for effectively recovering energy from oceanic methane hydrate deposits. *Wan et al*., [2018a] have studied the character of the heat transfer during hydrate dissociation under thermal injection conditions, and it was found that thermal stimulation can significantly increase the rate of hydrate dissociation compared with only using the depressurization method. *Sakamoto et al*., [2004] performed a series of experiments with a special bulk-scale experimental apparatus used to study the effects of heat injection on hydrate decomposition, including the different well pressures and hydrate saturation levels. It was found that the dissociation process of hydrate in gas hydrate reservoirs can be divided into four steps: (1) part of the free methane gas is released due to heat stimulation; (2) hydrate was reformed in the downstream zone resulting from the flow of water and free gas in the porous media; (3) initiation of hydrate dissociation; and (4) completion of dissociation.

It can be found that the decomposition of NGH under different conditions is limited by the mass transfer and heat transfer processes. Since the mechanical properties of hydrate-bearing sediments are significantly affected by NGH, the decomposition of NGH cannot be completely separated from the mechanical properties of sediments. Furthermore, the stress-strain behavior of the sediments will affect the migration of gas and liquid in the pores, which in turn affects the decomposition of NGH and the efficiency of gas production. Due to the construction of the

wellbore, the sediments located in different positions of the reservoir are in different stress states. Thermal stimulation and depressurization operations trigger the decomposition of NGH, which affects the stress-strain behavior of sediments, and the deformation of sediments will in turn affect the decomposition characteristics of NGH. Understanding the mechanics of hydrate-bearing sediments and the decomposition characteristics of hydrates under different stress states is also necessary to accurately predict the mechanical behavior of the reservoir during the exploitation process and improve the efficiency of gas production.

3. Aim and organization of this thesis

3.1 Aim of this thesis

Natural gas hydrate (NGH) is a clean and promising energy resource. Traditional fossil energy resources are no longer meet the increasing demand for energy consumption. The ultimate aim of this thesis is to provide an experimental basis for the realization of safe and efficient exploitation of NGH.

Firstly, before realizing the safe and efficient exploitation of NGH, it is necessary to study the influence mechanism of different factors on the mechanical properties of hydrate-bearing sediments by the laboratory's mechanical experiments. And then establish the constitutive model of the stress-strain relationship of hydrate-bearing sediments. Finally, according to different exploitation conditions, predict the changes in the mechanical properties of the NGH reservoir during the exploitation process to ensure the safety of exploitation. Sufficient laboratory research is the foundation to ensure the safe exploitation of NGH. Sediments have various stress conditions in the NGH reservoir. However, most of the current studies about the mechanical properties of hydrate-bearing sediments under general stress conditions and then established corresponding constitutive models. The failure of hydrate-bearing sediments under plane strain conditions is always accompanied by significant local strain and eventually formed a clear shear band. Even under the same experimental conditions, the stress-strain relationship of hydrate-bearing sediments is different in the triaxial shear and plane strain shear experiments. Moreover, the local strain may cause changes in the local permeability of the reservoir, which can also affect the gas production efficiency.

In chapter 2, the basic physical properties of the experimental materials in this thesis have been introduced. Then studied the development characteristics of the shear band of hydrate-bearing sediments in the plane strain shear test. Because in the plane strain experiment, the failure of the specimen is affected by the development of the shear band. In particular, the angle and thickness of the shear band are considered to be related to the strength of the specimen. The experimental results are helpful to understand the development process of the shear band in different stress-strain stages and to establish the relationship between the development of the shear band and the stress-strain in the future. To the long-term accurate prediction of the changes in the mechanical properties of the NGH reservoir, the time dependence of hydrate-bearing sediments must be considered. The shear rate dependence experiment is an effective method to study the time dependence of materials, but only a few relevant research results have been reported.

In chapter 3, the shear rate-dependent characteristics of hydrate-bearing sediments have been studied. After confirming that hydrate-bearing sediment also has shear rate-dependent characteristics under plane strain conditions, three different shear rates have been selected to study the effects of hydrate saturation and fines content on shear rate dependence. The research results will help to introduce time parameters into the constitutive model of hydrate sediments in the future, and then achieve long-term accurate prediction of the mechanical characteristics of the NGH reservoir.

Secondly, understanding the decomposition characteristics of hydrates in the sand is the basis for developing methods to improve gas production efficiency.

In Chapter 4, due to the differences in the content of fine particles in different reservoirs, the effect of the content of fine particles on the decomposition characteristics of hydrates in the sand under local thermal stimulation conditions has been studied firstly. On the other hand, sediments located

in different positions of the reservoir may be in different stress states due to the early wellbore construction. Thermal stimulation and depressurization operations cause the decomposition of hydrates, which will also affect the stress-strain behavior of sediments, and the deformation of sediments will in turn affect the decomposition characteristics of hydrates. In other words, the mechanical properties of the reservoir are closely related to the decomposition properties of hydrates. Understanding the mechanics of hydrate-bearing sediments and the decomposition characteristics of hydrates under different stress states is also very important to accurately predict the mechanical behavior of the reservoir during the exploitation process. In the second part of Chapter 4, under different stress conditions, the stress-strain relationship of hydrate-bearing sediments and the decomposition characteristics of hydrates during local thermal stimulation and depressurization have been studied. The experimental results are helpful to understand the interaction mechanism between the decomposition of hydrates and the stress-strain behavior of sediments under different conditions.

3.2 Organization of this thesis

This thesis is composed of five chapters.

Chapter 1. Introduction and literature reviews

Chapter 2. Experimental materials and the development of the shear band

Chapter 3. Shear rate dependence characteristics

Chapter 4. Decomposition of hydrate in sands

Chapter 5. Summary and future work

The content of this thesis is as follows:

In chapter 1, the research background about the natural gas hydrate has been introduced. The current exploitation progress of natural gas hydrate and the related problems were also reviewed. And then the mechanical properties and the decomposition characteristics of hydrate-bearing sediments have been discussed. Finally, the aim and organization of this thesis were shown.

In chapter 2, it has shown the image information and some basic physical properties of the experimental materials that used in this thesis. And then, with the plane strain shear tests on the host sand and hydrate-bearing sediment, the development of the shear band has been studied.

In chapter 3, the shear rate-dependent characteristics of hydrate-bearing sediments have been studied. After confirming that hydrate-bearing sediment also has shear rate-dependent characteristics under plane strain conditions, three different shear rates have been selected to study the effects of hydrate saturation and fines content on shear rate dependence.

In chapter 4, the decomposition of hydrate in sands has been studied. Firstly, the decomposition characteristics of hydrate-bearing sediments with different fine particle contents by local thermal stimulation were researched. And then, combined with different stress conditions, the decomposition characteristics of hydrate in the sediments by local thermal stimulation and depressurization have been studied.

In chapter 5, the summary of this thesis and future work has been shown.

Figure 1-15 show the organization of this thesis.

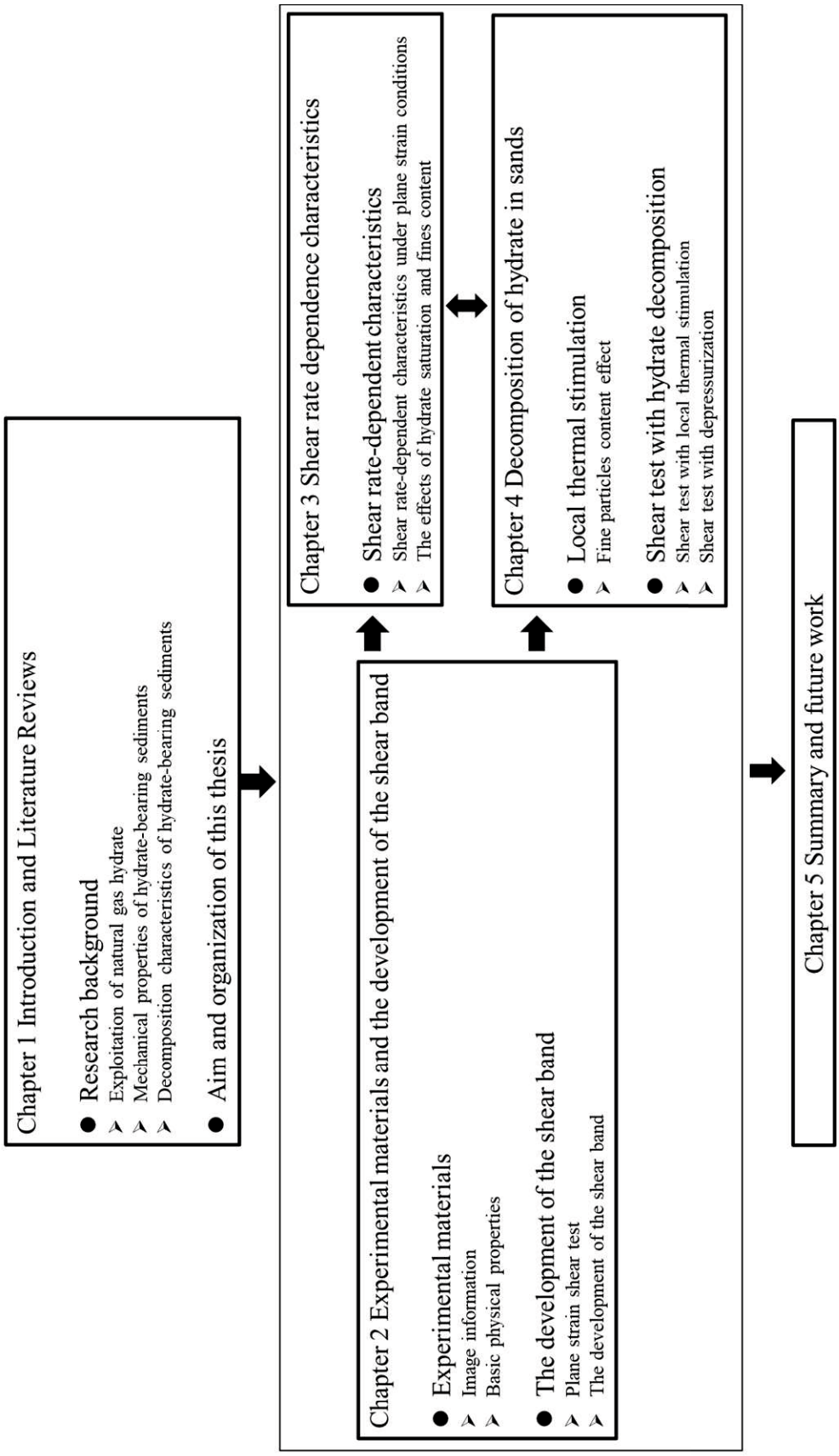

Figure 1-15. The organization of this thesis.

4. References

Alshibli, K. A., and S. Sture (2000), Shear band formation in plane strain experiments of sand, *Journal of Geotechnical and Geoenvironmental Engineering*, *126*(6), 495-503, doi:10.1061/(ASCE)1090-0241(2000)126:6(495).

Birchwood R, Noeth S, Jones E. Safe drilling in gas hydrate prone sediments: findings from the 2005 drilling campaign of the gulf of Mexico gas hydrate joint industry project (JIP). Fire Ice 2008;8:1–8.

Bohrmann, G., and M. E. Torres (2006), Gas hydrates in marine sediments, in *Marine geochemistry*, edited, pp. 481-512, Springer.

Chong, Z. R., S. H. B. Yang, P. Babu, P. Linga, and X. S. Li (2016a), Review of natural gas hydrates as an energy resource: Prospects and challenges, *Appl. Energy*, *162*, 1633-1652, doi:10.1016/j.apenergy.2014.12.061.

Chong, Z. R., G. A. Pujar, M. Yang, and P. Linga (2016b), Methane hydrate formation in excess water simulating marine locations and the impact of thermal stimulation on energy recovery, *Appl. Energy*, *177*, 409-421.

Cui, L., A. Moqsud, M. Hyodo, and S. Bhattacharya (2019), 7 - Methane hydrate as a "new energy", in *Managing Global Warming*, edited by T. M. Letcher, pp. 239-264, Academic Press, doi:https://doi.org/10.1016/B978-0-12-814104-5.00007-7.

He, S., D. Liang, D. Li, and L. Ma (2010), Experimental investigation on the dissociation behavior of methane gas hydrate in an unconsolidated sediment by microwave stimulation, *Energy &*

Fuels, *25*(1), 33-41.

Holder GD, Kamath VA, Godbole SP. The potential of natural gas hydrates as an energy resource. Annu Rev Energy 1984;9:427–45.

Hyodo, M., S. Kajiyama, A. Kato, A. Nishimura, Y. Nakata, and N. Yoshimoto (2015), Effect of fines on mechanical properties of methane hydrate bearing sands, paper presented at Proceedings of the 3rd International Symposium on Frontiers in Offshore Geotechnics, ISFOG 2015, CRC Press/Balkema.

Hyodo, M., Y. Li, J. Yoneda, Y. Nakata, N. Yoshimoto, A. Nishimura, and Y. Song (2013), Mechanical behavior of gas-saturated methane hydrate-bearing sediments, *J. Geophys. Res. Solid Earth*, *118*(10), 5185-5194, doi:doi: 10.1029/2006JB004484.

Hyodo, M., Y. Wu, K. Nakashima, S. Kajiyama, and Y. Nakata (2017), Influence of Fines Content on the Mechanical Behavior of Methane Hydrate-Bearing Sediments, *J. Geophys. Res. Solid Earth*, *122*(10), 7511-7524, doi:10.1002/2017JB014154.

Iwai, H., Y. Konishi, K. Saimyou, S. Kimoto, and F. Oka (2018), Rate effect on the stress-strain relations of synthetic carbon dioxide hydrate-bearing sand and dissociation tests by thermal stimulation, *Soils Found.*, *58*(5), 1113-1132, doi:10.1016/j.sandf.2018.05.007.

Jianliang, Y. (2020), Main progress of the second gas hydrate trial production in the South China Sea, *Geology in China*, *47(3)*, 557-568.

Jin, G., Lei, H., Xu, T., Xin, X., Yuan, Y., Xia, Y., and Juo, J. (2018). "Simulated geomechanical responses to marine methane hydrate recovery using horizontal wells in the Shenhu area, South China Sea." *Mar. Pet. Geol.*, 92, 424-436.doi:10.1016/j.marpetgeo.2017.11.007

Kajiyama, S., Y. Wu, M. Hyodo, Y. Nakata, K. Nakashima, and N. Yoshimoto (2017), Experimental investigation on the mechanical properties of methane hydrate-bearing sand formed with rounded particles, *Journal of Natural Gas Science and Engineering*, *45*, 96-107, doi:10.1016/j.jngse.2017.05.008.

Klar, A., K. Soga, and M. Ng (2010), Coupled deformation–flow analysis for methane hydrate extraction, *Geotechnique*, *60*(10), 765-776.

Klauda, J. B., and S. I. Sandler (2005), Global distribution of methane hydrate in ocean sediment, *Energy & Fuels*, *19*(2), 459-470.

Konno, Y., Y. Masuda, Y. Hariguchi, M. Kurihara, and H. Ouchi (2010), Key factors for depressurization-induced gas production from oceanic methane hydrates, *Energy Fuels*, *24*(3), 1762-1770, doi:10.1021/ef9011565.

Kvenvolden, K. A. (1993), A primer on gas hydrates, *US Geological Survey professional paper*, *1570*, 279-291.

Li, D., Wu, Q., Wang, Z., Lu, J., Liang, D., and Li, X. (2018). "Tri-axial shear tests on hydrate-bearing sediments during hydrate dissociation with depressurization." Energies, 11(7).

Lijith, K., B. R. Malagar, and D. N. Singh (2019), A comprehensive review on the geomechanical properties of gas hydrate bearing sediments, *Mar. Pet. Geol.*

Lin, J. S., Y. Seol, and J. H. Choi (2015), An SMP critical state model for methane hydrate - bearing sands, *International Journal for Numerical and Analytical Methods in Geomechanics*, *39*(9), 969-987.

Lu, J., Xiong, Y., Li, D., Shen, X., Wu, Q., and Liang, D. (2018). "Experimental investigation of

characteristics of sand production in wellbore during hydrate exploitation by the depressurization method." *Energies*, 11(7).doi:10.3390/en11071673

Miyazaki, K., A. Masui, H. Haneda, Y. Ogata, K. Aoki, and T. Yamaguchi (2008), Variable-compliance-type constitutive model for methane hydrate bearing sediment, paper presented at Proceedings of the 6th international conference on gas hydrates.

Miyazaki, K., N. Tenma, K. Aoki, and T. Yamaguchi (2012), A nonlinear elastic model for triaxial compressive properties of artificial methane-hydrate-bearing sediment samples, *Energies*, *5*(10), 4057-4075.

Miyazaki, K., N. Tenma, and T. Yamaguchi (2017), Relationship between creep property and loading-rate dependence of strength of artificial methane-hydrate-bearing toyoura sand under triaxial compression, *Energies*, *10*(10), doi:10.3390/en10101466.

Miyazaki, K., T. Yamaguchi, Y. Sakamoto, and K. Aoki (2011), Time-dependent behaviors of methane-hydrate bearing sediments in triaxial compression test, *International Journal of the JCRM*, *7*(1), 43-48.

Miller D J, Ketzer J M, Viana A R, et al. Natural gas hydrates in the Rio Grande Cone (Brazil): A new province in the western South Atlantic[J]. Marine and Petroleum Geology, 2015, 67: 187-196.

Moridis, G. J., T. S. Collett, R. Boswell, M. Kurihara, M. T. Reagan, C. Koh, and E. D. Sloan (2009), Toward production from gas hydrates: Current status, assessment of resources, and simulation-based evaluation of technology and potential, *SPE Reservoir Evaluation and Engineering*, *12*(5), 745-771, doi:10.2118/114163-PA.

MacDonald I R, Bender L C, Vardaro M, et al. Thermal and visual time-series at a seafloor gas

hydrate deposit on the Gulf of Mexico slope[J]. Earth and Planetary Science Letters, 2005, 233(1-2): 45-59.

Palodkar, A. V., and A. K. Jana (2019), Modeling recovery of natural gas from hydrate reservoirs with carbon dioxide sequestration: Validation with Iġnik Sikumi field data, *Scientific Reports*, *9*(1), 18901, doi:10.1038/s41598-019-55476-1.

Pinkert, S. (2017), Rowe's stress-dilatancy theory for hydrate-bearing sand, *International Journal of Geomechanics*, *17*(1), 06016008.

Rossi, F., A. M. Gambelli, D. K. Sharma, B. Castellani, A. Nicolini, and M. J. Castaldi (2019), Experiments on methane hydrates formation in seabed deposits and gas recovery adopting carbon dioxide replacement strategies, *Applied Thermal Engineering*, *148*, 371-381, doi:10.1016/j.applthermaleng.2018.11.053.

Sakamoto, Y., T. Komai, Y. Kawabe, N. Tenma, and T. Yamaguchi (2004), Gas hydrate extraction from marine sediments by heat stimulation method, paper presented at The Fourteenth International Offshore and Polar Engineering Conference - ISOPE 2004, Toulon.

Sánchez, M., X. Gai, and J. C. Santamarina (2017), A constitutive mechanical model for gas hydrate bearing sediments incorporating inelastic mechanisms, *Comput. Geotech.*, *84*, 28-46, doi:10.1016/j.compgeo.2016.11.012.

Siažik, J., M. Malcho, and R. Lenhard (2017), Proposal of experimental device for the continuous accumulation of primary energy in natural gas hydrates, paper presented at EPJ Web of Conferences, EDP Sciences.

Sloan, E. D. (1998), Gas hydrates: review of physical/chemical properties, *Energy & Fuels*, *12*(2), 191-196.

Sloan Jr, E. D. (2003), Fundamental principles and applications of natural gas hydrates, *Nature*, *426*(6964), 353.

Sloan Jr ED, Koh CA. Clathrate hydrates of the natural gases. 3rd ed. Boca Raton, FL: CRC Press; 2008.

Soga, K., S. Lee, M. Ng, and A. Klar (2006), Characterisation and engineering properties of methane hydrate soils, *Characterisation and engineering properties of natural soils*, *4*, 2591-1642.

Sun, Z. F., N. Li, S. Jia, J. L. Cui, Q. Yuan, C. Y. Sun, and G. J. Chen (2019), A novel method to enhance methane hydrate exploitation efficiency via forming impermeable overlying CO 2 hydrate cap, *Appl. Energy*, *240*, 842-850, doi:10.1016/j.apenergy.2019.02.022.

Uchida, S., K. Soga, and K. Yamamoto (2012), Critical state soil constitutive model for methane hydrate soil, *J. Geophys. Res. Solid Earth*, *117*(B3).

Waite, W. F., J. C. Santamarina, D. D. Cortes, B. Dugan, D. N. Espinoza, J. Germaine, J. Jang, J. Jung, T. J. Kneafsey, and H. Shin (2009), Physical properties of hydrate-bearing sediments, *Reviews of geophysics*, *47*(4).

Wang, B., Z. Fan, J. Zhao, X. Lv, W. Pang, and Q. Li (2018a), Influence of intrinsic permeability of reservoir rocks on gas recovery from hydrate deposits via a combined depressurization and thermal stimulation approach, *Appl. Energy*, *229*, 858-871, doi:10.1016/j.apenergy.2018.08.056.

Wang, B., H. Dong, Y. Liu, X. Lv, Y. Liu, J. Zhao, and Y. Song (2018b), Evaluation of thermal stimulation on gas production from depressurized methane hydrate deposits, Appl. Energy, *227*, 710-718, doi:10.1016/j.apenergy.2017.08.005.

Wang, B., P. Huo, T. Luo, Z. Fan, F. Liu, B. Xiao, M. Yang, J. Zhao, and Y. Song (2017), Analysis of the physical properties of hydrate sediments recovered from the Pearl River mouth basin in the South China Sea: Preliminary investigation for gas hydrate exploitation, *Energies*, *10*(4), doi:10.3390/en10040531.

Walsh, M. R., Hancock, S. H., Wilson, S. J., Patil, S. L., Moridis, G. J., Boswell, R., Collett, T. S., Koh, C. A., and Sloan, E. D. (2009). "Preliminary report on the commercial viability of gas production from natural gas hydrates." *Energy Economics*, 31(5), 815-823.doi:10.1016/j.eneco.2009.03.006

Winters W, Walker M, Hunter R, et al. Physical properties of sediment from the Mount Elbert gas hydrate stratigraphic test well, Alaska North Slope[J]. Marine and Petroleum Geology, 2011, 28(2): 361-380.

Xie, Y., Li, R., Wang, X. H., Zheng, T., Cui, J. L., Yuan, Q., Qin, H. B., Sun, C. Y., and Chen, G. J. (2020). "Review on the accumulation behavior of natural gas hydrates in porous sediments." *Journal of Natural Gas Science and Engineering*, 83.doi:10.1016/j.jngse.2020.103520

Xu, C. G., and X. S. Li (2015), Research progress on methane production from natural gas hydrates, *RSC Advances*, *5*(67), 54672-54699, doi:10.1039/c4ra10248g.

Yamamoto, K. (2015), Overview and introduction: Pressure core-sampling and analyses in the 2012-2013 MH21 offshore test of gas production from methane hydrates in the eastern Nankai Trough, *Mar. Pet. Geol.*, *66*, 296-309, doi:10.1016/j.marpetgeo.2015.02.024.

Yang, Y., Y. He, and Q. Zheng (2017), An analysis of the key safety technologies for natural gas hydrate exploitation, *Advances in Geo-Energy Research*, *1*(2), 100-104.

Yin, Z., G. Moridis, Z. R. Chong, H. K. Tan, and P. Linga (2018), Numerical analysis of

experimental studies of methane hydrate dissociation induced by depressurization in a sandy porous medium, *Appl. Energy*, *230*, 444-459, doi:10.1016/j.apenergy.2018.08.115.

Yoneda, J., M. Hyodo, Y. Nakata, and N. Yoshimoto (2008), Time-dependent elasto-plastic constitutive equation for sedimentary sands supported by methane hydrate, paper presented at the 12th Japan Symposium on Rock Mechanics and the 29th Western Japan Symposium on Rock Engineering, *Jpn. Comm. for Rock Mech., Ube, Japan*, 2-4.

Yoneda, J., A. Masui, Y. Konno, Y. Jin, M. Kida, J. Katagiri, J. Nagao, and N. Tenma (2017), Pressure-core-based reservoir characterization for geomechanics: Insights from gas hydrate drilling during 2012–2013 at the eastern Nankai Trough, *Mar. Pet. Geol.*, *86*, 1-16, doi:10.1016/j.marpetgeo.2017.05.024.

Yoneda, J., M. Oshima, M. Kida, A. Kato, Y. Konno, Y. Jin, J. Jang, W. F. Waite, P. Kumar, and N. Tenma (2018), Pressure core based onshore laboratory analysis on mechanical properties of hydrate-bearing sediments recovered during India's National Gas Hydrate Program Expedition (NGHP) 02, *Mar. Pet. Geol.*, doi:10.1016/j.marpetgeo.2018.09.005.

Yu, F., Y. Song, W. Liu, Y. Li, and W. Lam (2011), Analyses of stress strain behavior and constitutive model of artificial methane hydrate, *J. Pet. Sci. Eng.*, *77*(2), 183-188.

Yu, M., Li, W., Jiang, L., Wang, X., Yang, M., and Song, Y. (2018). "Numerical study of gas production from methane hydrate deposits by depressurization at 274 K." *Appl. Energy*, 227, 28-37.doi:10.1016/j.apenergy.2017.10.013

Yun, T. S., J. C. Santamarina, and C. Ruppel (2007), Mechanical properties of sand, silt, and clay containing tetrahydrofuran hydrate, *J. Geophys. Res. Solid Earth*, *112*(B4).

Yu, T., Guan, G., Abudula, A., Yoshida, A., Wang, D., and Song, Y. (2018). "Gas recovery

enhancement from methane hydrate reservoir in the Nankai Trough using vertical wells." *Energy*, 166, 834-844.doi:10.1016/j.energy.2018.10.155

Zhang G, Liang J, Yang S, et al. Geological features, controlling factors and potential prospects of the gas hydrate occurrence in the east part of the Pearl River Mouth Basin, South China Sea[J]. Marine and Petroleum Geology, 2015, 67: 356-367.

Chapter 2 Experimental materials and the development of the shear band

1. Introduction

The majority of the world's natural gas hydrate (NGH) resources exist in marine sediments. The results of marine NGH exploration in recent years have shown that NGH reservoirs in different sea areas have unique characteristics. For example, the occurrence mode of NGH in sediments, hydrate saturation, and particle size distribution of reservoirs varied with location. To develop a safe and efficient exploitation strategy with a wider range of adaptability, it is particularly important to study the mechanical and decomposition characteristics of hydrate-bearing sediments with different fine particle contents. The plane strain shear test can simultaneously complete the study of the mechanical behavior and local strain characteristics of hydrate-bearing sediments. Unlike the triaxial shear test, the generation of shear bands is an inevitable failure mode under plane stress conditions [*Khalid A Alshibli and Sture*, 1999; *White et al.*, 2020]. It has been found that the thickness of the shear band was closely related to the particle size and density of the sample. The failure theories such as Mohr-Coulomb (M-C), Roscoe [*Roscoe K H.*, 1970], and Arthur [*Arthur J F R et al.*, 1977] related the angle of the shear band to the internal friction and dilatancy angle of the sample. The higher porosity ratio and more significant particle crushing in the shear band area can also affect the change of the local permeability of the sample. At present, there are only a few studies on the mechanical properties of gas hydrate-bearing sediments under plane strain conditions, but it has been found that the presence of hydrates will affect the

properties of the shear band of the sediments [*Kajiyama et al.*, 2017; *Yoneda et al.*, 2013]. In different reports, the research stage of the shear band characteristics is quite different, which makes it difficult to compare the research results. In addition, the angle and thickness of the shear band may change during the shearing process. Studying the development of the shear band during the shearing process is helpful for the comparison of different research results. And it can also provide a date reference for the establishment of constitutive models containing the parameters of the angle and thickness of the shear band.

Some basic information of the materials used in the experiment is introduced in this chapter, including image information, material composition, particle size distribution, and permeability. This information is very helpful to understand the mechanical behavior and decomposition characteristics of the hydrate-bearing sediments in chapters 3 and 4.

In addition, the plane strain shear test results of hydrate-bearing sediments are also displayed. The stress-strain curves of hydrate-bearing sediments under plane strain conditions and the development characteristics of shear bands are also explained. In this study, a method combining Particle Tracking Velocimetry (PTV) technology to measure the angle and thickness of the shear band is proposed. With this method, it is possible to study the small changes in the angle and thickness of the shear band during the shearing process.

2. Experimental materials

2.1 Image information

In this study, three different materials named Toyoura, Tb, and Tc have been used as host sand. Here, the 'T' in the names Tb and Tc represents 'Turbidite', which was first proposed by *Suzuki et al*., [2009]. The images of the experimental materials are shown in **Figure 2-1**. Both Tb and Tc are composed of five different kinds of sand, namely No. 7 silica, No. 8 silica, R5.5 silica, Kaolin, and MK-300 mica, respectively. **Table 2-1** shows the composition of Tb and Tc. The microscopic photographs of three different materials are shown in **Figure 2-2 (a)**. **Figure 2-2 (b)** shows the schematic diagram of the particle arrangement of the three host sands. Since fine particles can occupy the pore spaces between large particles, the average pore size of Tb and Tc is much smaller than Toyoura.

Figure 2-1. The images of the experimental materials.

Table 2-1. The composition of Tb and Tc [*Kajiyama et al.*, 2017].

Name	No. 7 silica	No. 8 silica	R 5.5 silica	Kaolin	MK-300 mica
Tb (%)	70	17	10	1	2
Tc (%)	30	55	7	3	5

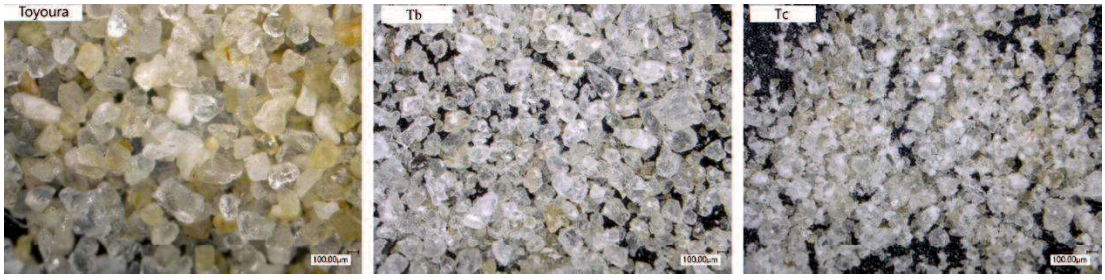

Figure 2-2 (a). The microscopic photographs of Toyoura, Tb, and Tc [*Kajiyama et al.*, 2017].

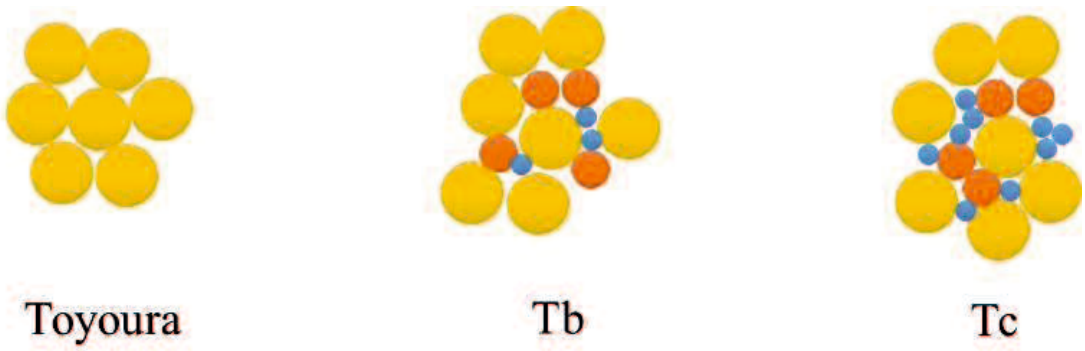

Figure 2-2 (b). The schematic diagram of the particle arrangement of Toyoura, Tb, and Tc.

2.2 Basic physical properties

Since the materials used in this study are composed of different types of sand, some of their basic physical properties are also different. **Figure 2-3** shows the particle size distribution curves of three different host sand. Here, the fine particle content (*Fc*) of the Toyoura, Tb, and Tc are 0%, 8.9%, and 22.9% respectively. The gray shaded part in **Figure 2-3** represents the size distribution range of NGH reservoirs in the Nankai Trough.

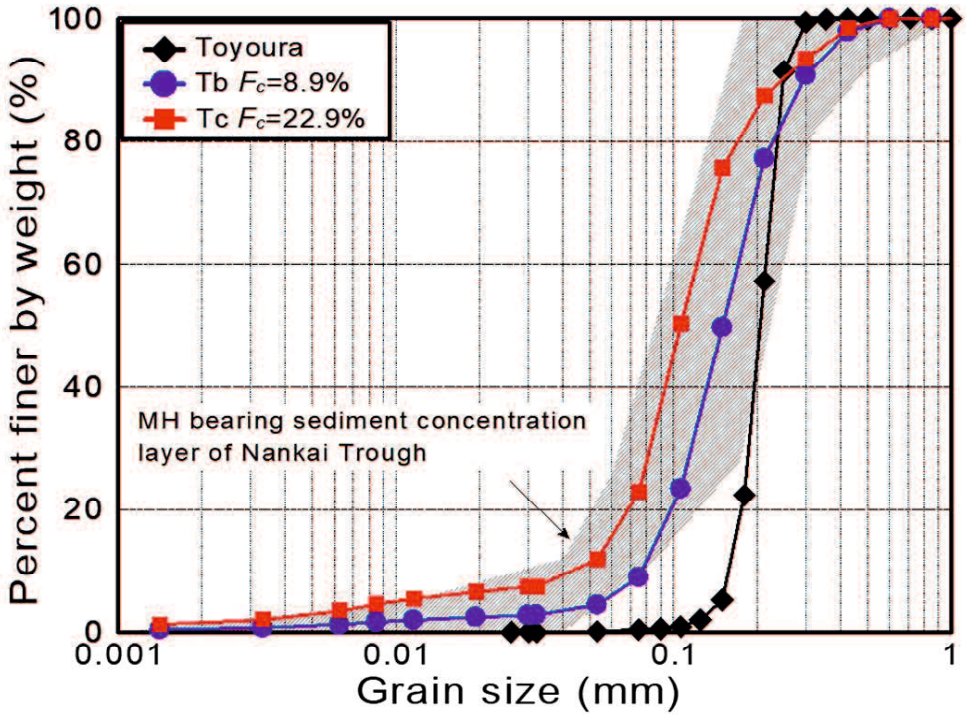

Figure 2-3. The particle size distribution curves of Toyoura, Tb, and Tc (modified from [*Kajiyama et al.*, 2017]).

The density and specific heat capacity of different sands are shown in **Table 2-2**.

The permeability of the materials is calculated according to Formula (2-1):

$$k = \frac{QL}{hAt} \tag{2-1}$$

where k is permeability (cm/s), Q, L is the volume of water passing through the sample in time t (cm^3), the height of the sample (cm), respectively. And h, A, t, are hydraulic head (cm), cross-sectional area (cm^2), and measured time (s), respectively. The permeability of Toyoura, Tb, and Tc is shown in **Figure 2-4**. It can be found that the permeability of Tc is far lower than that of the Toyoura and Tb. As more fine particles may fill in the pores of Tc, the transport of the liquid becomes difficult, and which reduces the permeability of the Tc.

Table 2-2. The density and specific heat capacity of different sands.

Name	Density (ρ_s) kg/m^3	Specific heat capacity (c_s) J/(kg·k)
Toyoura	2650	745
Kaolin	2618	841
MK-300 mica	2700	865
No. 8 silica	2673	745
No. 7 silica	2661	754
R 5.5	2640	745

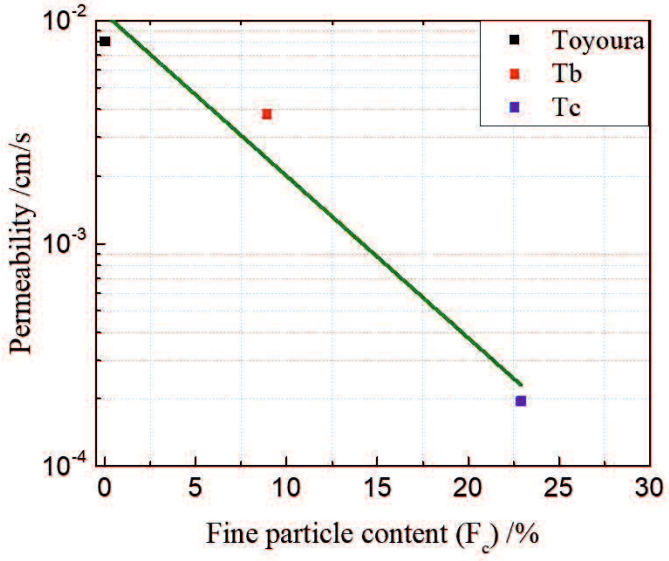

Figure 2-4. The permeability of Toyoura, Tb, and Tc.

3. The development of the shear band

3.1 Plane strain shear test

3.1.1 Experimental instrument

A high-pressure and low-temperature plane strain shear test apparatus has been adopted to study the mechanical properties of methane hydrate-bearing sediments. The view of the experimental apparatus is shown in **Figure 2-5**. The experimental apparatus was placed in the temperature-controlled room, and the temperature was controlled by a temperature regulator within 273.15 K to 303.15 K, with an accuracy of ± 0.5 K. The operation of the experimental system was controlled by an external computer.

Figure 2-6 shows the schematic diagram of the experimental instrument system. The size of the specimen (a) was 80 mm (length) × 60 mm (width) × 160 mm (height). The water in the cell liquid tank (j) can be injected into the pressure cell (b), and the cell (confining) pressure was controlled by the confining pressure amplifier (k) with an accuracy of ± 0.1 MPa. The 60 mm × 160 mm surface (surface σ_2) of the specimen was bound by two confining plates (d), and the digital camera (p) can record the picture information of this surface of the specimen during the experiment through the observation window (c). The pore pressure of the specimen can be controlled from 0 to 20.0 MPa by four different syringe pumps (e, f, g, h)with an accuracy of ± 0.1 MPa. Through the methane gas cylinder (j) and syringe pumps (e) and (f), methane gas can be injected into the bottom and top of the specimen at the same time. A compression loading system (m and n) that could supply a loading capacity of 200 kN was installed. The axial strain of the specimen can be measured by the displacement transducer (l). The temperature sensor (q) on the diagonal inside the sample, which was used to measure the temperature of the specimen.

Figure 2-7 shows the detailed position of the temperature sensor. It can be seen that the temperature sensor was 30mm away from the bottom of the specimen.

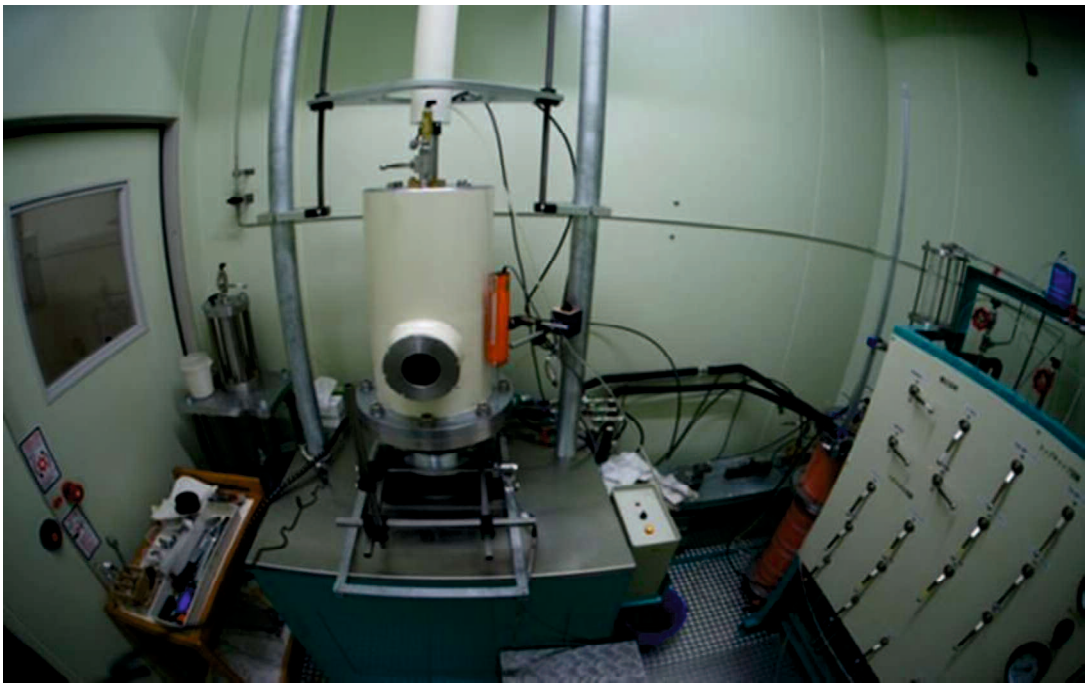

Figure 2-5. The view of the experimental apparatus.

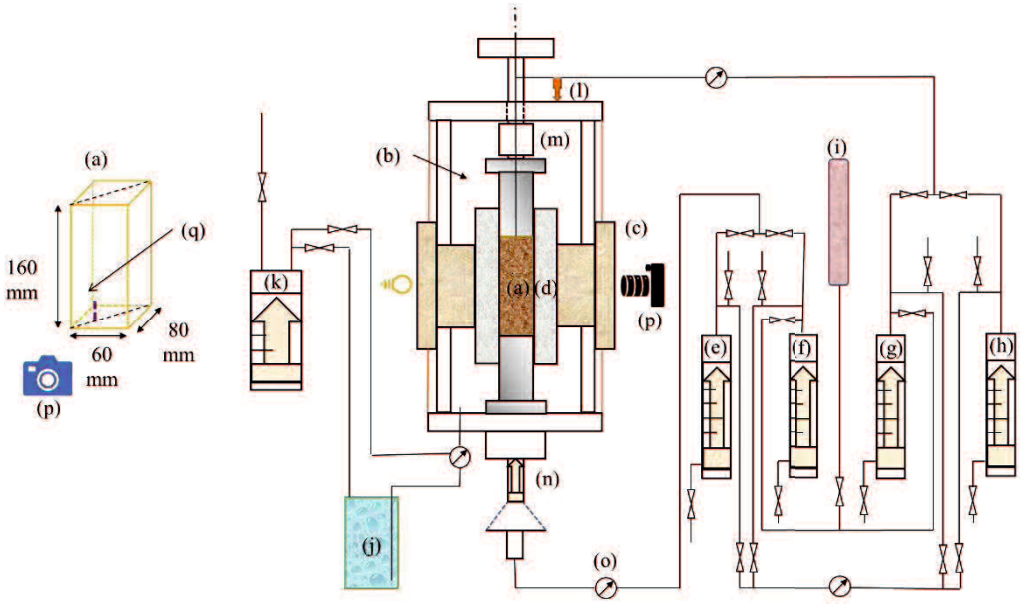

(a) Specimen; (b) pressure cell; (c) observation window; (d) confining plate; (e) lower syringe pump for water;(f) lower syringe pump for gas; (g) upper syringe pump for gas; (h) upper syringe pump for water; (i) methane gas cylinder; (j) cell liquid tank; (k) confining pressure amplifier; (l) displacement transducer; (m) load cell; (n) loading equipment; (o) pressure gauge; (p) camera; (q) thermocouple.

Figure 2-6. The schematic diagram of the experimental instrument system.

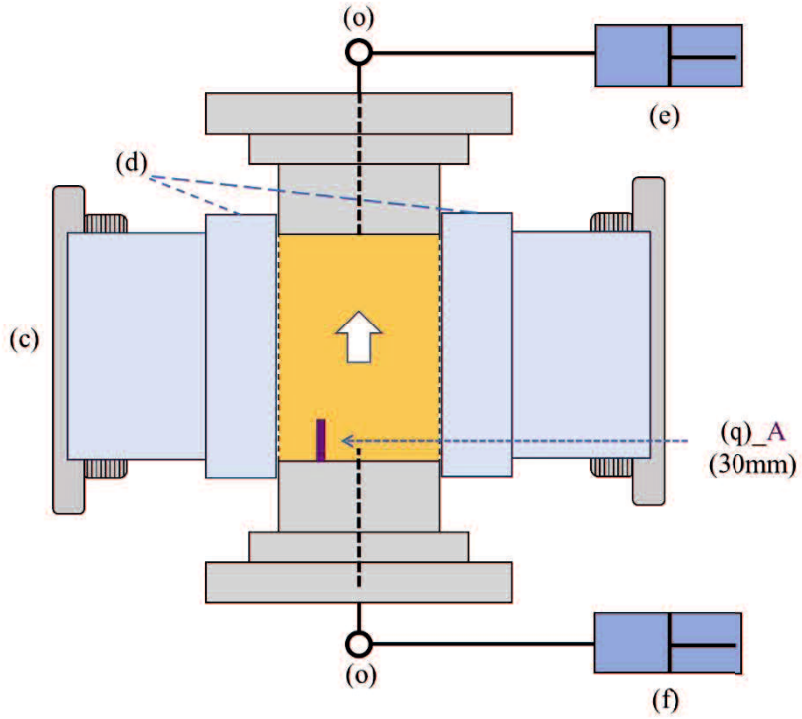

Figure 2-7. The height information of the temperature sensor.

3.1.2 Experimental procedures

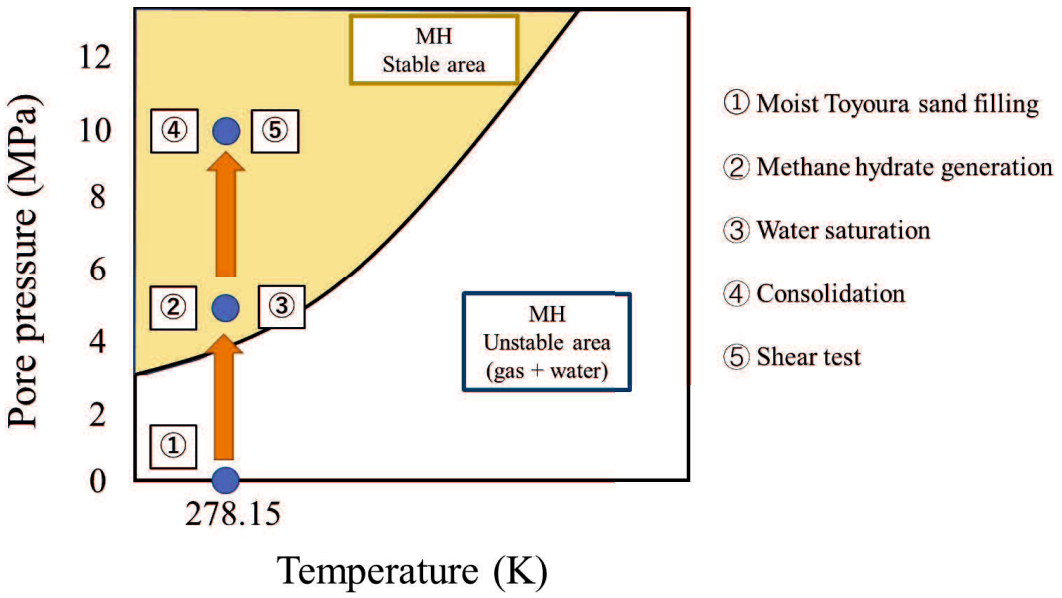

Figure 2-8. the flowchart of the experimental procedures.

Figure 2-8 shows the flowchart of the experimental procedures. And the detailed description of the experimental procedures is as follows.

- Methane hydrate-bearing sediment preparation

In this study, Toyoura sand was adopted as the host sand. (1) Toyoura sand and a certain amount of water for target hydrate saturation were evenly mixed. (2) After the membrane with a grid attached was installed to the mold, the moist Toyoura sand was divided into 12 layers and filled into the mold. (3) Filter papers were applied to the upper and bottom surfaces of the specimen. Two acrylic confining plates were fixed on the opposite side of the specimen to maintain plane strain conditions. (4) A vacuum pump was used to remove free air from the inside of the specimen. (5) Water was filled within the confining chamber after the cell was fixed. Syringe pumps were adopted to inject water and gas into the apparatus. Methane gas could be injected into the specimen from both the top and the bottom with two syringe pumps. By injecting water and methane gas into the machine, the pore pressure and the cell pressure were increased to 5.0 MPa

and 5.2 MPa gradually. During this period, the confining pressure was kept higher than the pore pressure at all times. (6) The methane hydrate-bearing sediment was formed at 278.15 K and under 5.0 MPa (pore pressure) for about 3 days.

- Water saturation and consolidation

After the generation of the methane hydrate inside the specimen, water was injected from the bottom of the specimen to replace the excess methane gas, making the specimen saturated with water. And then gradually increased the pore pressure and confining pressure to 10.0 MPa and 13.0 MPa, respectively. Consolidation was conducted under this condition for about 1 hour.

- Shear test and hydrate saturation calculation

The axial loading was applied to the specimen under drained conditions after the consolidation. The shear strain rate here was 0.2 %/min, and the local deformation of the specimen was also recorded by the digital camera at the same time.

The hydrate saturation (S_{MH}) was defined as for formula (2-2):

$$S_{MH}(\%) = \frac{V_{MH}}{V_V} \times 100 \tag{2-2}$$

Where V_{MH} is the volume of the methane hydrate and V_V is the total pore volume of samples. During the sample preparation time, the initial water ratio of the moist sand was calculated based on the target hydrate saturation. Formula (2-3) defines the initial water ratio ($w_{initial}$):

$$w_{initial} = \frac{(S_{MH}/100)\cdot V_V \cdot \rho_{MH}}{m_s} \cdot A \tag{2-3}$$

Where ρ_{MH} is the density of methane hydrate, and $\rho_{MH} = 0.912$ (g/cm^3) was adopted. A is the water content of individual methane hydrate molecules ($CH_4 \cdot 6H_2O$). The molar mass of methane hydrate (M_{MH}) is 124.0 g/mol. Through simple calculations the value of A can be got (A=108/124×100=87.1 %); m_s is the quality of dry sand.

After the shear test, the hydrate saturation of the synthesized methane hydrate-bearing sediments would be calculated using the total collected methane gas volume [*Li et al.*, 2018].

$$S_{MH}(\%) = \frac{L/164}{V_V} \times 100\% \quad (2\text{-}4)$$

Where L is the total volume of methane gas collected from the decomposition of the specimen in the standard state.

The experimental conditions are shown in **Table 2-3**.

Table 2-3. Experimental conditions.

Test	Void Ratio	Hydrate Saturation (%)	Confining Pressure (MPa)	Pore Pressure (MPa)	Temperature (K)	Shear Rate (%/min)
1	0.711	0	13.0	10.0	278.15	0.2
2	0.706	37.1	13.0	10.0	278.15	0.2

3.1.3 Particle tracking velocimetry technology

The particle tracking velocimetry (PTV) is a non-contact measurement of the velocities and trajectories of moving targets. The schematic diagram of PTV technology is shown in **Figure 2-9**. As shown in **Figure 2-9**, a series of reference points are drawn on the membrane attached to the surface of the specimen. The digital camera records the images of different shearing test stages and then obtains the displacement increment by comparing the position changes of the reference points before and after deformation. Finally, the velocities and trajectories of the reference point movement can be calculated [*Yoneda et al.*, 2013].

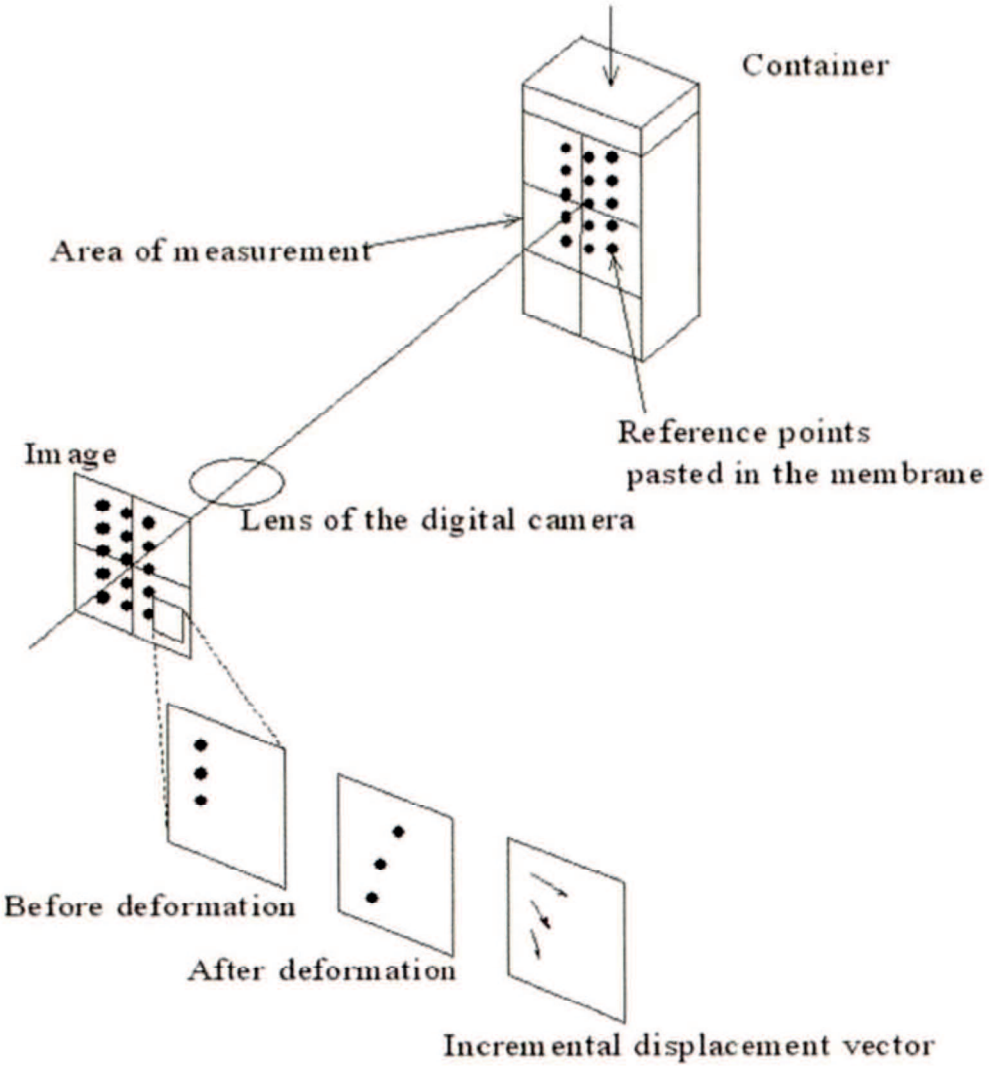

Figure 2-9. The schematic diagram of PTV technology [*Yoneda, J*, 2011].

In this study, the reference points to be tracked were the position of the intersection of the grid drawn on the membrane. **Figure 2-10** shows the PTV analysis area in this study. The size of the full PTV analysis area is 60 × 140 mm and the smallest analysis element size is 2 × 2 mm. To reduce the boundary effect, the measurement area of the shear band is the center part of the PTV analysis area with the size of 44 × 124 mm. The intersection of the grid on the membrane can move with the deformation of the specimen. According to the position information before and

after the movement of the intersection of the analysis element, the local strain increment of the specimen can be calculated.

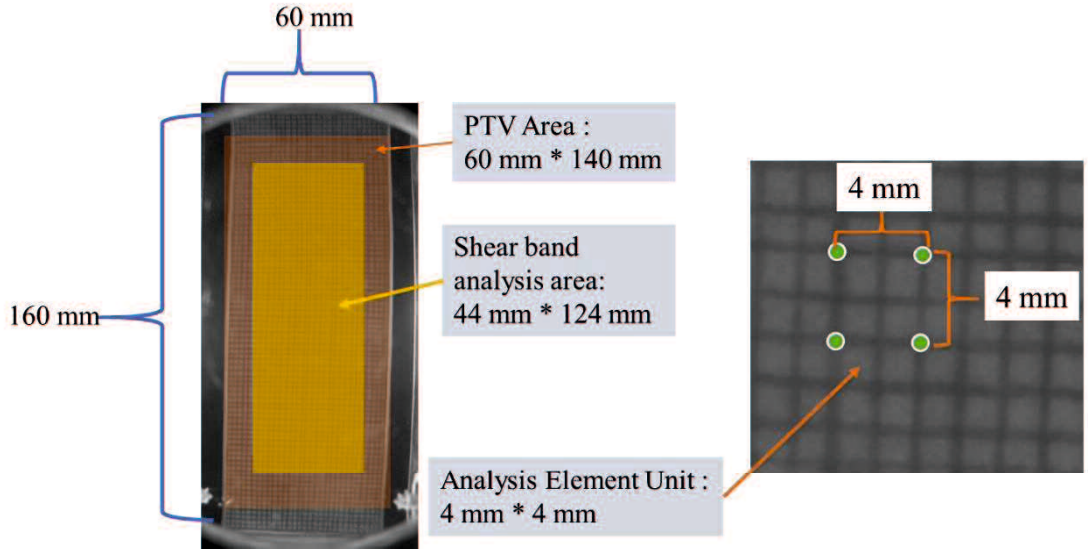

Figure 2-10. The PTV analysis area.

The strain in the horizontal (x) and vertical (y) direction are obtained according to Formula (2-5) and (2-6), respectively:

$$\varepsilon_x = -\frac{\partial_u}{\partial_x} \tag{2-5}$$

$$\varepsilon_y = -\frac{\partial_v}{\partial_y} \tag{2-6}$$

Where ε_x is the strain in the horizontal (x) direction, u is displacement in the horizontal (x) direction. ε_y is the strain in the vertical (y) direction, v is displacement in the vertical (y) direction.

The shear strain and volumetric strain can be calculated by formulas (2-7) and (2-8), respectively:

$$\gamma_{yx} = -\left(\frac{\partial_u}{\partial_x} + \frac{\partial_v}{\partial_y}\right) \tag{2-7}$$

$$\varepsilon_v = \varepsilon_x + \varepsilon_y \tag{2-8}$$

Where γ_{yx} and ε_v are shear strain and volumetric strain, respectively.

The maximum shear strain is obtained by formula (2-9):

$$\gamma_{max} = \sqrt{(\varepsilon_y - \varepsilon_x)^2 + {\gamma_{yx}}^2} \tag{2-9}$$

where γ_{max} is the maximum shear strain.

3.2 Development of the shear band

3.2.1 Stress-strain behavior

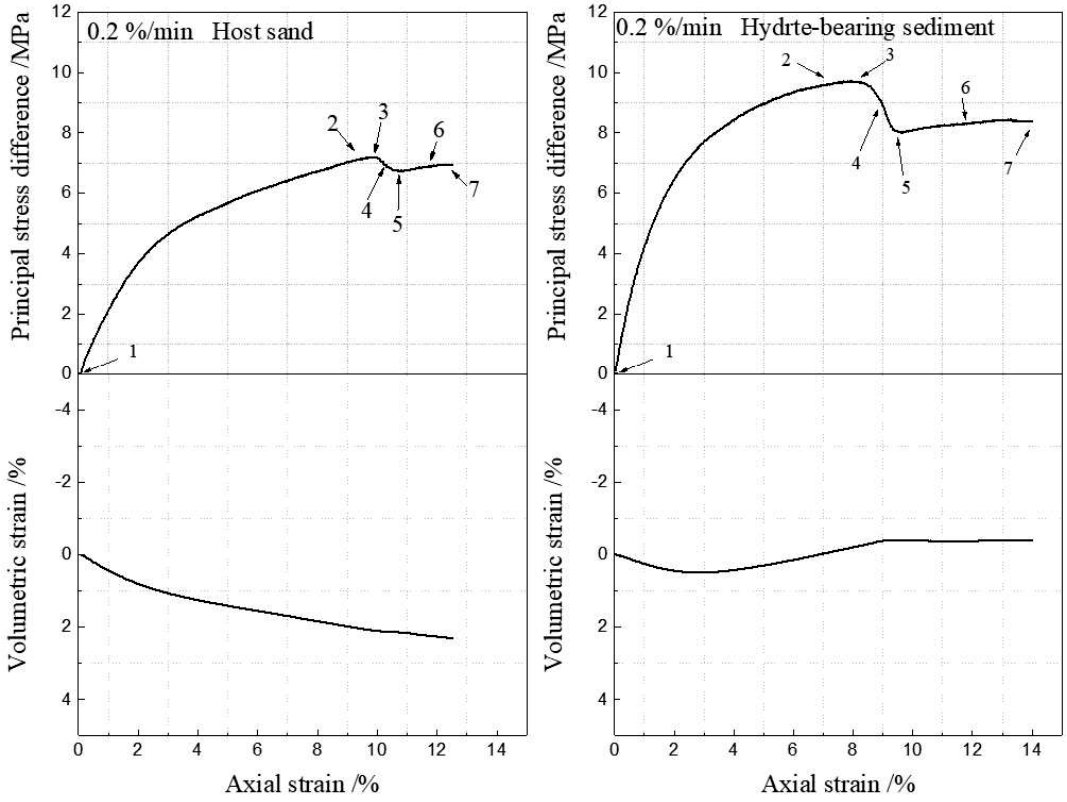

Figure 2-11. Stress-strain relationship of host sand and hydrate-bearing sediment.

Figure 2-11 shows the stress-strain relationship of host and hydrate-bearing sediment. It can be found that the hydrate-bearing sediment showed higher stiffness and strength. The volumetric strain of the hydrate-bearing sediment gradually changed from compressive to dilative during the shearing process, while the host sand only showed compressive behavior. These are consistent with previous reports [*Kajiyama et al.*, 2017; *Yoneda et al.*, 2013]. Previous studies have shown that the appearance of shear bands was accompanied by the failure of the specimen in the plane

strain shear experiment [*Khalid A Alshibli and Sture*, 1999; *Finno et al.*, 1997]. To study the development of the shear band, seven different stages during the shearing test were selected as the object of analysis (as shown in **Figure 2-11**). They are: (1) the starting point; (2) the point before the peak; (3) the peak point; (4) the point where the principal stress difference drops fastest after the peak; (5) the point where the principal stress difference begins to maintain stability; (6) The point where the principal stress difference remains stable; (7) The ending point.

3.2.2 Localized deformation

Figure 2-12 shows the image information of the host sand and the hydrate-bearing sediment sample at different shear stages. The clear shear band can only be observed after the principal stress difference of the samples reached the peak. To make it easier to observe the development of the shear band, **Figure 2-13** shows the contours of maximum shear strain (γ_{max}) of the host sand and hydrate-bearing sediment at different shear stages.

For the host sand, before the principal stress difference reaches the peak (stage 2), the localization of the shear strain of the sample is not significant, and then a clear shear band was gradually formed. The γ_{max} in the central area of the shear band is higher than in other areas. For the hydrate-bearing sediment, similarly, the clear shear band gradually formed after the peak strength (stage 3). However, compared with the host sand, the area with high γ_{max} (red area) in the shear band of hydrate-bearing sediment is wider. *Yoneda et al*., [2013] found that the shear band of the hydrate-bearing sediment had a larger γ_{max} than that of the host sand. And the shear band of the hydrate-bearing sediment was narrower and appeared earlier. It was reported that the cementation of hydrates on sediment particles was responsible for these results. *Kajiyama et al*., [2017] also found that the clear shear band of the host sand and hydrate-bearing sediments appeared after the peak strength. From **Figure 2-13**, it can be found that the thickness and angle of the shear band

may change in different shear stages. Previous studies [*Khalid A Alshibli and Sture*, 1999; *K. A. Alshibli and Sture*, 2000; *Hutchinson and Tvergaard*, 1981; *Mühlhaus and Vardoulakis*, 1987] have simply assumed that the shear band has a constant angle and thickness, and the angle and thickness measurement position of the shear band were also not uniform in different works of literature. This may make it difficult to compare the results of different studies. It is necessary to develop a method to measure the small changes in the angle and thickness of the shear band and to study the development of the shear band in different shear stages.

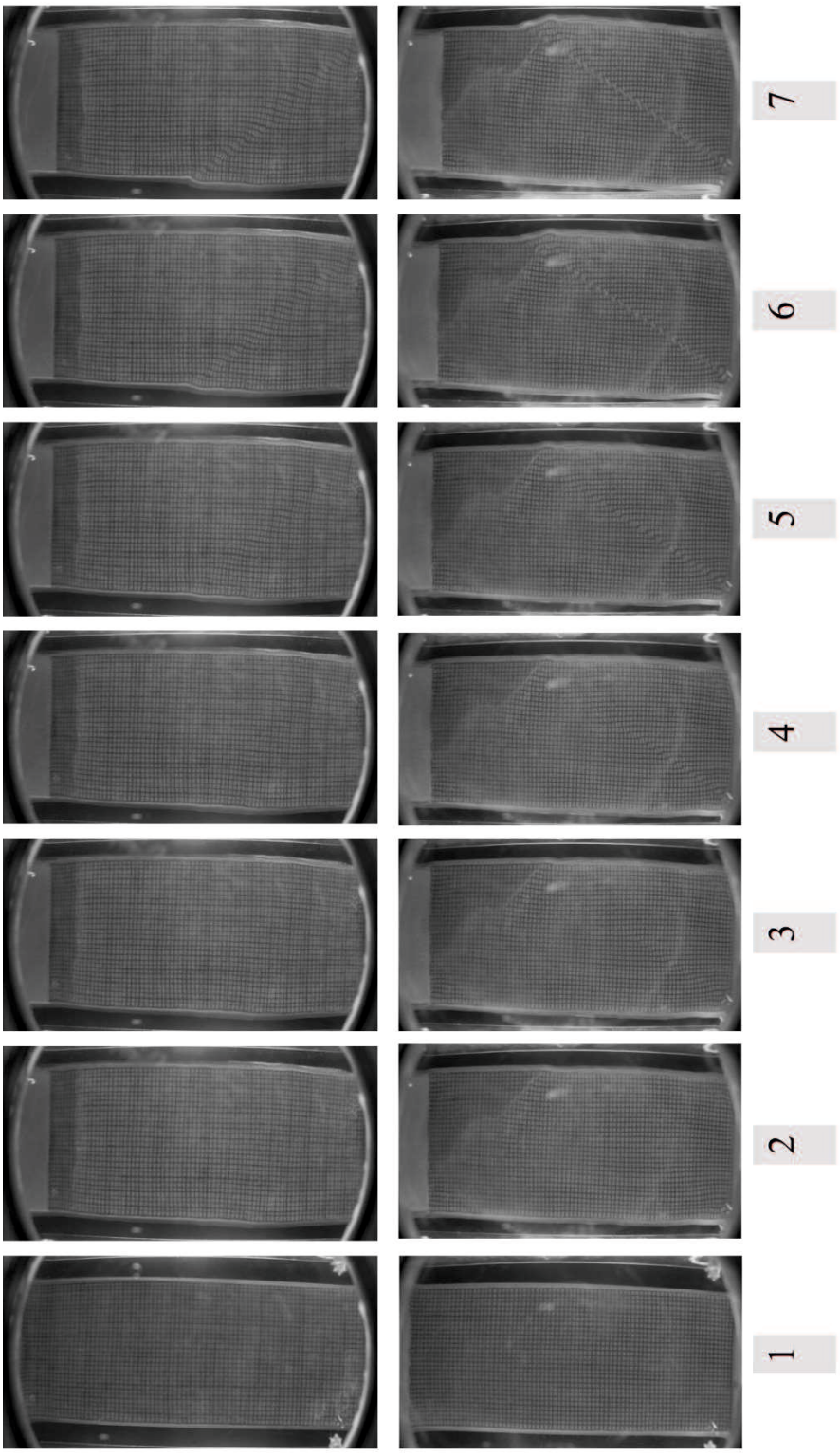

Figure 2-12. Specimen images during the shearing test: (upper) Host sand; (bottom) Hydrate-bearing sediment.

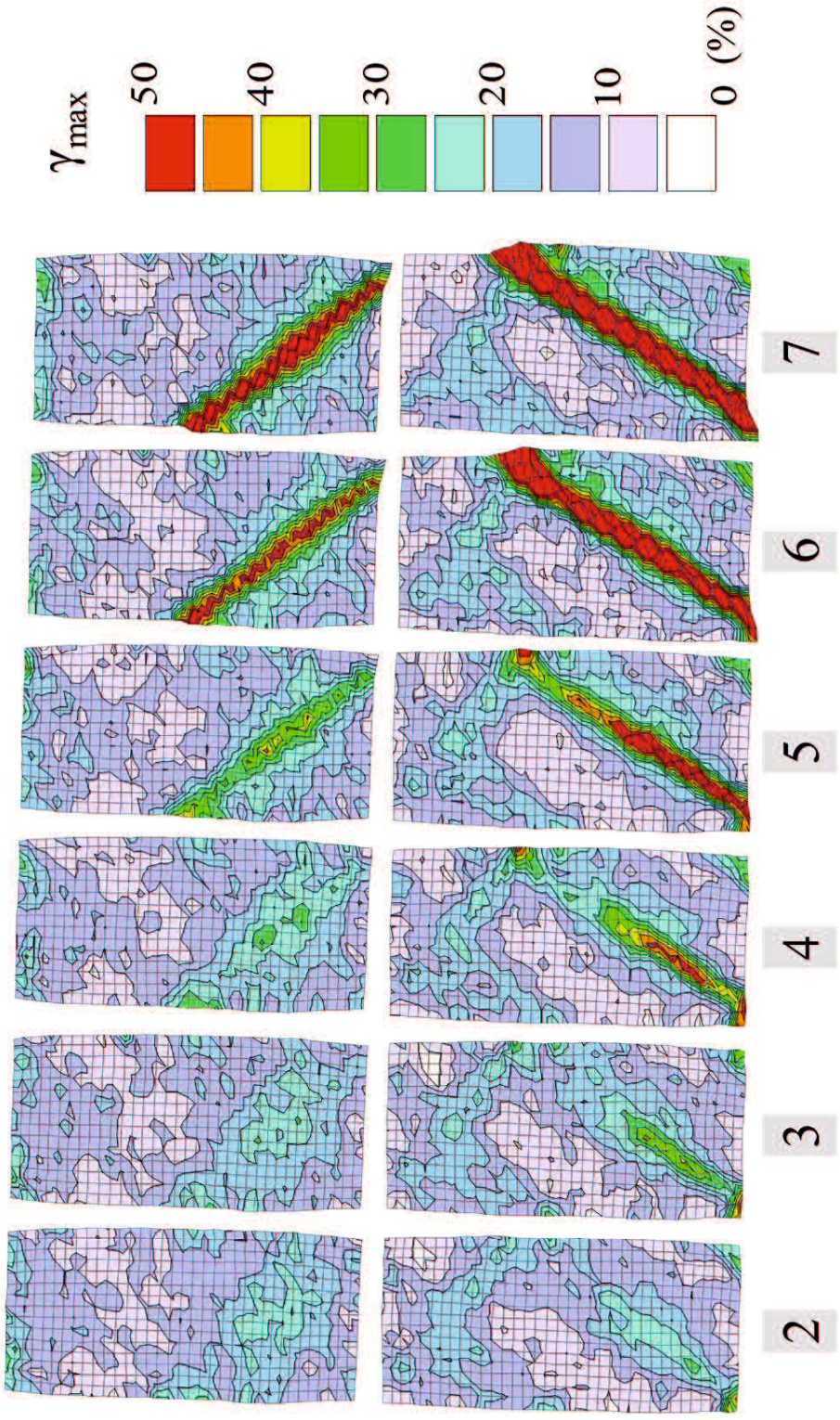

Figure 2-13. The contours of maximum shear strain (γ_{max}) of the host sand (upper) and hydrate-bearing sediment (bottom) at different shear stages.

3.2.3 Measurement of the angle of the shear band

It has been found that under plane strain conditions, the maximum shear strain (γ_{max}) at the shear band position is much greater than that of other regions [*K. A. Alshibli and Sture*, 2000; *Finno et al.*, 1997]. In this study, the same phenomenon can also be observed from **Figure 2-13**. Such, it can be separated the shear band by selecting the area with a higher value of γ_{max}.

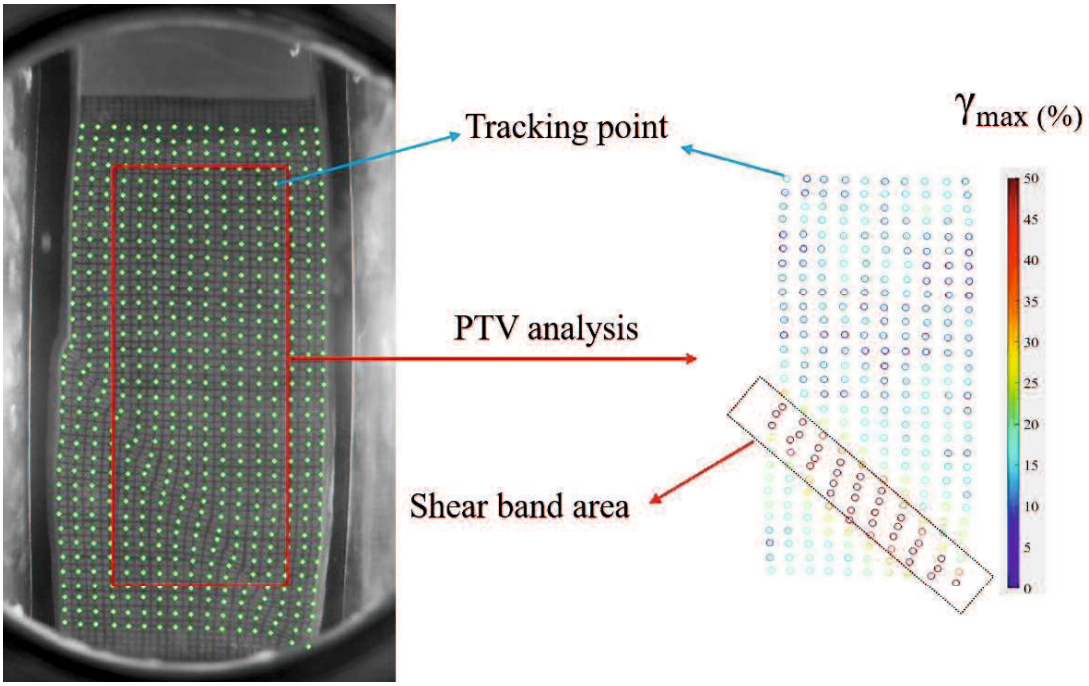

Figure 2-14. Example of γ_{max} result in the PTV analysis area.

Figure 2-14 shows an example of γ_{max} result in the PTV analysis area, the γ_{max} values for different tracking points in the original image can be obtained by PTV technology. The γ_{max} values of the tracking points in the PTV analysis area were mapped through different colors in the right of **Figure 2-14**, and it can be found that the γ_{max} values of the traction points that in the shear band were much larger than other areas. If the tracking points in the shear band area can be accurately extracted, and then perform a linear fit to these tracking points, the inclination of the fitted line can be regarded as the angle of the shear band.

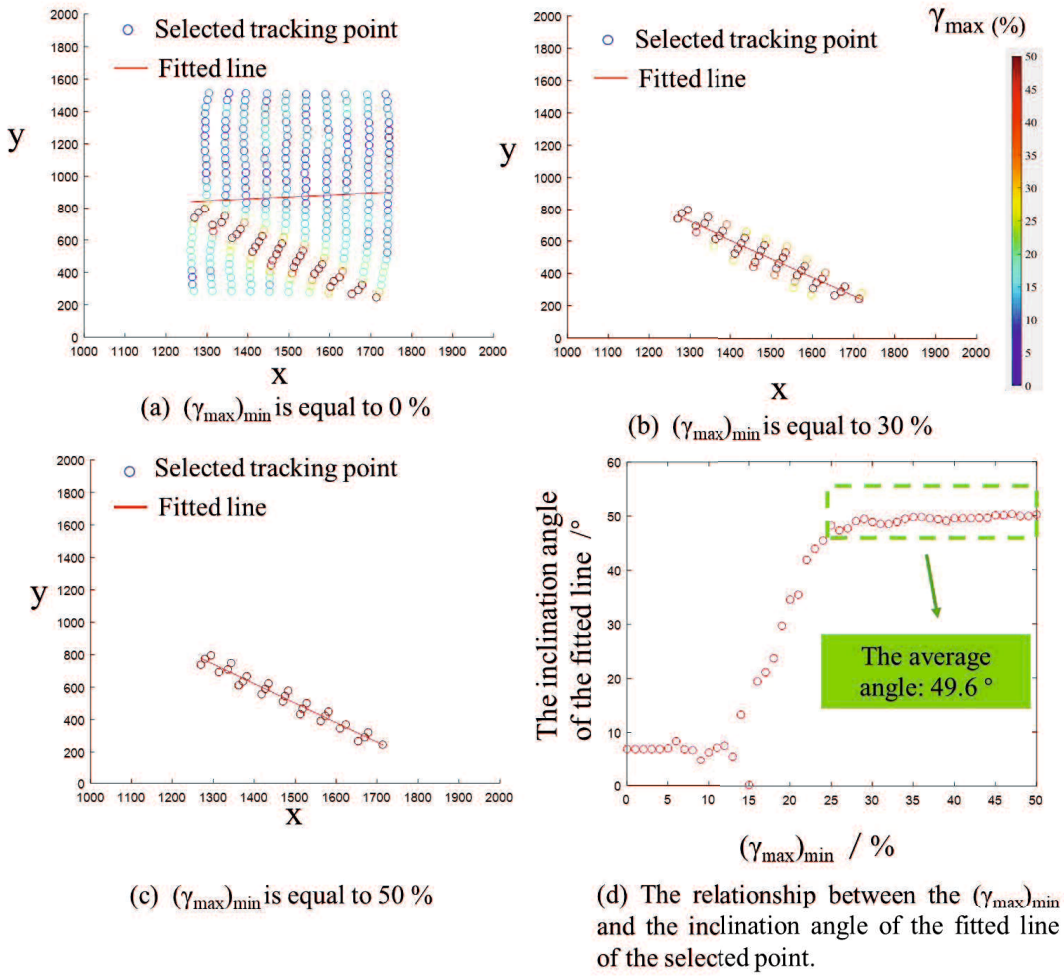

Figure 2-15. Schematic diagram of the acquisition process of the shear band angle.

Figure 2-15 illustrates the process of obtaining the angle of the shear band in more detail. As shown in **Figure 2-15 (a)**, when the minimum value of γ_{max} is set to 0%, all tracking points for PTV analysis can be obtained. Performing a linear fitting on these points can get a nearly horizontal straight line with an inclination angle of 9.5°. **Figure 2-15 (b and c)** show the minimum value of γmax are set to 30% and 50%, respectively. At this time, only tracking points with γ_{max} greater than or equal to 30% (**Figure 2-15 b**) and 50% (**Figure 2-15 c**) were selected. Similarly, the inclination angle of the line fitted by these points can be obtained as 48.9 and 49.6°, respectively. In this way, by controlling the minimum value of γ_{max}, we can get a series of

inclination angle values. **Figure 2-15 (d)** shows the relationship between the setting of the minimum value of γ_{max} and the inclination value of the fitted line of the selected point. It can be found that when the minimum of γ_{max} is greater than a certain value, the inclination angle of the fitted line remains steady. In this study, the average value of the inclination angle that remains steady in the final stage is considered as the angle of the shear band. This method can reduce the random errors, and facilitate the observation of the subtle changes in the shear band inclination during the shearing process. However, it must be noted that this method is not suitable for the bifurcation shear bands. At the same time, this method is also not applicable when comparing the angles of the shear bands of different samples with small differences.

3.2.4 Measurement of the thickness of the shear band

Since the shear band is not an ideal straight line, and it is difficult to identify the edge of the shear band, measuring the thickness of the shear band is considered a very tricky matter, although it is very important. *Khalid A. Alshibli et al.*, [1999] developed a method to measure the thickness of the shear band and verified its effectiveness. In this study, the same method was used to obtain the boundaries of the shear band.

There are 10 columns of tracking points in the analysis area of the shear band, and each column contains 36 tracking points. By formulas (2-10) and (2-11), the relative horizontal (x) and vertical (y) displacement of adjacent tracking points in the column can be calculated.

$$Rx_n = (x_{n+1} - x_n) - (x'_{n+1} - x'_n) \qquad (1 \le n \le 35) \qquad (2\text{-}10)$$

$$Ry_n = (y_{n+1} - y_n) - (y'_{n+1} - y'_n) \qquad (1 \le n \le 35) \qquad (2\text{-}11)$$

where the Rx_n and Ry_n are the relative displacements between the tracking points n and (n+1) in x and y-direction. (x_n, y_n) , (x'_n, y'_n) and (x_{n+1}, y_{n+1}) , (x'_{n+1}, y'_{n+1}) is the initial and during

the shearing process' coordinates of tracking points n and (n+1) in the column.

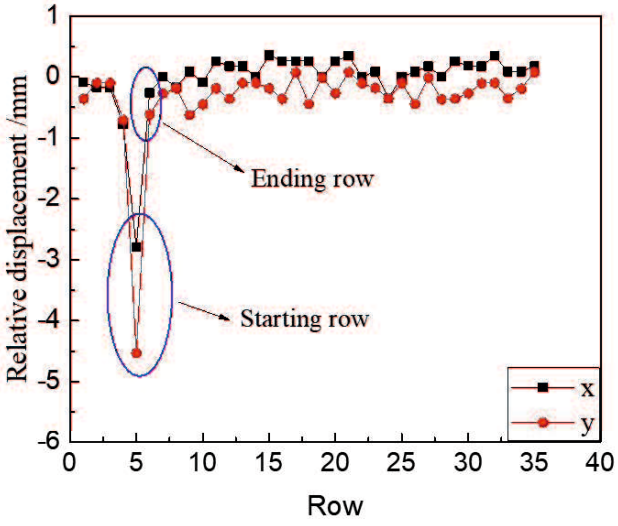

(a) The relative displacement result of one of the columns.

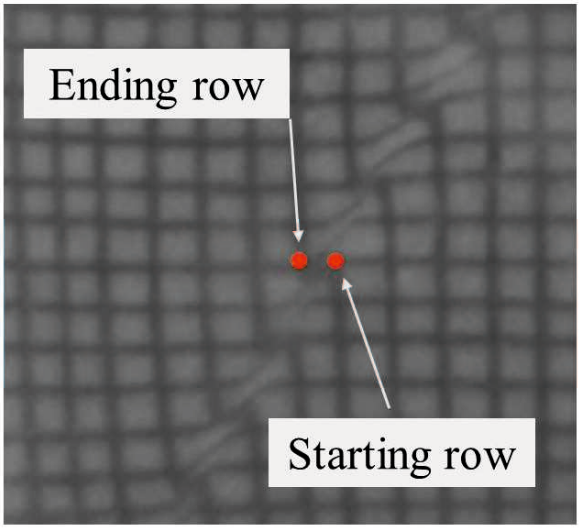

(b) The calculated start and end points of the shear band in the actual picture.

Figure 2-16. The schematic diagram of the boundary calculation process of the shear band.

Figure 2-16 shows the schematic diagram of the boundary calculation process of the shear band. **Figure 2-16 (a)** shows the calculation result of one of the columns. Since the relative displacement (x and y direction) of the tracking point located at the shear band position was much larger than

other positions, the start and end positions of the shear band can be determined. **Figure 2-16 (b)** shows the calculated start and ending points of the shear band in the actual picture. Finally, the thickness of the shear band can be obtained by the formula (2-12). Here, the average of all calculated shear band thickness was used as the final thickness of the shear band.

$$T_s = \left|\frac{(y_1-y_2)+\tan\theta(x_2-x_1)}{\sec\theta}\right| \quad (2\text{-}12)$$

where T_s and θ are the thickness and inclination angle of the shear band, respectively. (x_1, y_1) and (x_2, y_2) are the coordinates of the starting and ending points of the shear band.

3.2.5 The development of the shear band

Through the previously introduced method of measuring the angle and thickness of the shear band, **Figures 2-17** and **2-18** show the variations in the angle and thickness of the shear band of the host sand and hydrate-bearing sediment during the shearing process, respectively. Since the boundary of the shear band only can be accurately obtained after the principal stress difference of the sample reaches the peak value (peak strength), the starting point of the measurement of the angle and thickness of the shear band here was after the sample reached the peak strength. The four different shearing positions are shown in **Figures 2-17** and **2-18** correspond to stages 4 to 7 in **Figure 2-13**, respectively.

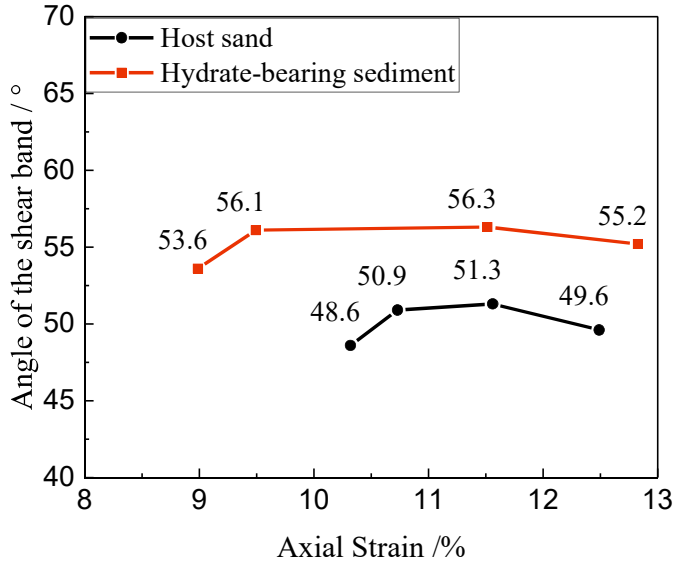

Figure 2-17. The variations in the angle of the shear band of the host sand and hydrate-bearing sediment during the shearing process.

From **Figure 2-17**, it can be found that the angle of the shear band of the hydrate-bearing sediment is higher than that of the host sand during the shearing process. *Yoneda et al*., [2013] also reported that the shear band of the methane hydrate-bearing sediment was steeper than that of the host sand. Regardless of the hydrate-bearing sediment or the host sand, after the sample reaches the peak strength, the measured shear band angle changes with the axial strain in the same law. The angle of the shear band of the sample first increased, then remained constant, and finally decreased slightly. It should be noted that the starting measurement of the angle of the shear band corresponds to the position where the principal stress difference (σ_1-σ_3) of the sample dropped the fastest after reaching the peak value, and the shear band has not yet fully formed. Such, a measurement method adopted in this study may cause a certain measurement error due to the lack of sufficient target tracking points.

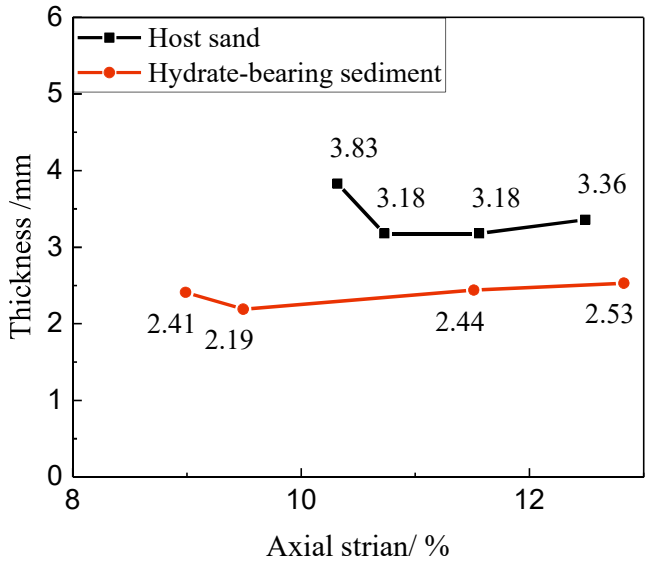

Figure 2-18. The variations in the thickness of the shear band of the host sand and hydrate-bearing sediment during the shearing process.

From **Figure 2-18**, it can be found that the thickness of the shear band of the hydrate-bearing sediment is smaller than that of the host sand. However, as the axial strain increases, the thickness of the shear band changes in the same way for the two different samples, first decreasing and then increased slightly. Similarly, the measured value of the starting point of the thickness of the shear band here may also cause a certain measurement error due to the lack of target tracking points. For the latter part of the shearing stage, the measured value of the thickness of the shear band increased slightly, which may also be caused by the fact that the shear band is not ideally straight.

Figure 2-19 shows the schematic representation of specimen shearing. When analyzing the shear band of the sample under plane strain shear conditions, as shown in **Figure 2-19**, it is generally assumed that the sample is divided into two rigid parts A and B by the shear band. Part B moves along the edge of part A at a fixed angle (θ_E). Figure 2-20 shows the displacement vectors on the observation plane of hydrate-bearing sediment at the end of the shear test (stage 7) in this study. In **Figure 2-20**, part A is subdivided into two parts, A_1 and A_2. It can be found that because

part A is not completely rigid, the displacements of parts A_1 and A_2 are quite different. The A_2 part has a clear tendency to shift to the lower right, which causes the shear band to no longer be ideal straight. At the same time, since the measurement value of the angle of the shear band is an average value, the shift of the A_2 part may cause the angle of the shear band to become smaller.

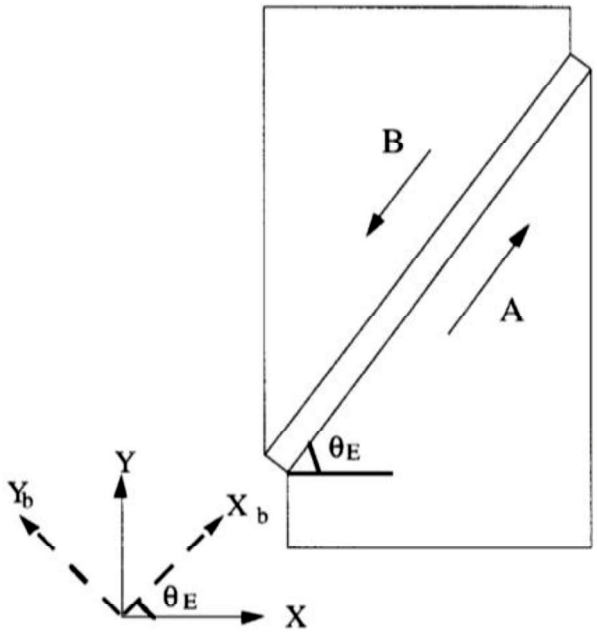

Figure 2-19. The schematic representation of specimen shearing ([*Khalid A Alshibli and Sture*., 1999]).

In summary, the shear band gradually develops completely after the principal stress difference of the sample reached its peak. The development of the shear band is closely related to the change in the strength of the sample. When the principal stress difference remains constant after the peak (residual strength), the angle of the shear band also almost remained constant. This implies that the angle of the shear band is closely related to the residual strength. In the later stage of the shear test, since the two parts of the sample separated by the shear band cannot be completely regarded as a rigid body, the shear band was no longer an ideal straight line and finally resulted in the change in the angle and thickness measurement of the shear band. Generally, the researcher may

choose the stage near the peak strength or the end of the shear test as the research stage of the shear band characteristics. It can be seen that near the peak strength, the shear band has a larger angle and smaller thickness.

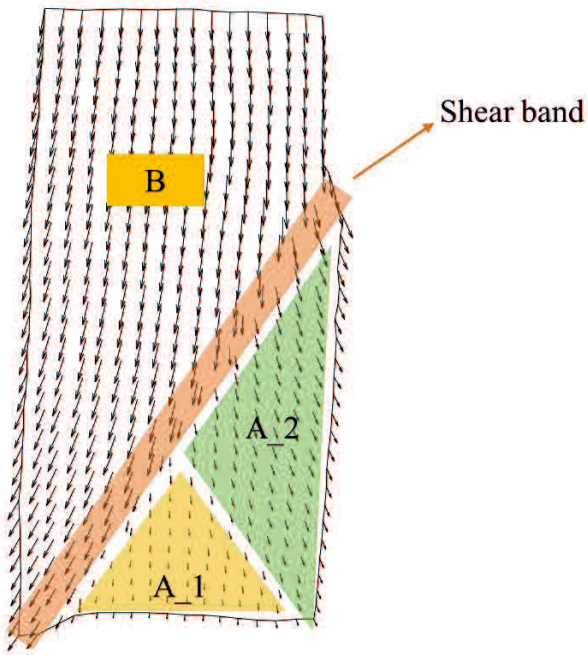

Figure 2-20. The displacement vectors on the observation plane of the hydrate-bearing sediment at the end of the shearing test.

4. Conclusion

Chapter 2 has shown the image information and some basic physical properties of the experimental materials that used in this thesis. And then, with the plane strain shear tests on the host sand and hydrate-bearing sediment, the development of the shear band has been studied. The following conclusions can be get:

(1) The permeability of Tc is far lower than that of the Toyoura and Tb.

(2) The hydrate-bearing sediment showed higher stiffness and strength. The volumetric strain of the hydrate-bearing sediment gradually changed from compressive to dilative during the shearing process, while the host sand only showed compressive behavior.

(3) The angle of the shear band of the hydrate-bearing sediment is higher than that of the host sand during the shearing process.

(4) Regardless of the hydrate-bearing sediment or the host sand, after the sample reaches the peak strength, the measured shear band angle changes with the axial strain in the same law: the angle of the shear band of the sample first increased, then remained constant, and finally decreased slightly.

(5) The thickness of the shear band of the hydrate-bearing sediment is smaller than that of the host sand. However, as the axial strain increases, the thickness of the shear band changes in the same way for the two different samples, first decreasing and then increased slightly.

5. Reference

Arthur, J., Dunstan, T., Al-Ani, Q., and Assadi, A. (1977). "Plastic deformation and failure in granular media." *Geotechnique*, 27(1), 53-74

Alshibli, K. A., and S. Sture (1999), Sand shear band thickness measurements by digital imaging techniques, *Journal of computing in civil engineering*, *13*(2), 103-109.

Alshibli, K. A., and S. Sture (2000), Shear band formation in plane strain experiments of sand, *Journal of Geotechnical and Geoenvironmental Engineering*, *126*(6), 495-503, doi:10.1061/(ASCE)1090-0241(2000)126:6(495).

Finno, R. J., W. Harris, M. A. Mooney, and G. Viggiani (1997), Shear bands in plane strain compression of loose sand, *Geotechnique*, *47*(1), 149-165.

Hutchinson, J. W., and V. Tvergaard (1981), Shear band formation in plane strain, *International Journal of Solids and Structures*, *17*(5), 451-470, doi:10.1016/0020-7683(81)90053-6.

Kajiyama, S., M. Hyodo, Y. Nakata, N. Yoshimoto, Y. Wu, and A. Kato (2017), Shear behaviour of methane hydrate bearing sand with various particle characteristics and fines, *Soils Found.*, *57*(2), 176-193, doi:10.1016/j.sandf.2017.03.002.

Roscoe, K. H. (1970). "The influence of strains in soil mechanics." *Geotechnique*, 20(2), 129-170

Li, D., Q. Wu, Z. Wang, J. Lu, D. Liang, and X. Li (2018), Tri-axial shear tests on hydrate-bearing sediments during hydrate dissociation with depressurization, *Energies*, *11*(7), doi:10.3390/en11071819.

Mühlhaus, H. B., and I. Vardoulakis (1987), The thickness of shear bands in granular materials, *Geotechnique*, *37*(3), 271-283, doi:10.1680/geot.1987.37.3.271.

Suzuki, K., T. Ebinuma, and H. Narita (2009), Features of methane hydrate-bearing sandy-

sediments of the forearc basin along the Nankai Trough: Effect on methane hydrate-accumulating mechanism in turbidite, *JOURNAL OF GEOGRAPHY-CHIGAKU ZASSHI*, *118*(5), 899-912.

White, M., T. Kneafsey, Y. Seol, W. F. Waite, S. Uchida, J. Lin, E. Myshakin, X. Gai, S. Gupta, and M. Reagan (2020), An international code comparison study on coupled thermal, hydrologic and geomechanical processes of natural gas hydrate-bearing sediments, *Mar. Pet. Geol.*, 104566.

Yoneda (2011), chanical and defbrmation characteristics of methane hydrate-bearing sediments in deep seabed, Yamaguchi University, Doctoral dissertation.

Yoneda, J., M. Hyodo, N. Yoshimoto, Y. Nakata, and A. Kato (2013), Development of high-pressure low-temperature plane strain testing apparatus for methane hydrate-bearing sand, *Soils Found.*, *53*(5), 774-783.

Chapter 3 Shear rate dependence characteristics

1. Introduction

Studying the mechanical properties of natural gas hydrate-bearing sediment under different conditions, and then accurately predicting the mechanical behavior of the reservoir during the exploitation of natural gas hydrates, is extremely helpful for the safe and sustainable exploitation of natural gas hydrate resources.

Previous researchers have reported the mechanical properties study results of hydrate-bearing sediments synthesized in the laboratory and in-suit sore samples [*Hyodo et al.*, 2013; *Lijith et al.*, 2019; *Yoneda et al.*, 2017]. It has been found that temperature, effective confining pressure, hydrate saturation, etc. have significant effects on the stiffness and shear strength of hydrate-bearing sediments. Some related constitutive models [*Klar et al.*, 2010; *Lin et al.*, 2015; *Miyazaki et al.*, 2012] have also been proposed to describe the stress-strain relationship of hydrate-bearing sediments under different conditions. In particular, some researchers have found that the stress-strain relationship of hydrate-bearing sediments showed significant time-dependent characteristics [*Miyazaki et al.*, 2008; *Miyazaki et al.*, 2011; *Yoneda et al.*, 2008]. For example, under high shear rate conditions, hydrate-bearing sediments have higher stiffness and strength. Different shear rates may be chosen by different researchers according to laboratory conditions when studying the mechanical properties of hydrate-bearing sediments. If the influence of shear rate on the experimental results is neglected, the relevant constitutive model may lose accuracy in predicting the mechanical behavior of natural gas hydrate reservoirs. In addition, the previous

studied on the shear rate dependence of hydrate-bearing sediments were all under triaxial conditions. However, under the plane strain condition, the failure mode of the sample is quite different from that under the triaxial condition. Some geological problems, such as submarine landslides, are more closed to plane strain conditions [*K. A. Alshibli and Sture*., 2000]. Therefore, it is very necessary to study the shear rate dependence characteristics of hydrate-bearing sediments under plane strain conditions.

In this chapter, to ensure that relevant research can be carried out safely and efficiently, firstly, plane strain shear tests were done on host sand samples and methane hydrate-bearing sediments (hydrate saturation was about 40%) under different shear rates conditions. After determining that methane hydrate-bearing sediments had significant shear rate dependence characteristics under plane strain conditions, three appropriate shear rates based on the results were selected to study the influence of other experimental conditions on the shear rate-dependent characteristics. Here, the hydrate saturation and fine particle content were chosen as the variable for the experiments. The specific research system in this chapter is shown in **Figure 3-1**.

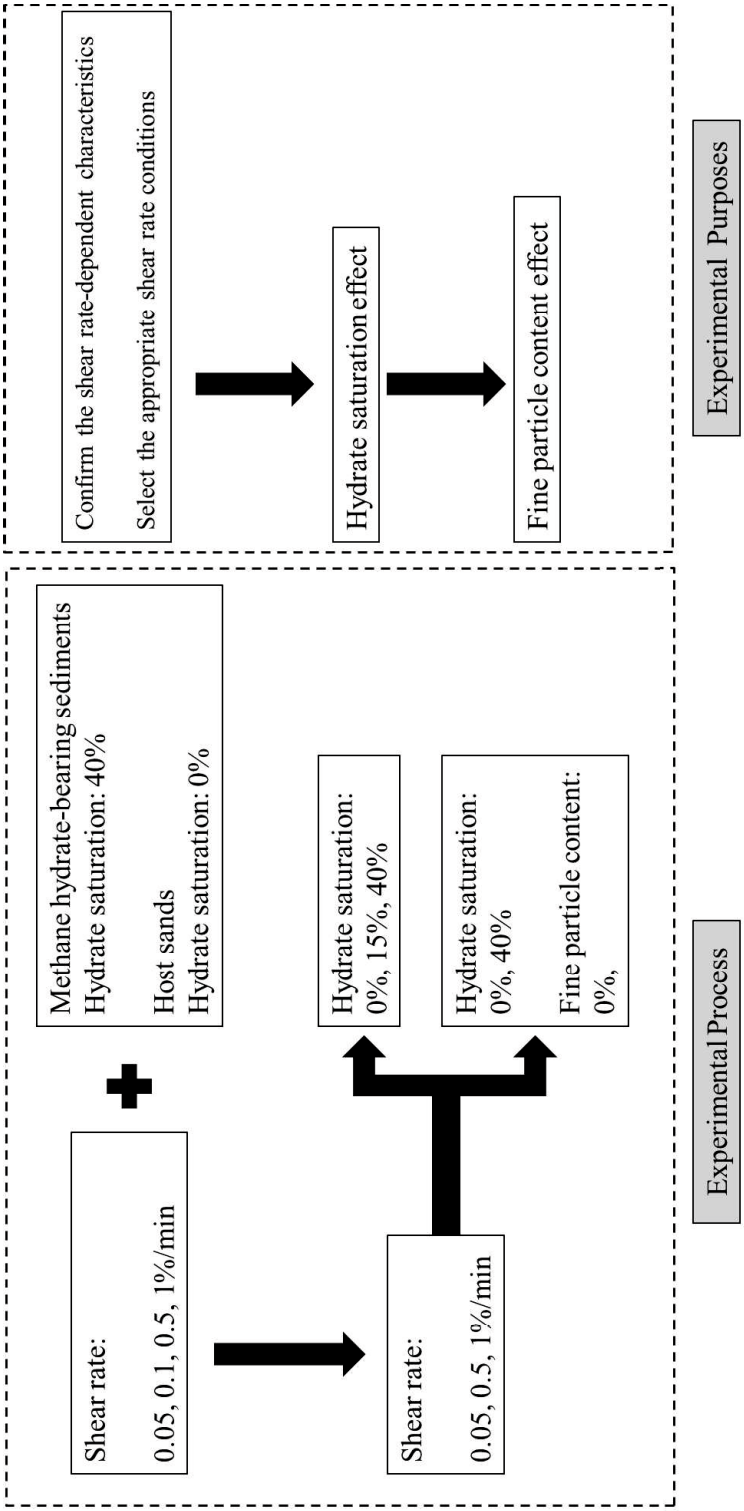

Figure 3-1. The specific research system in this chapter.

2. Shear rate-dependent characteristics

2.1 Shear rate-dependent characteristics under plane strain conditions

2.1.1 The experimental instrument

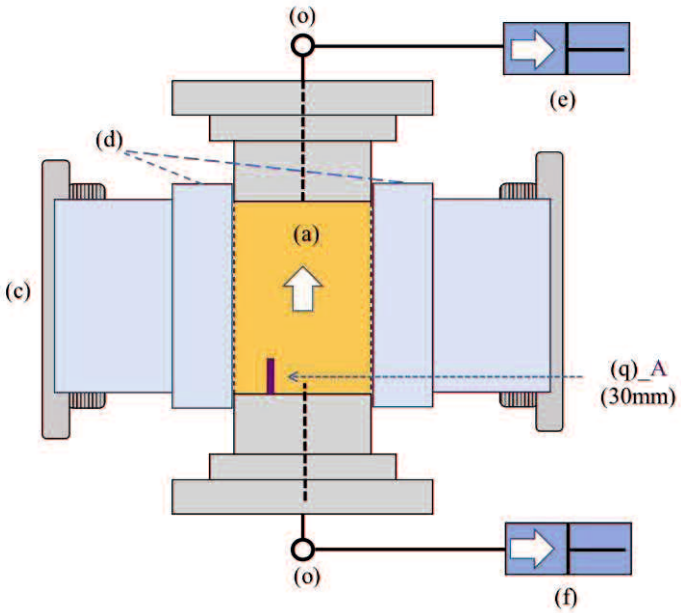

(a) Specimen; (c) observation window; (d) confining plate; (e) lower syringe pump for water;(f) lower syringe pump for gas; (o) pressure gauge; (q) thermocouple;

Figure 3-2. The schematic diagram of the main part of the experimental instrument.

The schematic diagram of the experimental instrument has been shown in Section 4.1 of Chapter 2. **Figure 3-2** only shows the schematic diagram of the main part of the experimental instrument. Only thermocouple A at the bottom was used to obtain the temperature information of the sample during the experiment.

2.1.2 Experimental procedures

First, Toyoura sand was mixed well with water for the target hydrate saturation (S_{MH} = 50%), and the moist sand was filled into a mold with the membrane in 12 layers. After that, the effective

confining pressure of the sample was set to 0.2 MPa, and the temperature was reduced to 287.15 K by the air conditioner. Methane gas was injected into the sample through pumps, and the pore pressure and confining pressure were gradually increased to 5.0 MPa and 5.2 MPa, respectively. During this process, the effective pressure of the sample was constantly maintained at 0.2 MPa. This temperature-pressure condition was kept constant for three days to generate the hydrate. Once the methane hydrate was formed, the excess gas in the pore space of the sample was replaced by water to get the water saturation condition. For the pure sand sample, all procedures were the same except there was no hydrate generation step. The pore pressure and confining pressure were gradually increased to 10.0 MPa and 13.0 MPa, respectively after the sample reached water saturation, and then the consolidation test was performed. The axial loading was applied to the specimen under drained conditions. The hydrate saturation was also calculated based on the total amount of decomposition gas measured after the experiment.

2.1.3 Experimental conditions

Table 3-1. Experimental conditions.

Test	Void Ratio	Hydrate saturation (%)	Confining pressure (MPa)	Pore Pressure (MPa)	Temperature (K)	Shear Rate (%/min)
S1	0.685	0	13.0	10.0	278.15	0.05
S2	0.658	0	13.0	10.0	278.15	0.1
S3	0.657	0	13.0	10.0	278.15	0.5
S4	0.696	0	13.0	10.0	278.15	1
M1	0.655	43.6	13.0	10.0	278.15	0.05
M2	0.694	41.2	13.0	10.0	278.15	0.1
M3	0.685	42.0	13.0	10.0	278.15	0.5
M4	0.717	43.7	13.0	10.0	278.15	1

The detailed experimental conditions of this section are shown in **Table 3-1**.

2.1.4 Stress-strain relationship

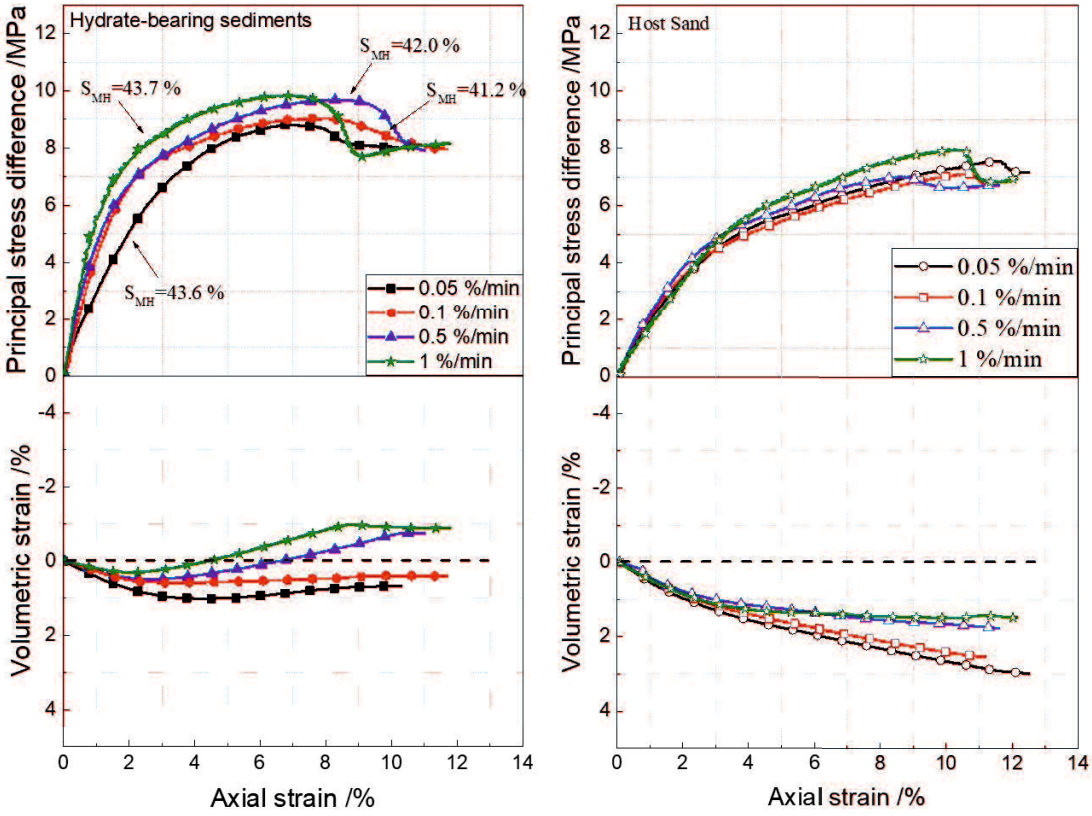

Figure 3-3. The stress-strain results of hydrate-bearing sediments and host sand samples with four different shear rates.

Figure 3-3 shows the stress-strain results of hydrate-bearing sediments and host sand samples with four different shear rates. As for the host sand samples, under different shear rate conditions, the relationship between the principal stress difference (σ_1-σ_3) and the axial strain (ε_a) of the sample did not change significantly. The volumetric strain (ε_v) of host sand samples was dominated by shear compression, and the volumetric compression strain becomes smaller, as the shear rate increased. As for the hydrate-bearing sediments, under a higher shear rate, the initial (σ_1-σ_3) of the sample increased faster. The volumetric strain of the hydrate-bearing sediments was initially dominated by slight shear compression, followed by volume expansion for all shear rate conditions. Besides, the volumetric dilatancy behavior of hydrate-bearing sediments becomes more significant in the final shear stage with the increase of shear rate. Compared with the host

sand samples, the stress-strain relationship of the hydrate-bearing sediments is more significantly affected by the shear rate.

2.1.5 Strength and stiffness

Peak strength is an important parameter when measuring the mechanical properties of hydrate-bearing sediments. And the peak strength of hydrate-bearing sediment is related to many factors, such as effective confining pressure, hydrate saturation, and temperature. To better compare the influence of shear rate on the peak strength of hydrate-bearing sediments from different studies, the experimental conditions of different researchers are shown in **Table 3-2**. In all studies, the hydrate saturation was about 40%, and the host sand was Toyoura sand.

Table 3-2. Comparison of experimental conditions of different researchers.

Researchers	Test type	Temperature (K)	Effective confining pressure (MPa)	Pore pressure (MPa)	Drainage condition	Gas hydrate type
This study	plane strain	278.15	3	10.0	drained	methane
Miyazaki et al. (2017)	triaxial	278	1	8.0	drained	methane
Iwai, H et al. (2018)	triaxial	274	2	10.0	undrained	carbon dioxide

Figure 3-4 shows the relationship between the peak strength $(\sigma_1-\sigma_3)_{max}$ and shear rate from this study and other works of literature. It can be found that the $(\sigma_1-\sigma_3)_{max}$ of the pure sand sample is not affected by the shear rate under all experimental conditions. On the contrary, the $(\sigma_1-\sigma_3)_{max}$ of hydrate-bearing sediment always increases with the increase of shear rate. To compare the sensitivity of the $(\sigma_1-\sigma_3)_{max}$ of the sample to the shear rate under different experimental conditions,

the slopes of the fitted line of the relationship between $(\sigma_1-\sigma_3)_{max}$ and shear rate are also marked. **Formula 3-1** shows the form of the fitted line:

$$q_{peak} = k \times \log_{10}(C_e) \tag{3-1}$$

where q_{peak} is the peak strength $(\sigma_1-\sigma_3)_{max}$, k is the slope of the fitted line, and C_e is the shear rate.

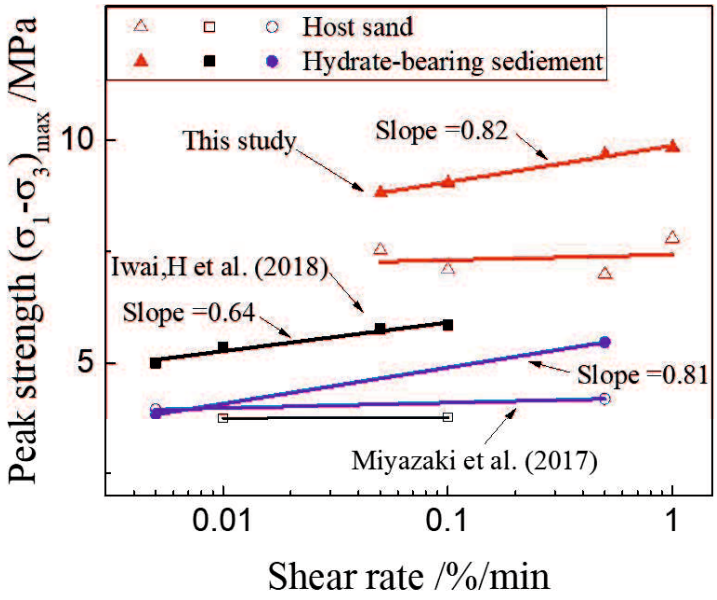

Figure 3-4. The peak strength $(\sigma_1-\sigma_3)_{max}$ of hydrate-bearing sediments and host sand samples.

The slope of the fitting line of the relationship between the $(\sigma_1-\sigma_3)_{max}$ and shear rates in this study is consistent with the result reported by *Miyazaki et al*., [2017]. This means that under plane strain conditions the peak shear strength of the methane hydrate-bearing sediments also has shear rate-dependent properties.

From **Figure 3-3**, it can be found that in the final stage of shearing, although the axial strain continues to increase, the principal stress difference and volumetric strain of the specimen remain unchanged. This stage is called the critical state. In this study, the residual strength was obtained in the critical state [*Schofield* and *Wroth*, 1968]. The specific location to obtain the residual strength is shown in **Figure 3-5**. And **Figure 3-6** presents the relationship between the residual

strength and shear rate of two different samples in this study. It can be seen that the residual strength of the host sand and hydrate-bearing sediment did not be affected by the shear rate. The presence of methane hydrate increased the residual strength can also be observed.

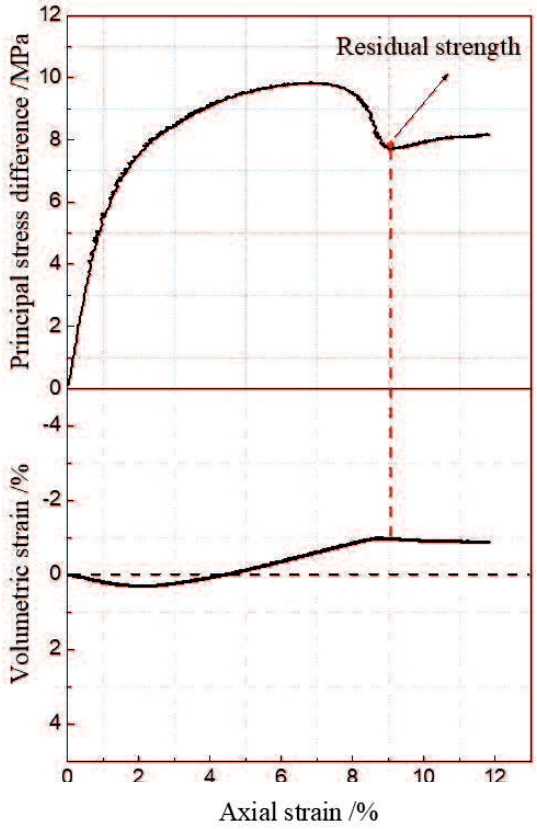

Figure 3-5. The schematic diagram of obtaining the residual strength.

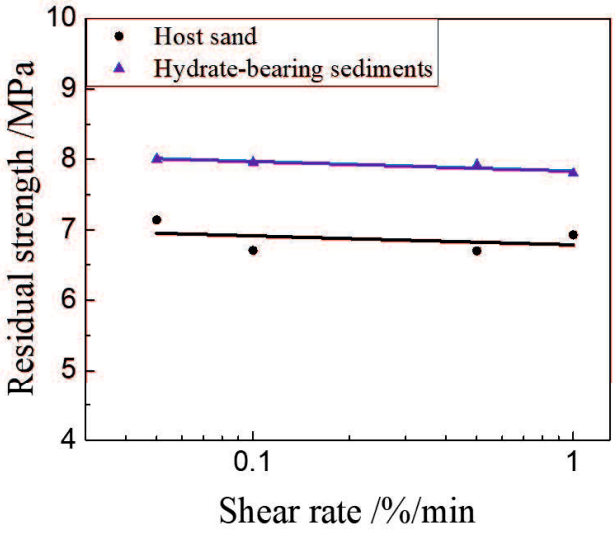

Figure 3-6. The relationship between the residual strength and shear rate of host sand samples and hydrate-bearing sediments.

The secant Young's modulus (E_{50}) can be regarded as an index to measure the difficulty of elastic deformation of a material [*Duncan* and *Chang*, 1970]. The E_{50} can be obtained by **Formula 3-2**:

$$E_{50} = \frac{(q_{peak})/2}{\varepsilon_a} \tag{3-2}$$

where the E_{50} is the secant Young's modulus, q_{peak} is the peak strength $(\sigma_1-\sigma_3)_{max}$, and ε_a is the axial strain corresponding to the half of peak strength. **Figure 3-7** shows the schematic diagram of obtaining the secant Young's modulus. **Figure 3-8** shows the secant Young's modulus (E_{50}) of hydrate-bearing sediments and host sand under different shear rates. It can be observed that the E_{50} increased with the rise in shear rate for hydrate-bearing sediments. This implies that a high shear rate leads to a higher stiffness for hydrate-bearing sediments. This behavior is attributed to the grains in the hydrate-bearing sediment, which gets densified and their relative movement was limited in the high shear rate. As for the host sand, no obvious difference in the E_{50} was observed at different shear rates.

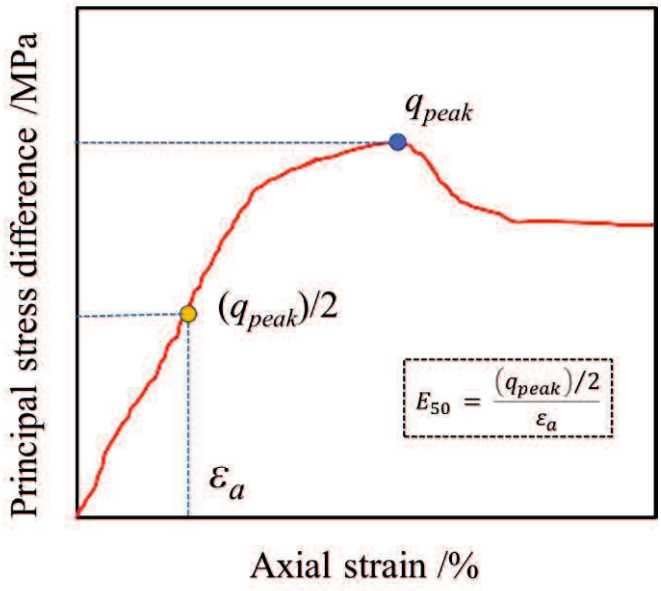

Figure 3-7. The schematic diagram of obtaining the secant Secant Young's modulus (E_{50}).

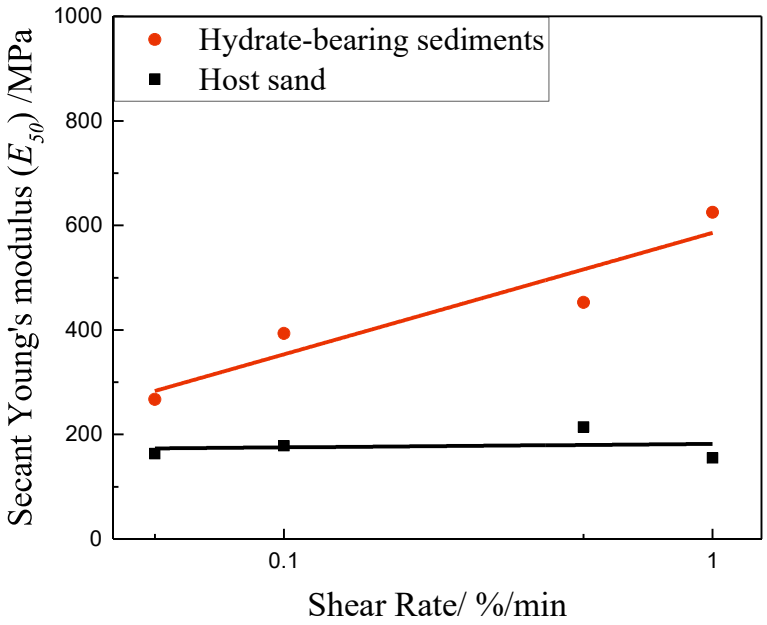

Figure 3-8. The Secant Young's modulus (E_{50}) of hydrate-bearing sediments and host sand under different shear rates.

2.1.6 Localized deformation

Firstly, the specimen images of the host sand and hydrate-bearing sediments with shear rates of 0.05 %/min and 0.5 %/min during the shearing tests are shown in **Figures 3-9** and **3-10**. From Figures 3-9 and 3-10, it can be found that the shear band gradually appeared with the increase in axial strain for all cases. However, the clear shear band appeared at different axial strains and the appearance characteristics of the shear band seem also affected by the type of the samples and the shear rates.

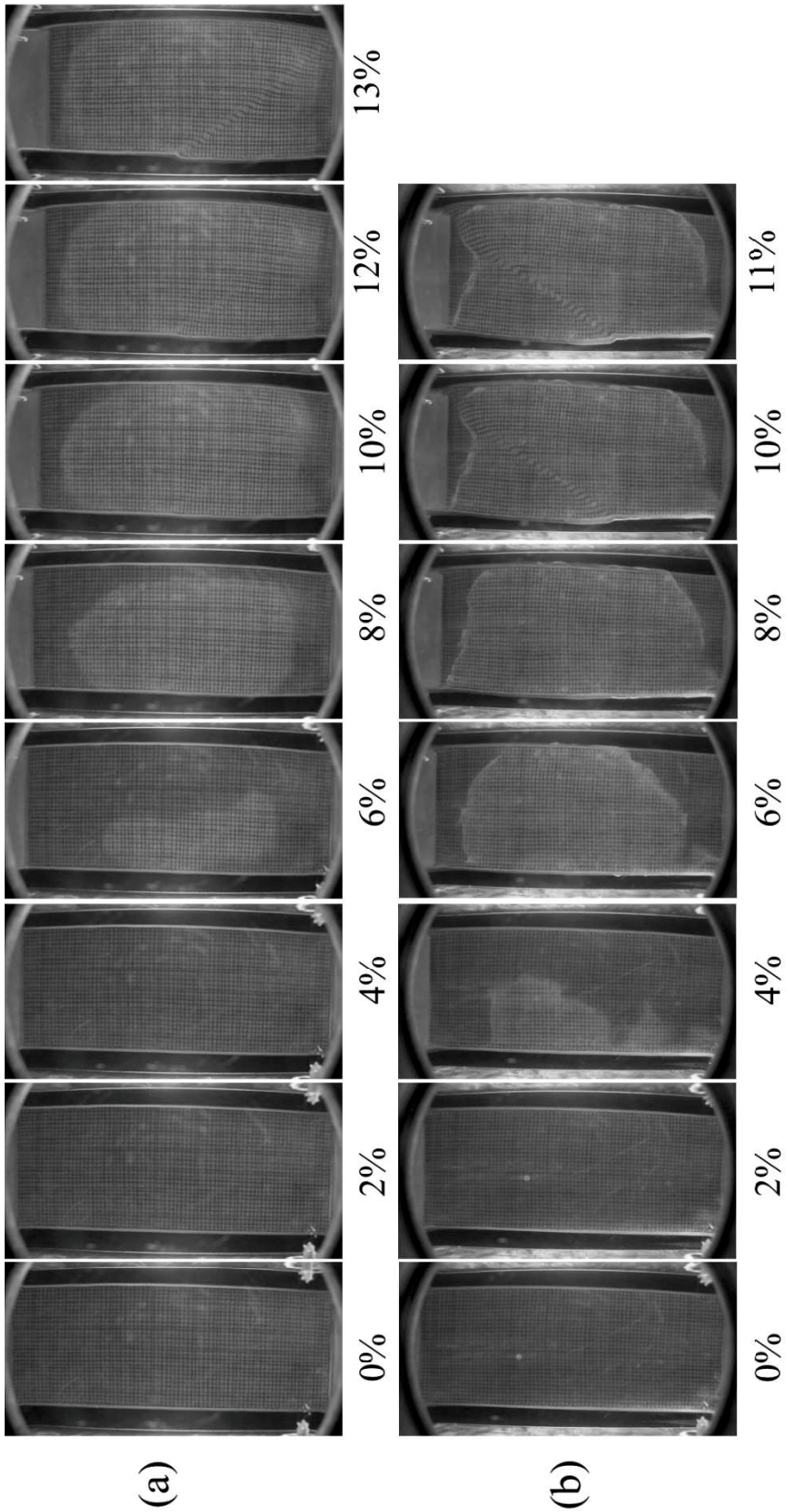

Figure 3-9. The specimen images of the host sand with the shear rates of 0.05 %/min (a) and 0.5 %/min (b) during the shearing tests.

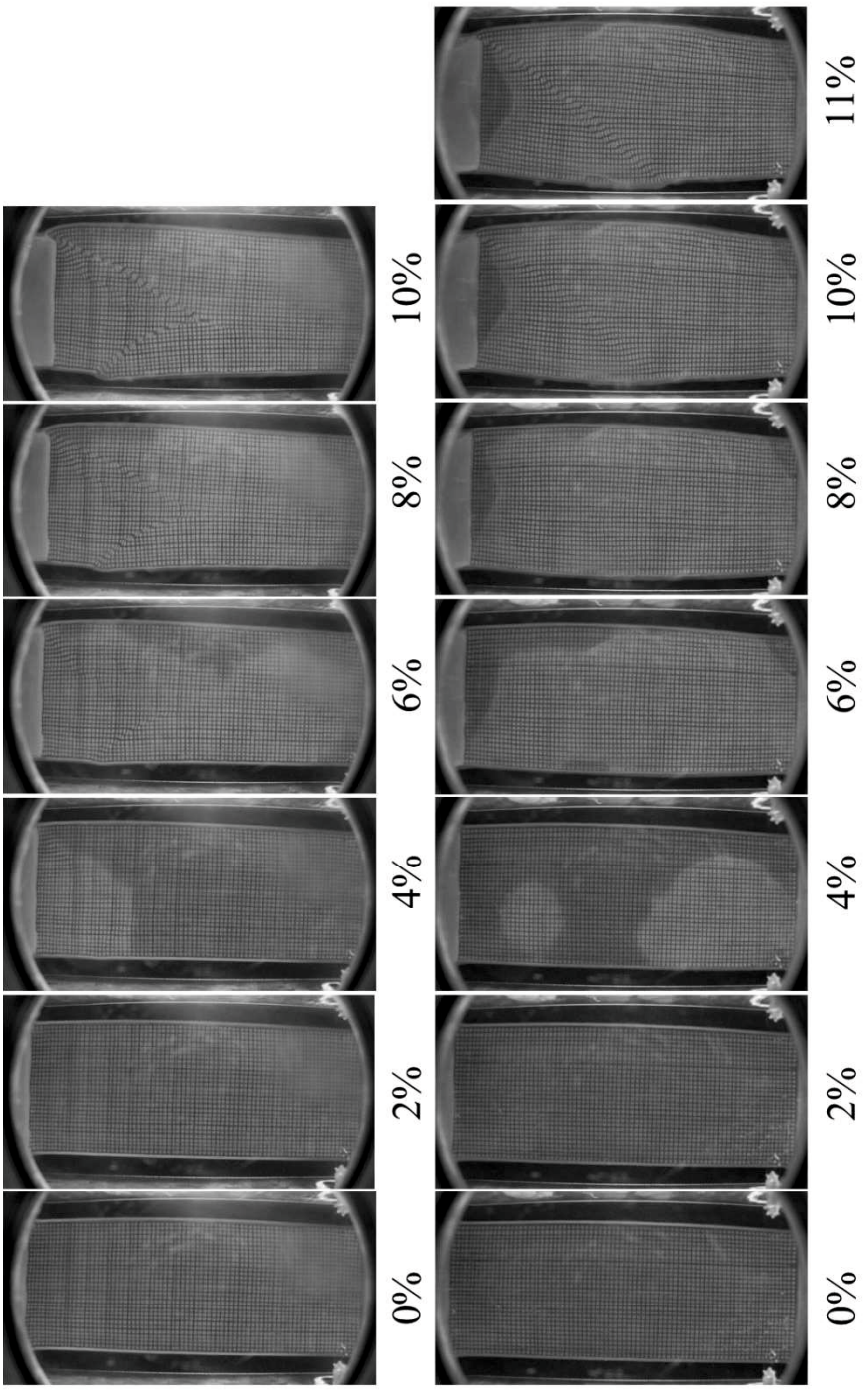

Figure 3-10. The specimen images of the hydrate-bearing sediment with the shear rates of 0.05 %/min (a) and 0.5 %/min (b) during the shearing tests.

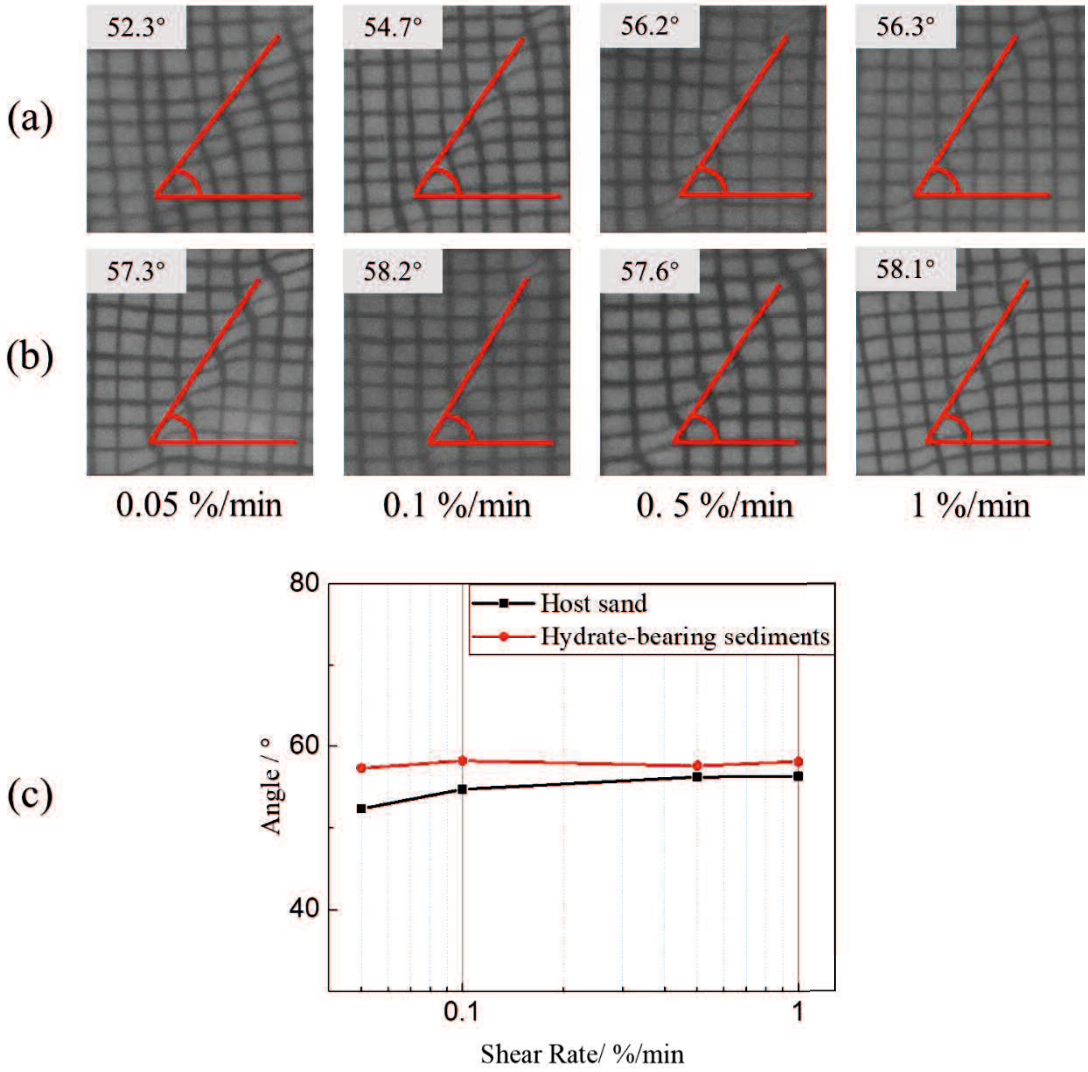

Figure 3-11. The shear band angle of (a) host sand and (b) hydrate-bearing sediments at different shear rates. (c) The angle of the shear band of host sand and hydrate-bearing sediments at different shear rates [*Wu et al*., 2020].

Considering the complexity of the shape of the shear band, the method reported by other researchers [*Khalid A Alshibli and Sture*, 1999] was used to measure the angle of the shear band here. In this study, after the sample experienced peak strength $(\sigma_1-\sigma_3)_{max}$, the location where $(\sigma_1-\sigma_3)$ decreased faster was selected to measure the angle of the shear band. A similar research method can also be found in previous reports [*Kajiyama et al.*, 2017; *J. Yoneda et al.*, 2013]. It

should be noted that the angle here is an average value, as the shear band is not an ideal straight line. **Figure 3-11** shows the shear band angle of the host sand and hydrate-bearing sediments. It can be observed that the shear band angle of the hydrate-bearing sediments was around 57.7° and no remarkable change was seen in the angle with an increase in the shear rate. Besides, there was a slight increase in the shear band angle of the host sand at a higher shear rate (from 52.3° to 56.3°), and the shear band angle of pure sand samples was lower than that of the hydrate-bearing sediments at all shear rates in this study. It has been reported that the shear band angle tends to increase with higher hydrate saturation [*Yoneda, J et al.*, 2013]. The effect of the dilation angle and cementation mechanisms of hydrate with the sand may result in a complex shear band angle prediction [*Soga et al.*, 2006; *Vaid et al.*, 1981; *Waite et al.*, 2009]. It has been reported that the angle of the shear band (θ_A) was related to the internal friction angle (ϕ_m) [Roscoe, K. H., 1970], as presented by **Formula (3-3)**:

$$\theta_A = \frac{\pi}{4} + \frac{1}{2}\,\phi_m \tag{3-3}$$

Based on this expression, it can be inferred that within the shear rate range of this study, the internal friction angle at the failure of hydrate-bearing sediments can be regarded as a constant.

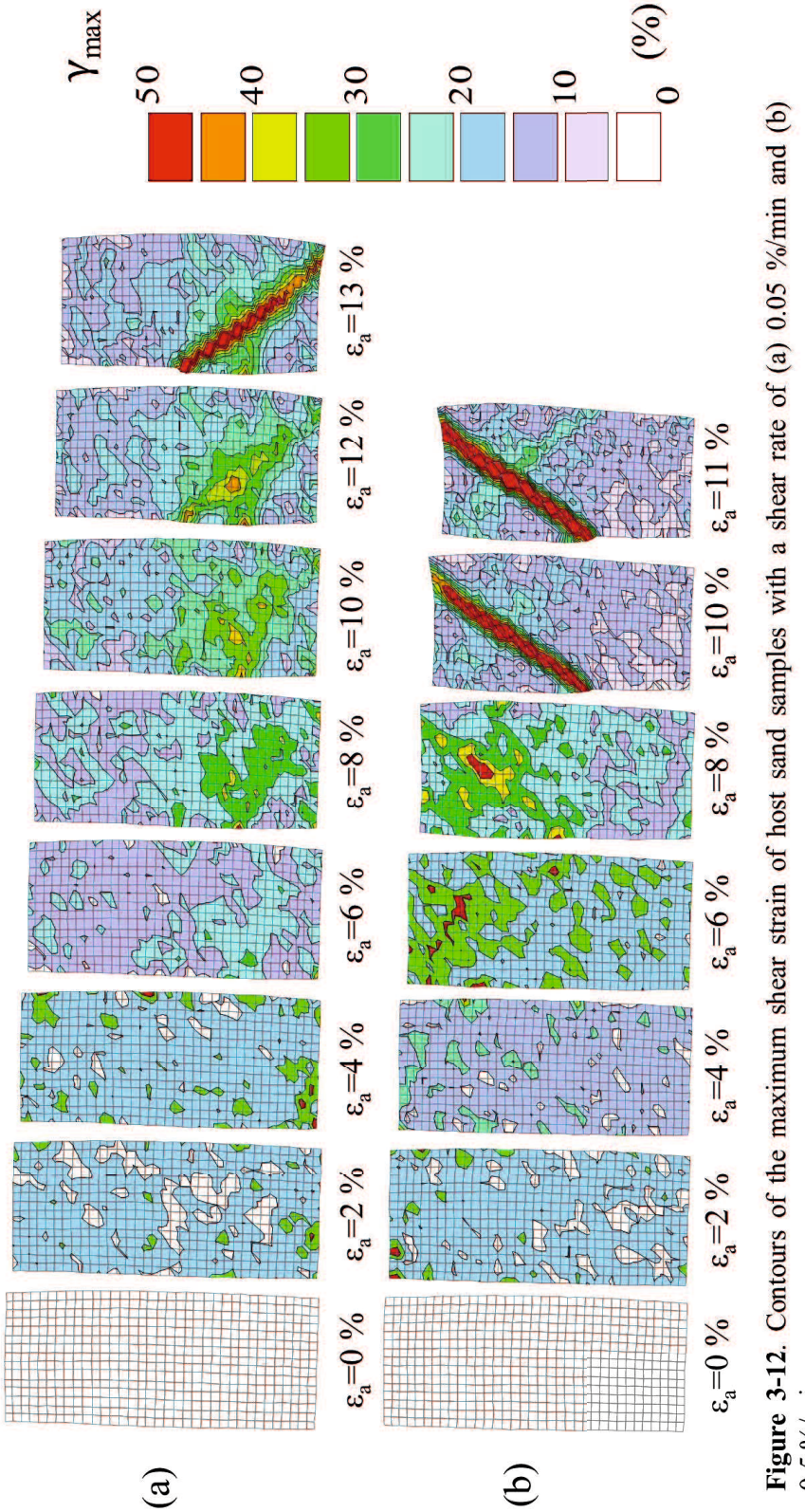

Figure 3-12. Contours of the maximum shear strain of host sand samples with a shear rate of (a) 0.05 %/min and (b) 0.5 %/min.

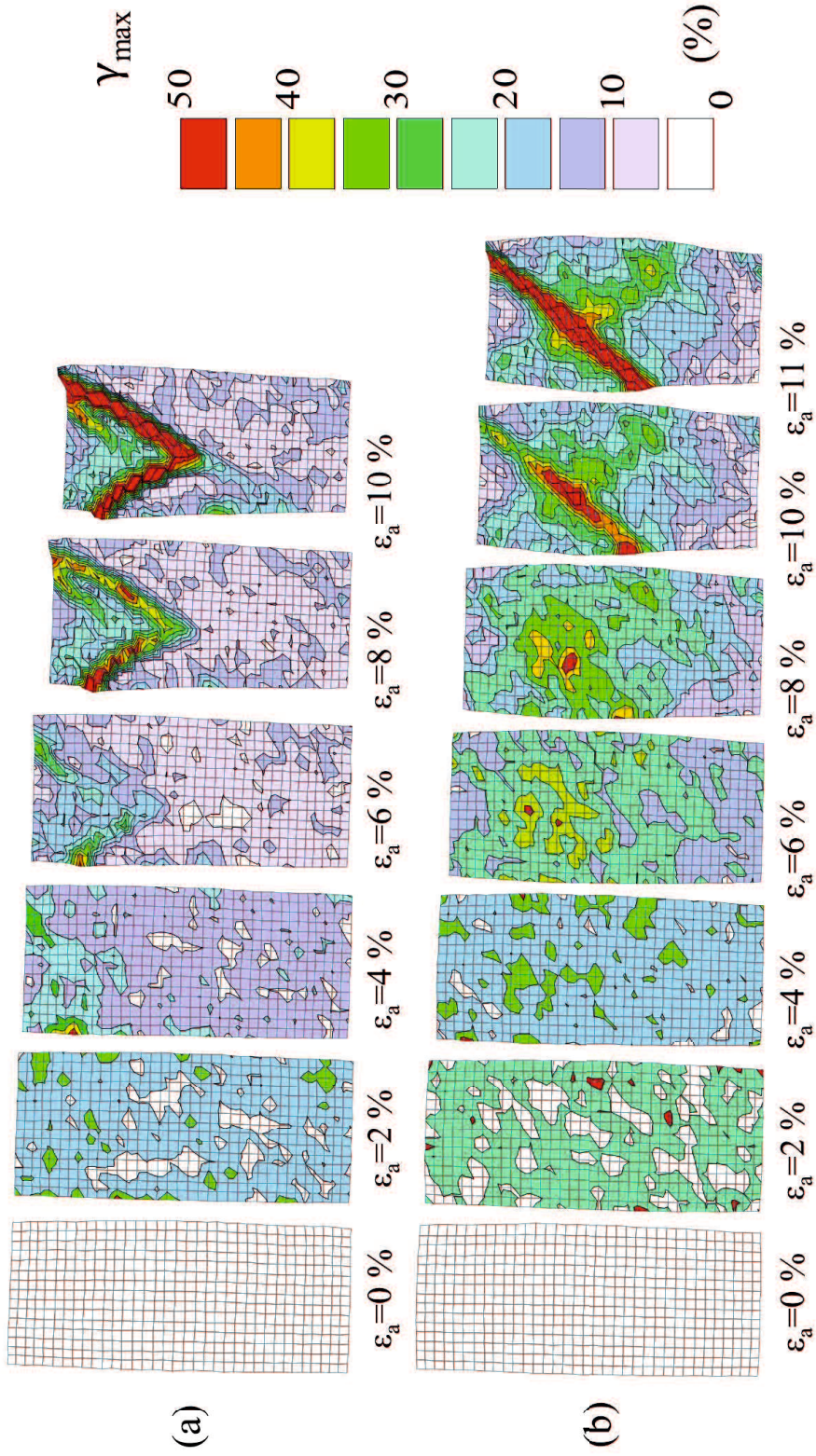

Figure 3-13. Contours of the maximum shear strain of the hydrate-bearing sediments with a shear rate of (a) 0.05 %/min and (b) 0.5 %/min.

Figures 3-12 and **3-13** show the contours of the maximum shear strain of the host sand samples and hydrate-bearing sediments during the shear test, respectively. In the case of host sand samples, at a higher shear rate (0.5 %/min), the localized strain concentration appeared earlier. Conversely, as for the hydrate-bearing sediments, the significant local strain concentration (shear band) occurs at an axial strain of about 10% at a shear rate of 0.5 %/min, and 8% at a shear rate of 0.05 %/min. besides, the shear rate also has different effects on the large shear strain contour (γ_{max} > 40%) distribution of the two types of specimens. In the case of hydrate-bearing sediments, at a low shear rate (0.05 %/min), the large shear strain contours appeared not only in the interior of the shear band (45% < γ_{max} < 50% in this study) but also around the shear band. As the shear rate was increased to 0.5 %/min, the large shear strain contour became more concentrated inside the shear band. As for the host sand samples, at the two different shear rates, the large shear strain contours were observed around the shear band.

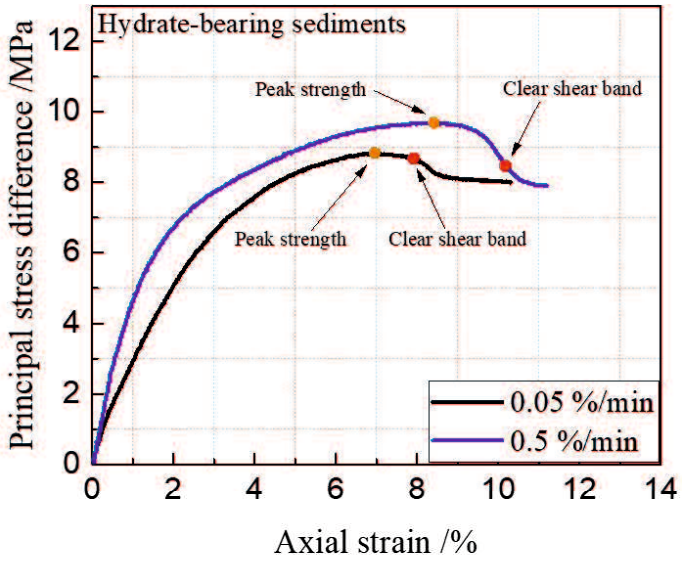

Figure 3-14. The appearance position of the clear shear band of hydrate-bearing sediments under different shear rates.

Figure 3-14 shows the appearance position of the clear shear band of hydrate-bearing sediments

under different shear rates. As for the hydrate-bearing sediment under the shear rate of 0.05%/min, the clear shear band appeared after the peak strength closely. However, the appearance of the clear shear band of hydrate-bearing sediment under the shear rate of 0.5%/min more late after the sample reached the peak strength. It seems that the higher shear rate delayed the appearance of the shear band. Previous studies [*Desrues et al*., 2004; *Lade et al*., 2014; *Kajiyama et al*., 2017] have found that for non-cemented sands, the appearance of clear shear bands may occur before the sample reaches its peak strength. For cemented sand and hydrate-bearing sediments, the shear band appeared after the sample reached its peak strength. It has been reported that cementation in the sand delayed the appearance of shear bands. Based on this, the possible reason for the appearance of the shear band has been delayed under a higher shear rate is that the cementation in the sand specimens restricts the movement of the particles more significantly under a high shear rate.

Figures 3-15 and **3-16** show the contours of the volumetric strain of the host sand and hydrate-bearing sediments with shear rates of 0.05 %/min and 0.5 %/min. In this study, the local volume expansion and compression of the specimen during the shear test were analyzed separately with the PTV technique, as it has been reported that volume compression and expansion simultaneously exist at the shear band area under plane strain shear tests [*Kato and Nakata*, 2015]. In the case of the host sand (see **Figure 3-15**), the compression behavior is more significant at a lower shear rate (0.05 %/min). When the shear rate was increased, the shear band area showed obvious expansion behavior. On the contrary, for the hydrate-bearing sediments (see **Figure 3-16**), under the two different shear rate conditions, more significant local expansion behavior can be observed. Especially for the higher shear rate condition (0.5 %/min), the area of local expansion was wider, and the local compression behavior was almost not observed. *Yoneda et al*., [2013] reported that the existence of methane hydrate in the pore spaces results in a marked

increase in the dilative volumetric strain in the shear band. From **Figures 3-15** and **3-16**, it can be found that the increase in shear rate can significantly improve the local volume expansion behavior of the samples, especially for the hydrate-bearing sediments. This implies that under the higher shear rate, the relative movement of particles tends to increase the pore space inside the sample, which in turn causes the local volume of the sample to expand. The possible explanation is that at a higher shear rate, the movement type of the particles was restricted, the structure reorganization between the particles became difficult, and the fine particles did not have enough time to fill the newly created pores, causing local volume expansion.

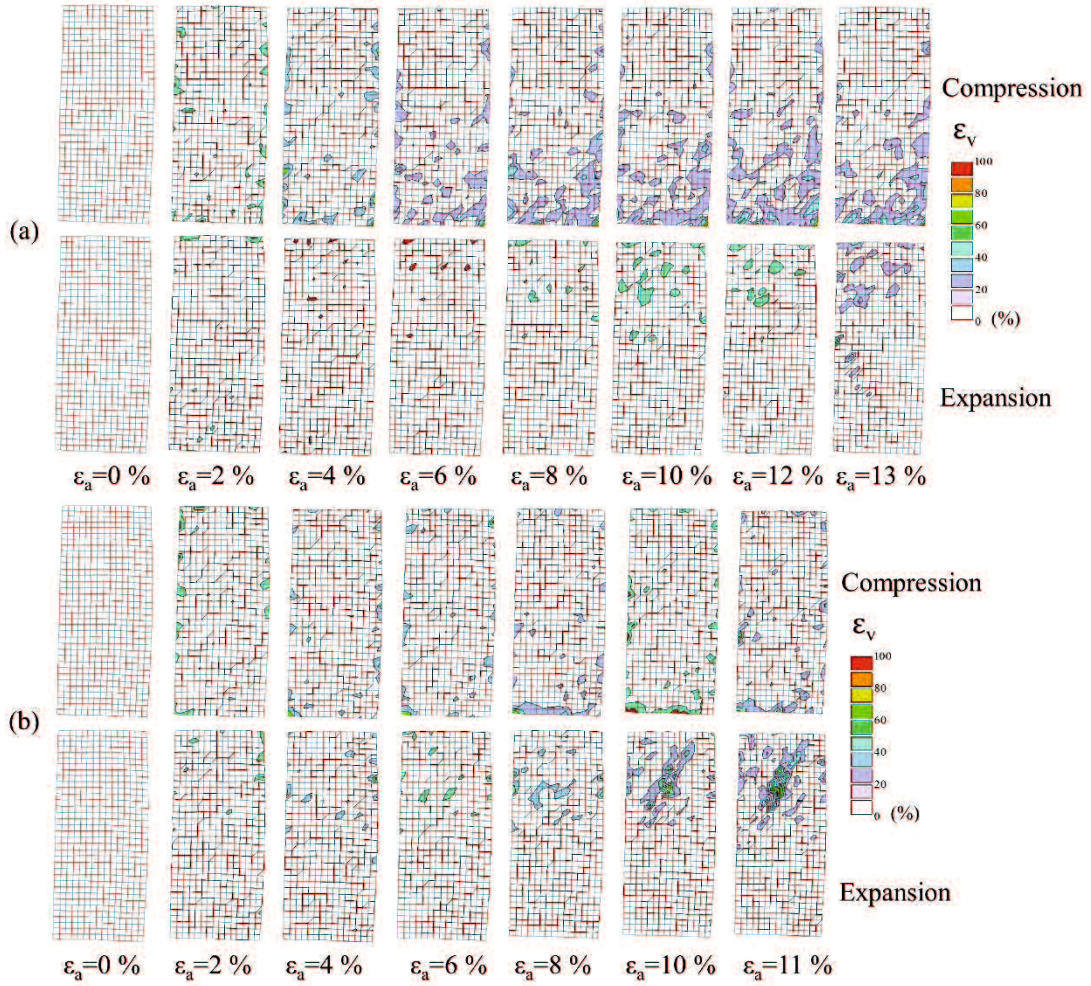

Figure 3-15. Contours of the volumetric strain of host sand samples with a shear rate of (a) 0.05 %/min and (b) 0.5 %/min.

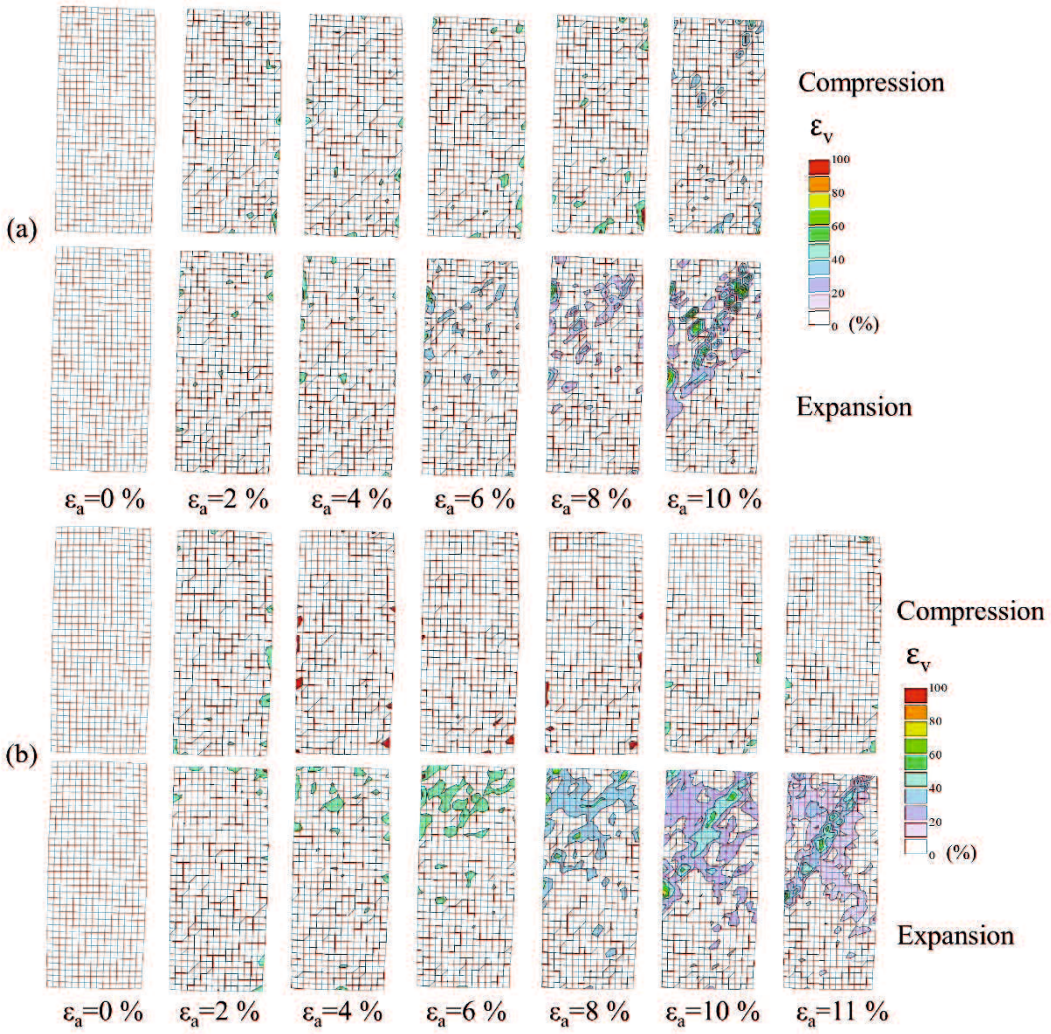

Figure 3-16. Contours of the volumetric strain of the hydrate-bearing sediments with a shear rate of (a) 0.05 %/min and (b) 0.5 %/min.

2.1.7 Shear rate-dependent mechanism of hydrate-bearing sediments

Table 3-3 summarizes the shear rate-dependent characteristics of hydrate-bearing sediments. Since the mechanical properties of host sand specimens are independent of the shear rate, it implies that hydrates play an important role in the shear rate dependence of sediments. Based on the mechanism that hydrates enhance the mechanical properties of sediments, *Yoneda, J et al.*,

[2018] suggested considering the shear rate-dependent mechanism of hydrate sediments from two aspects. The first is the hydrate itself, and the second is the friction mechanism between the hydrate, pore fluid, and sediment particles. And this shear rate dependence has been considered as the viscous behavior of hydrate-bearing sediments.

Table 3-3. Summary of the shear rate dependence characteristics of hydrate-bearing sediments.

Hydrate-bearing sediment	Peak strength	Residual strength	Stiffness	Global volumetric strain	Shear band (Local deformation)
Plane strain shear (This study)	+	x	+	More significant volumetric expansion under a higher shear rate	● Angle: x ● Appearance: be delayed under a higher shear rate; ● Maximum shear strain: + ● Volumetric strain: more significant volumetric expansion under a higher shear rate;
Triaxial shear	+	*	*	*	*

+: positive dependence; x: independence; *: no information;

Triaxial shear test results: [Miyazaki, K et al., 2011 and 2017; Iwai, H et al., 2018; Yoneda, J et al., 2018]

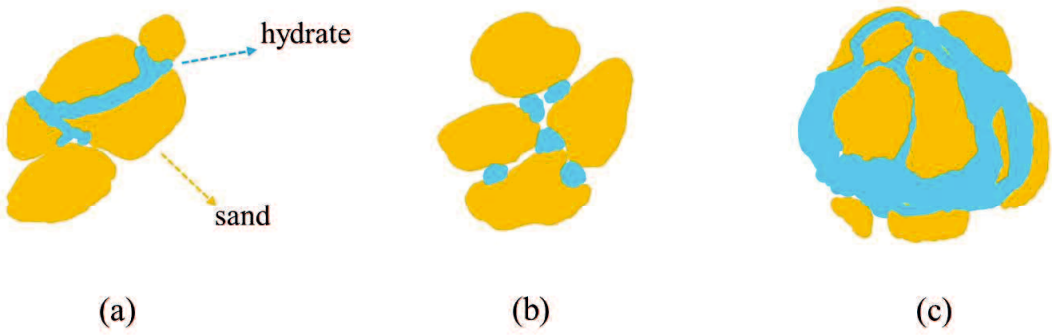

Figure 3-17. Schematic of different morphologies of hydrate-bearing sediments in this study. (a) The hydrate cemented sand particles; (b) The hydrate particles in the pore space of the sand particles; (c) Hydrate and sand particles formed clusters;

The structure of pure methane hydrate is similar to ice, and the shear rate dependence characteristics of the pure methane hydrate are more significant than that of ice [*Hawkes* and *Mellor*., 1972; *Jones* et al., 1997; *Durham* et al., 2003]. Under a low shear rate, the grain boundaries diffusion or cracking in ice, and during the shearing process, the local high pressure

generated by the contact points of the grains may melt the ice, resulting in lower strength and stiffness [*Dillon* and *Andersland*., 1967]. The shear rate dependence mechanism of the pure methane hydrates may be similar to the ice, but due to the stronger thermodynamic stability of the hydrate under high-pressure conditions, the high pressure melting phenomenon may not occur in the methane hydrate. Frozen sand also has shear rate-dependent characteristics. Under the condition of low shear rate, the creep behavior of the ice, and the melting water produced by the local high pressure has sufficient time to migrate within the specimen eventually resulted in the decrease in the strength and stiffness of frozen sand [*Parameswaran*., 1980]. According to the results of previous studies [*Yoneda, J* et al., 2016; *Kato, A* et al., 2016], the preparation method of the hydrate-bearing sediments used in this study, most of the hydrates and sand particles were cemented, and a small number of hydrates existed in the pore space between the sand particles or formed clusters structure with sand particles. **Figure 3-17** shows the schematic of different morphologies of hydrate-bearing sediments in this study. **Figure 3-18** shows the tomographic image and the related conceptual model of the structure of the hydrate-bearing sediments. Even under stable conditions, a liquid layer of several microns between the hydrate and the sand particles has been observed [*Chaouachi, M* et al., 2015]. It has been assumed that if the liquid that trapped between the hydrate and the sand particles was drained during the shearing process, the movement of the liquid layer may also cause the shear rate-dependent characteristics of the sample [*Yoneda, J* et al., 2018]. Based on the above analysis, the following explains the possible mechanism of shear rate dependence of hydrate-bearing sediments under plane strain conditions:

Peak strength and stiffness: Under a lower shear rate condition, the hydrate that cemented with sand particles or existed in the pore space of the sand particles may have lower strength and stiffness due to the grain boundaries diffusion or cracking. And the clusters composed of hydrate and sand particles have sufficient time to turn over and move, it did not cause great resistance to

the movement of the surrounding particles. The irregularity of the shear band shape is also considered to be related to the movement of the clusters [*Yoneda, J* et al., 2016].

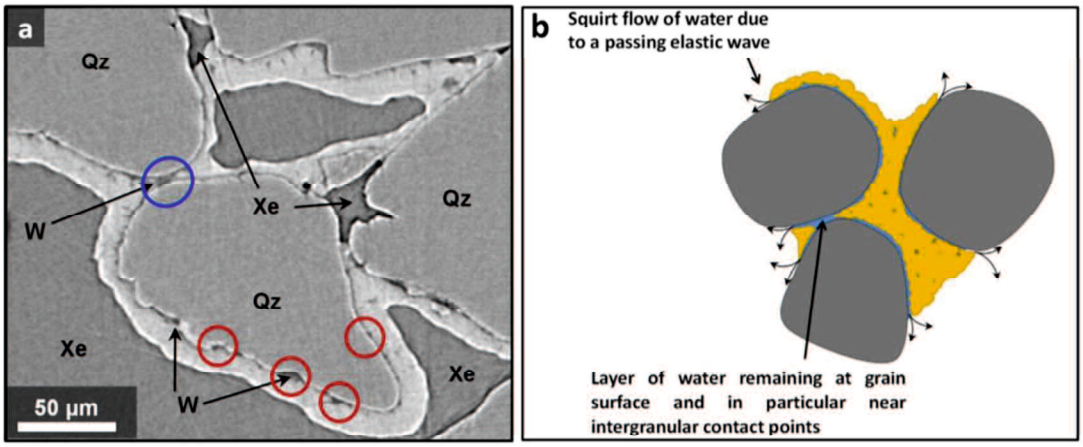

Figure 3-18. The tomographic image (a) and the related conceptual model (b) of the structure of the hydrate-bearing sediments [*Chaouachi, M* et al., 2015].

Residual strength: The residual strength of hydrate-bearing sediments was independent of the shear rate in this study. In the final stage of the shearing test, the strain of the specimen is concentrated in the shear band area, and the residual strength is closely related to the angle and friction characteristics of the shear band area. The angle of the shear band was independent of the shear rate in this study, and the friction characteristics of the shear band area are related to the hydrate saturation, effective confining pressure, particle size, and shape, etc., independent of the strain rate, so the residual strength was not affected by the shear rate. As mentioned in Chapter 2, the angle of the shear band remains almost unchanged when the sample reaches the stage of residual strength. Since the internal friction angle is directly related to the angle of the shear band [*Alshibli, K. A,* and *Sture, S*., 2000], it can also be said that the internal friction angle of the sample is independent of the shear rate. Previous studies have also found that within a certain strain rate range, although the peak strength of the soil increased with the increase of the strain rate, the internal friction angle was independent of the strain rate [*Stafford, J,* and *Tanner, D*., 1983].

Volumetric strain: The volumetric strain of the hydrate-bearing sediment was affected by the movement of the sand particles inside the sample. Under the condition of high shear rate, the movement mode of the sand particles was restricted, and the particle structure did not have enough time to complete the reorganization, resulted in more significant volumetric expansion; The cementation of the sand particles by the hydrate and the hydrate filled in the sand pores can also make the volumetric expansion effect of the sample more significant under the condition of high shear rate.

Shear band: Previous studies have found that due to the cementation of hydrates on sand particles, the appearance of shear bands may be delayed [*Kajiyama* et al., 2017]. Under the condition of a high shear rate, the movement of cementation particles was restricted, which may be the reason for the delayed appearance of shear bands.

2.2 The effects of hydrate saturation and fines content

Current research on core samples and field tests has found that the hydrate saturation and fine particle content conditions in different regions have great differences [*Moridis et al.*, 2011; *J. Yoneda et al.*, 2018]. In this section, the influence of hydrate saturation and fines content on the shear rate dependence of hydrate-bearing sediments under plane strain conditions has been studied.

2.2.1 Experimental conditions

Table 3-4. Experimental conditions.

Test	Sand	Hydrate Saturation (%)	Confining Pressure (MPa)	Pore Pressure (MPa)	Temperature (K)	Shear Rate (%/min)
1*	Toyoura	0	13.0	10.0	278.15	0.05
2*	Toyoura	0	13.0	10.0	278.15	0.5
3*	Toyoura	0	13.0	10.0	278.15	1
4	Toyoura	11.6	13.0	10.0	278.15	0.05
5	Toyoura	16.3	13.0	10.0	278.15	0.5
6	Toyoura	12.4	13.0	10.0	278.15	1
7*	Toyoura	43.6	13.0	10.0	278.15	0.05
8*	Toyoura	42.5	13.0	10.0	278.15	0.5
9*	Toyoura	43.7	13.0	10.0	278.15	1
10	Tb	0	13.0	10.0	278.15	0.05
11	Tb	0	13.0	10.0	278.15	0.5
12	Tb	0	13.0	10.0	278.15	1
13	Tb	43.6	13.0	10.0	278.15	0.05
14	Tb	40.0	13.0	10.0	278.15	0.5
15	Tb	44.3	13.0	10.0	278.15	1

* The experimental results already have been shown in section 2.

Based on the experimental results in section 2, three different strain rates (0.05 %/min, 0.5 %/min, 1 %/min) were selected to study the effect of hydrate saturation and fine particle content on shear

rate-dependent characteristics. The hydrate saturation was about 0%, 15%, 40%, respectively. As for the content of fine particles, only Toyoura (fines content = 0%) and Tb (fines content = 8.9%) were selected for comparison experiments. The specific experimental conditions of the experiments are shown in **Table 3-4**.

The experiments with * in the experiment serial number have been shown in section 2, here as the comparison group. In this section, the size and unit of the Particle Tracking Velocimetry (PTV) analysis are shown in **Figure 3-19**.

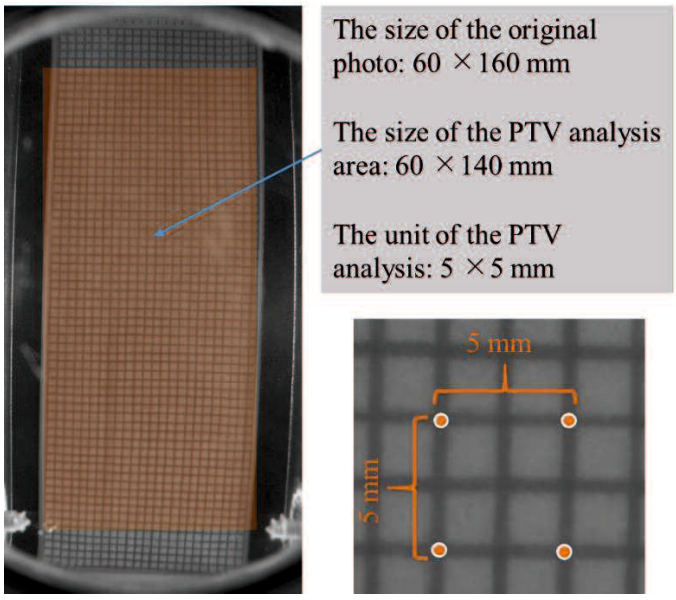

Figure 3-19. The size and unit of the PTV analysis.

2.2.2 Stress-strain relationship

Figure 3-20 shows the stress-strain relationship of the host sand (Toyoura) samples and hydrate-bearing sediments (Toyoura) under different shear rates. As mentioned earlier, the principal strength difference versus axial strain curve of host sand (Toyoura) was not affected by the shear rate, but the volumetric strain compression (positive means compression and negative means expansion) of the host sand (Toyoura) was decreased under a higher shear rate. As for hydrate-

bearing sediments (Toyoura) with a hydrate saturation of about 40%, the principal strength difference of the samples increased with the increase of the shear rate. And with the increase of the shear rate, the volumetric expansion effect of the hydrate-bearing sediments (Toyoura) was significantly increased in the later period of the shear test.

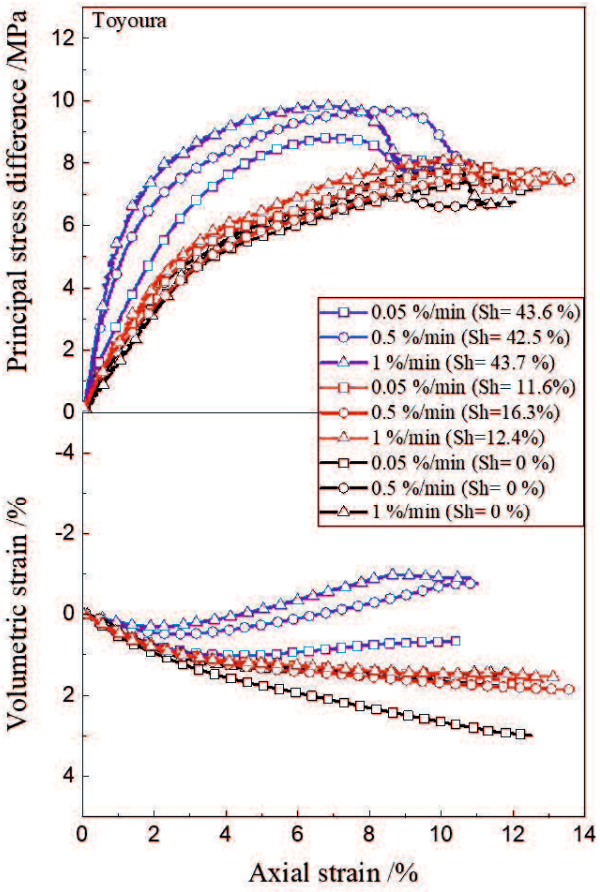

Figure 3-20. Stress-strain relationship of the host sand (Toyoura) samples and hydrate-bearing sediments (Toyoura) under different shear rates.

When the hydrate saturation was about 15%, the shear rate had little effect on the stress-strain relationship of the hydrate-bearing sediments (Toyoura). The stress-strain carves of hydrate-bearing sediments with hydrate saturation about 15% almost the same under different shear rates. Previous studies [*Lijith et al.*, 2019] have found that the morphologies of methane hydrate in the

sediments varied with hydrate saturation. When the hydrate saturation was very low, the hydrate mainly existed on the surface of the particles and the pores between the particles. And at this condition, the strength and stiffness of the hydrate-bearing sediments were not increased significantly due to the presence of hydrate. The cementation effect between the hydrate and the particles and the load-bearing morphology were increased with a higher hydrate saturation. Here it was found that the shear rate dependence of the hydrate-bearing sediments (Toyoura) was more significant under the condition of high hydrate saturation (Sh≈40%). A possible explanation for this phenomenon is that the hydrate-bearing sediments showed significant shear rate dependence result from the cementation between the hydrate and the particles and the loading-bearing morphology in the sample. As the cementation of hydrates on sediment particles or the loading-bearing morphology in the sample can limit the movement and turnover of sediment particles during the shearing process.

Figure 3-21 shows the stress-strain relationship of host sand (Toyoura and Tb) and hydrate-bearing sediments (Toyoura and Tb) under different shear rates. From **Figure 3-21** (left), it can be found that the volumetric compression effect of the host sand (Tb) was more significant than that of the Toyoura sand. The principal stress difference-axial strain curves of both Toyoura and Tb host sand samples were almost not affected by the shear rate, and the volume compression of them was reduced under a higher shear rate. As shown in **Figure 3-21** (right), under the same experimental conditions, the initial stiffness and final volumetric expansion effect of the hydrate-bearing sediments (Tb) were lower than that of the hydrate-bearing sediments (Toyoura). Previous studies [*Kajiyama et al.*, 2017] also reported that at a dense state, the hydrate-bearing sediments with high fines content displayed a smaller initial stiffness. On the other hand, the hydrate-bearing sediments (Tb) also showed shear rate dependence. The initial stiffness and principal stress difference of the hydrate-bearing sediments (Tb) increased with the increase of the shear rate.

Additional, marked volumetric expansion behavior of the hydrate-bearing sediments (Tb) can be observed at a higher shear rate. Finally, regardless of whether the Tb sand contains hydrate or not, its volume expansion strain was lower than that of the Toyoura sand sample under the same conditions.

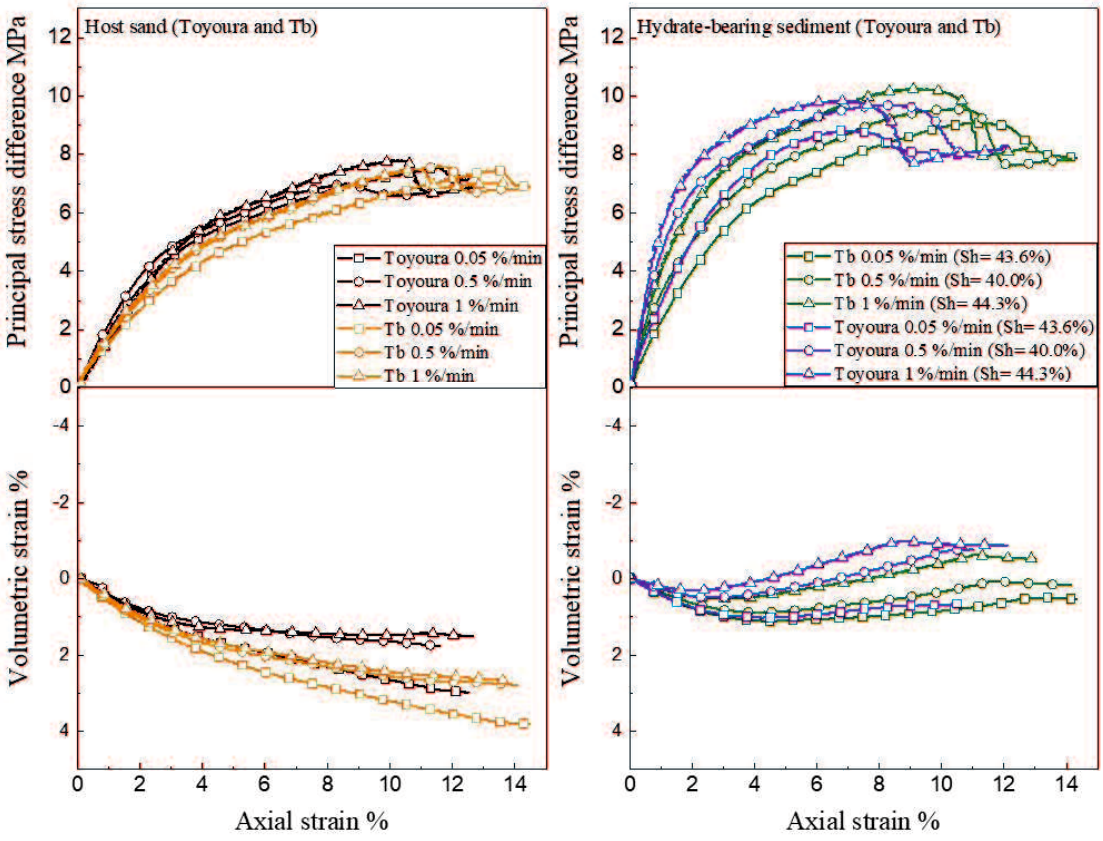

Figure 3-21. Stress-strain relationship of the host sand (Toyoura and Tb) samples and hydrate-bearing sediments (Toyoura and Tb).

2.2.3 Strength and stiffness

Figure 3-22 shows the peak strength $(\sigma_1-\sigma_3)_{max}$ of the host sand (Toyoura and Tb) samples and hydrate-bearing sediments (Toyoura and Tb) at different shear rates. It can be found that the peak strength of Toyoura sand samples increased with the increase of the hydrate saturation, and only

when the hydrate saturation was high (Sh ≈ 40%), the peak strength of the hydrate-bearing sediments (Toyoura) increased significantly at a higher shear rate. As for the Tb samples, the peak strength of the host sand (Tb) was almost the same as that of the host sand (Toyoura), and it also did not show the shear rate dependence. Under a high hydrate saturation, the peak strength of the hydrate-bearing sediments (Tb) showed the same shear rate-dependent behavior as the hydrate-bearing sediments (Toyoura). And the peak strength of the hydrate-bearing sediments (Tb) was slightly higher than that of the hydrate-bearing sediments (Toyoura) with the same hydrate saturation and shear rates.

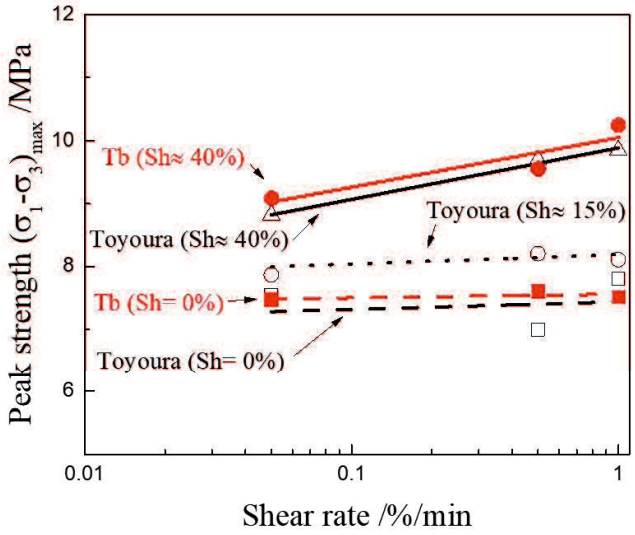

Figure 3-22. Peak strength $(\sigma_1-\sigma_3)_{max}$ of the host sand (Toyoura and Tb) samples and hydrate-bearing sediments (Toyoura and Tb).

Figure 3-23 shows the residual strength of the host sand (Toyoura and Tb) samples and hydrate-bearing sediments (Toyoura and Tb) at different shear rates. With the scope of the experimental conditions in this study, the residual strength of the sample did not show a significant correlation between the shear rate and the content of fine particles. Besides, the residual strength increased with the increase of hydrate saturation.

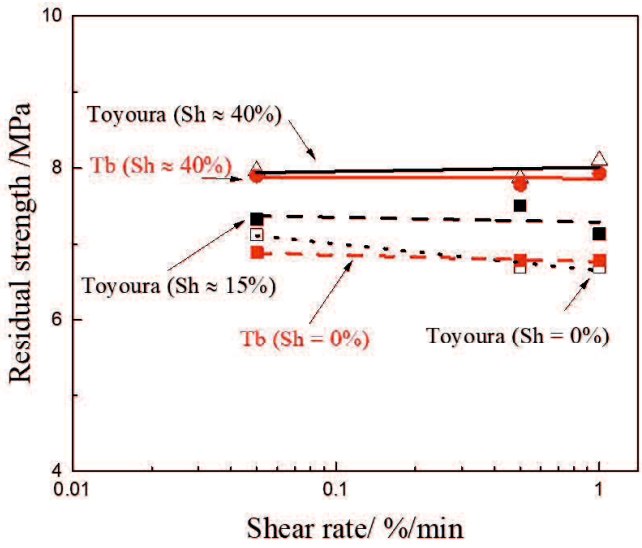

Figure 3-23. Residual strength of the host sand (Toyoura and Tb) samples and hydrate-bearing sediments (Toyoura and Tb).

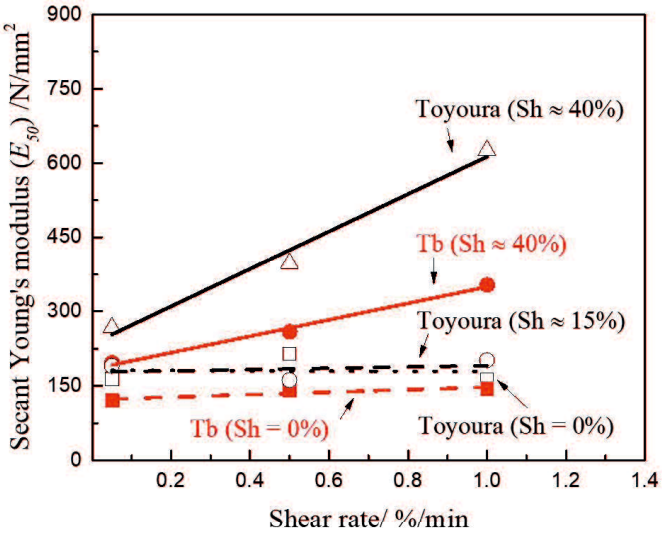

Figure 3-24. Secant Young's modulus (E_{50}) of the host sand (Toyoura and Tb) samples and hydrate-bearing sediments (Toyoura and Tb).

Figure 3-24 shows the Secant Young's modulus (E_{50}) of the host sand (Toyoura and Tb) samples and hydrate-bearing sediments (Toyoura and Tb). As for the Toyoura sand samples, when there was no hydrate (host sand) or the hydrate saturation was very low (Sh≈15%), the E_{50} of the

sample was not affected by the shear rate. And, compared with the host sand sample, the E_{50} of the sample with low hydrate saturation did not increase. When the hydrate-bearing sediments (Toyoura) were at a higher hydrate saturation, the E_{50} of the samples increased with the increase of the shear rate, showing significant shear rate dependence. Under the same hydrate saturation and shear rate conditions, the E_{50} of the samples of Tb in this study was lower than that of the samples of Toyoura. Additionally, the E_{50} of the hydrate-bearing sediments (Tb) also showed shear rate dependence, but the degree was less than that of the hydrate-bearing sediments (Toyoura) with the same hydrate saturation.

2.2.4 Localized deformation

The contours of the maximum shear strain (γ_{max}) results of the host sands (Toyoura) and hydrate-bearing sediments (Toyoura) with hydrate saturation of about 40% have been discussed previously (see **Figures 3-12 and 3-13**). As a comparison, **Figures 3-25** and **3-26** show the maximum shear strain of the hydrate-bearing sediments (Tb) with hydrate saturation of about 40% and the host sands (Tb) under the shear rate of 0.05 %/min and 0.5 %/min, respectively. Firstly, whether it is the pure sand (Tb) or the hydrate-bearing sediment (Tb), under different shear rate conditions, clear shear bands appeared after the axial strain reaches 12%. From **Figure 3-25**, it can be found that for the hydrate-bearing sediment (Tb), under a higher shear rate, the area with high γ_{max} becomes slightly wider (red area). For the host sands (Tb), the shear rate has little effect on the γ_{max} results (see in **Figure 3-26**). The high γ_{max} area (red area) and the appearance time of the shear band were almost the same in different shear rates. **Figure 3-27** shows the appearance position of the clear shear band of hydrate-bearing sediments (Tb) under different shear rates. It can be found that the increase of the shear rate did not delay or advance the appearance of the shear bands in hydrate-bearing sediments (Tb).

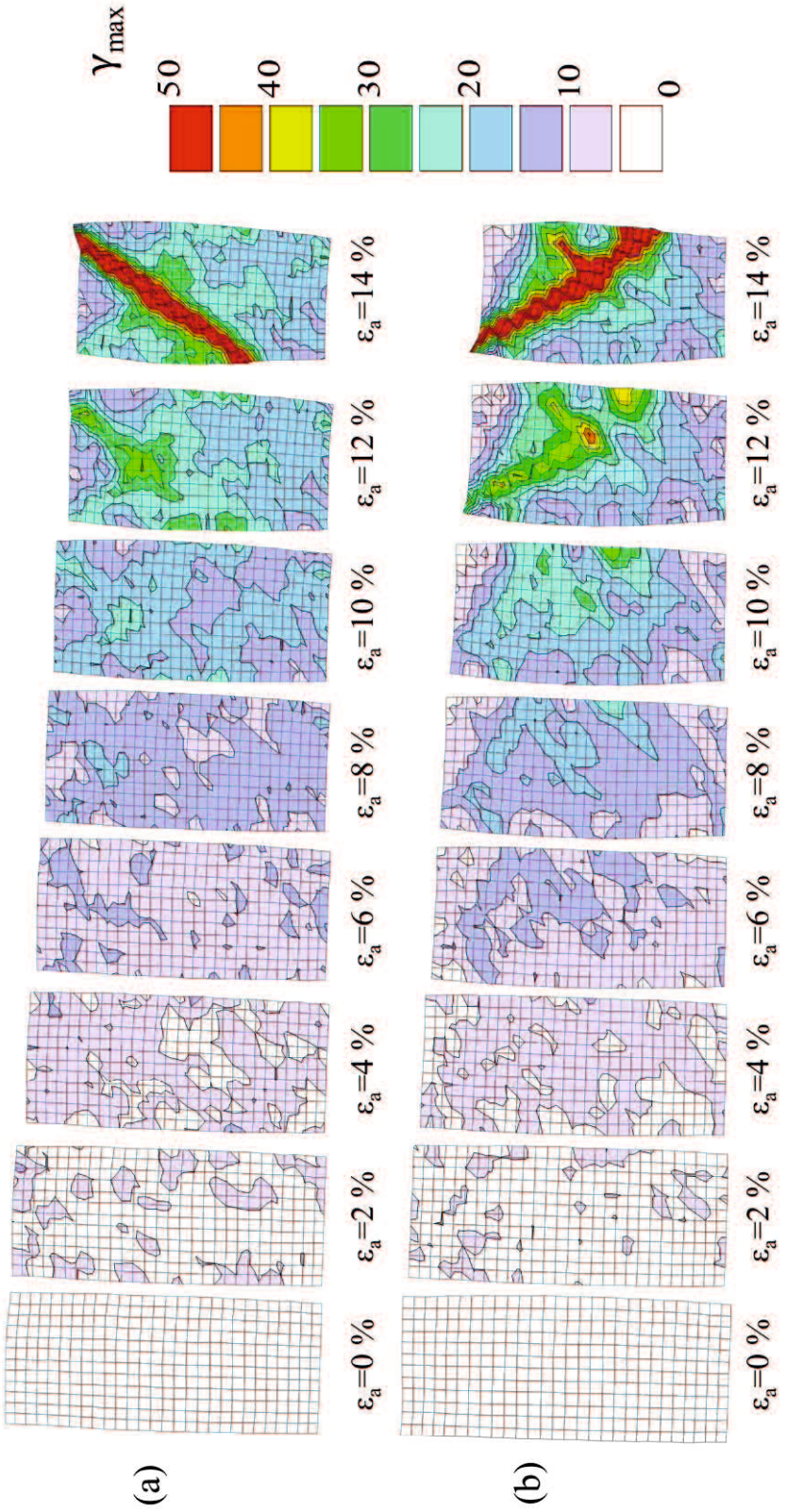

Figure 3-25. Contours of the maximum shear strain of the host sand samples (Tb) with a shear rate of (a) 0.05 %/min and (b) 0.5 %/min.

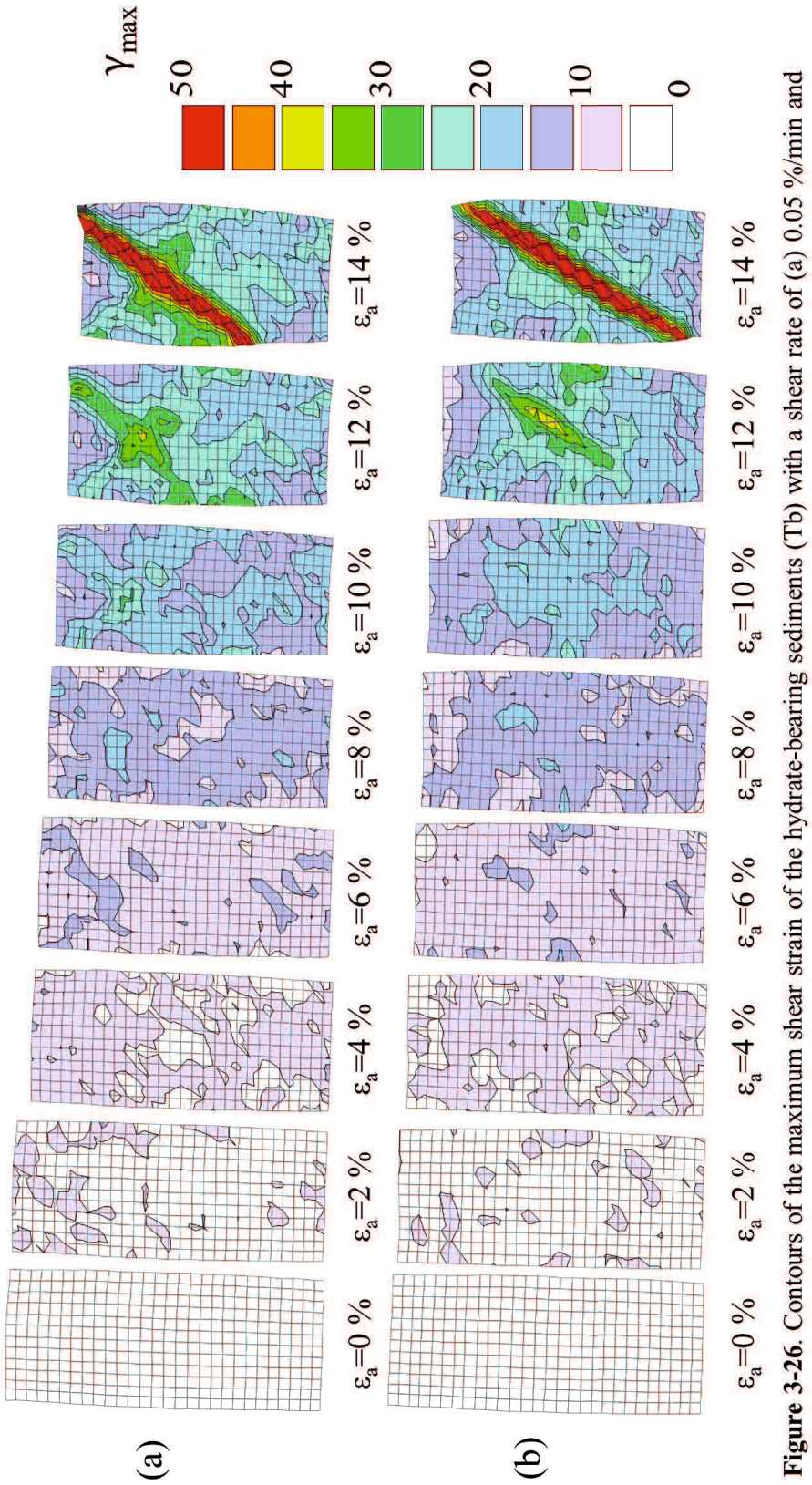

Figure 3-26. Contours of the maximum shear strain of the hydrate-bearing sediments (Tb) with a shear rate of (a) 0.05 %/min and (b) 0.5 %/min.

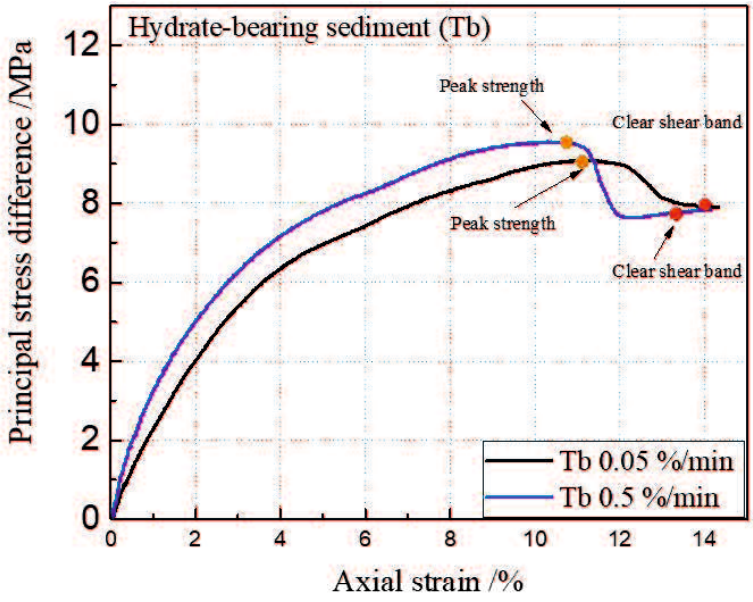

Figure 3-27. The apparent position of the clear shear band of hydrate-bearing sediments (Tb) under different shear rates.

Figures 3-28 and **3-29** show the contours of the final volumetric strain (ε_v, positive means compression, and negative means expansion) of host sand (Toyoura and Tb) and hydrate-bearing sediments (Toyoura and Tb) under different shear rates. To observe the small volumetric strain clearly, here the value of the volumetric strain was controlled within ±20%. As shown in **Figure 3-28**, the shear rate has a greater impact on the local volume expansion effect of the hydrate-bearing sediments (Toyoura). Under high shear rate conditions, the local volumetric expansion area of the hydrate-bearing sediments (Toyoura) was wider, and the volumetric expansion in the shear band was more significant. As for the host sand (Toyoura), the local volumetric expansion only existed in the shear band area and it was almost unaffected by the shear rate.

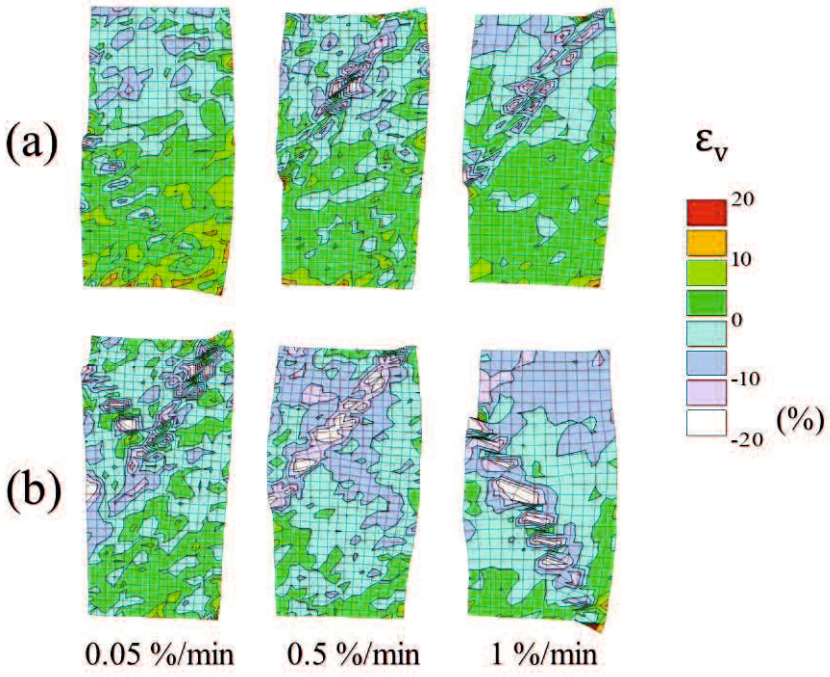

Figure 3-28. Contours of the final volumetric strain of (a) host sand (Toyoura) and (b) hydrate-bearing sediments with hydrate saturation of about 40% (Toyoura).

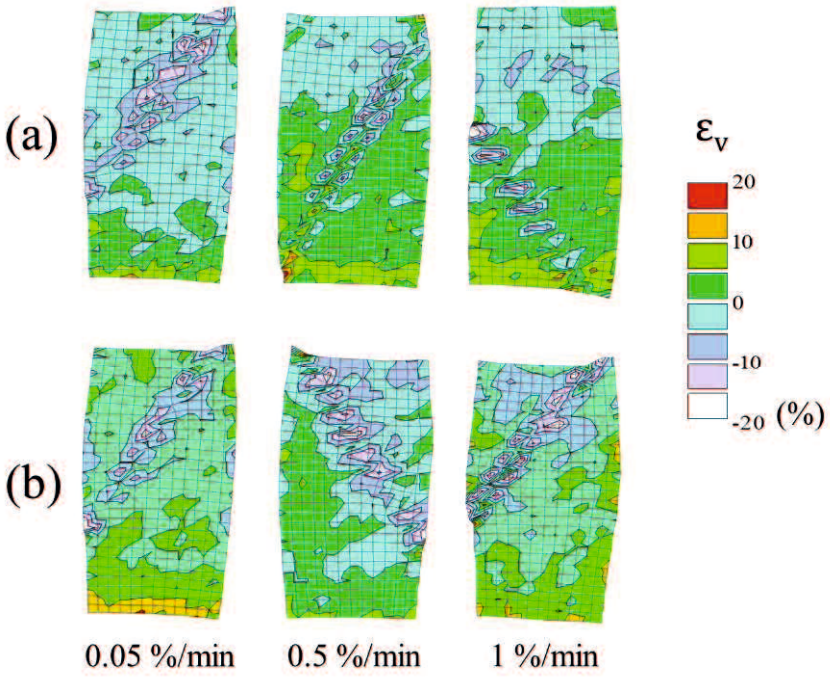

Figure 3-29. Contours of the final volumetric strain of (a) host sand (Tb) and (b) hydrate-bearing sediments with hydrate saturation about 40% (Tb).

Differently, from **Figure 3-29**, it can be found that under a higher shear rate, the local volumetric expansion area of the host sand (Tb) and hydrate-bearing sediments (Tb) with hydrate saturation of about 40% was slightly reduced and increased, respectively. This means that the shear rate has little effect on the local volumetric strain of the samples (Tb) with and without hydrates. Additionally, comparing **Figures 3-28** and **3-29**, the local volumetric strain expansion of the hydrate-bearing sediments (Toyoura) was more significant than that of the hydrate-bearing sediments (Tb) under all shear rate conditions.

To sum up, due to the presence of fine particles, the shear rate dependence characteristics of the host sand (Tb) and hydrate-bearing sediments (Tb) were affected significantly. As for the host sands, the peak strength, residual strength, and E_{50} of the host sand (Tb and Toyoura) were not affected by the shear rate. However, the local strain behaviors of the host sand (Toyoura) vary with changes in shear rate. The local volumetric strain expansion of the host sand (Toyoura) was more significant and the appearance of clear shear bands was also earlier under a higher shear rate. The local deformation of the host sand (Tb) was not affected by the shear rate. As for the hydrate-bearing sediments, under the same hydrate saturation, the peak strength of the hydrate-bearing sediments (Toyoura and Tb) were similar and have the same shear rate-dependent characteristics. But the E_{50} of the hydrate-bearing sediments (Tb) was lower than that of hydrate-bearing sediments (Toyoura), the E_{50} of the hydrate-bearing sediments (Tb) also showed lower shear rate dependence. The local deformation of the hydrate-bearing sediments (Tb) was also not as significantly affected by the shear rate as in the hydrate-bearing sediments (Toyoura).

The presence of fine particles will increase the compactness of the sample and then affect the movement of sediment particles during the shearing process. And the fine particles in the pore space of the sediment can also affect the formation of the hydrates in sediments. Previous studies

[*Lei and Santamarina*, 2019] found that the sediment mechanical and transport responses were controlled by the fine particles, even though most of the mass is sand in the sediment. Besides, the fine particles can also affect the formation of the gas hydrate in the sediments. The generation of the hydrate in the sediment that contained fines was displacive and segregated and it was easier to generate the lenses-like structure [*Lei and Santamarina*, 2018]. Coarse sand samples are prone to generate larger hydrate clusters [*Yoneda et al.*, 2016] due to the larger pore size between sediment particles, which in turn affects the migration mode of particles during the shearing process. In the future, an experimental method that can observe the movement of particles inside the sample needs to be adopted to determine the reason for the influence of fine particles on the shear rate dependence of the hydrate-bearing sediments.

3. Conclusion

Chapter 3 studies the shear rate dependence characteristics of methane hydrate-bearing sediments under plane strain conditions. The host Toyoura sand and methane hydrate-bearing sediments (Toyoura) with hydrate saturation of about 40% were first used to confirm the shear rate dependence behaviors of different kinds of samples under plane strain conditions. And then the effection of fine particle content and hydrate saturation on shear rate dependence has been studied. Based on the experimental results, the following conclusions can be get:

(1) Compared with the host sand (Toyoura and Tb), the stress-strain relationship of the hydrate-bearing sediments (Toyoura and Tb) is more significantly affected by the shear rate.

(2) The peak strength of the host sands (Toyoura and Tb) was not affected by the shear rate. On the contrary, the peak strength of hydrate-bearing sediments (Toyoura and Tb) increased with the increase of shear rate. This means that under plane strain conditions the peak strength of the methane hydrate-bearing sediments (Toyoura and Tb) have shear rate-dependent properties.

(3) The presence of methane hydrate increased the residual strength of the hydrate-bearing sediments, but the shear rate did not affect the residual strength of the hydrate-bearing sediments.

(4) The secant Young's modulus (E_{50}) of hydrate-bearing sediments (Toyoura and Tb) increased with the increase of the shear rate, and no obvious difference in the E_{50} was observed at different shear rates for the host sand (Toyoura and Tb). Besides, under the same hydrate saturation and shear rate conditions, the E_{50} of the samples of Tb was lower than that of the samples of Toyoura.

(5) As for the hydrate-bearing sediments (Toyoura) with hydrate saturation of about 40%, the angle of the shear bands was not affected by the shear rate. And for the shear rate range used in this study, the shear band angles of the hydrate-bearing sediment samples were larger than that of

the host sand samples.

(6) The shear rate dependence characteristics of the hydrate-bearing sediments were more significant with a higher hydrate saturation.

(7) The local deformation of the hydrate-bearing sediments (Tb) was also not as significantly affected by the shear rate as in the hydrate-bearing sediments (Toyoura). As for the hydrate-bearing sediments (Toyoura), the increase in shear rate can significantly improve the local volume expansion behavior of the samples and the large shear strain contour became more concentrated inside the shear band under a higher shear rate.

4. Reference

Alshibli, K. A., and S. Sture (1999), Sand shear band thickness measurements by digital imaging techniques, *Journal of computing in civil engineering*, *13*(2), 103-109.

Alshibli, K. A., and S. Sture (2000), Shear band formation in plane strain experiments of sand, *Journal of Geotechnical and Geoenvironmental Engineering*, *126*(6), 495-503, doi:10.1061/(ASCE)1090-0241(2000)126:6(495).

Arthur, J., T. Dunstan, Q. Al-Ani, and A. Assadi (1977), Plastic deformation and failure in granular media, *Geotechnique*, *27*(1), 53-74.

Chaouachi, M., Falenty, A., Sell, K., Enzmann, F., Kersten, M., Haberthür, D., and Kuhs, W. F. (2015). "Microstructural evolution of gas hydrates in sedimentary matrices observed with synchrotron X-ray computed tomographic microscopy." *Geochem. Geophys. Geosyst.*, 16(6), 1711-1722

Desrues, J., Viggiani, G., 2004. Strain localization in sand: an overview of the experimental results obtained in Grenoble using stereophotogrammetry. Int. J. Numer. Anal. Methods Geomech. 28, 279–321.

Dillon, H. B., and Andersland, O. (1967). "Deformation rates of polycrystalline ice." *Physics of Snow and Ice*: proceedings, 1(1), 313-328

Durham, W. B., Kirby, S. H., Stern, L. A., and Zhang, W. (2003). "The strength and rheology of methane clathrate hydrate." J. Geophys. Res. *Solid Earth*, 108(4), ECV 2-1 - 2-11

Duncan, J. M., and C.-Y. Chang (1970), Nonlinear analysis of stress and strain in soils, *Journal of Soil Mechanics & Foundations Div*.

Hawkes, I., and Mellor, M. (1972). "Deformation and fracture of ice under uniaxial stress."

Journal of Glaciology, 11(61), 103-131

Hyodo, M., Y. Li, J. Yoneda, Y. Nakata, N. Yoshimoto, A. Nishimura, and Y. Song (2013), Mechanical behavior of gas-saturated methane hydrate-bearing sediments, *J. Geophys. Res. Solid Earth*, *118*(10), 5185-5194, doi: 10.1029/2006JB004484.

Iwai, H., Y. Konishi, K. Saimyou, S. Kimoto, and F. Oka (2018), Rate effect on the stress-strain relations of synthetic carbon dioxide hydrate-bearing sand and dissociation tests by thermal stimulation, *Soils Found.*, *58*(5), 1113-1132, doi:10.1016/j.sandf.2018.05.007.

Jones, S. J. (1997). "High strain-rate compression tests on ice." *The Journal of Physical Chemistry* B, 101(32), 6099-6101

Kajiyama, S., M. Hyodo, Y. Nakata, N. Yoshimoto, Y. Wu, and A. Kato (2017), Shear behaviour of methane hydrate bearing sand with various particle characteristics and fines, *Soils Found.*, *57*(2), 176-193, doi:10.1016/j.sandf.2017.03.002.

Kato, A., and Y. Nakata (2015), Plane strain compression behaviour and localization of deformation of MH-bearing sand, paper presented at 15th Asian Regional Conference on Soil Mechanics and Geotechnical Engineering, ARC 2015, Asian Regional Conference on Soil Mechanics and Geotechnical Engineering.

Kato, A., Nakata, Y., Hyodo, M., and Yoshimoto, N. (2016). "Macro and micro behaviour of methane hydrate-bearing sand subjected to plane strain compression." *Soils Foundations*., 56(5), 835-847.doi:10.1016/j.sandf.2016.08.008

Klar, A., K. Soga, and M. Ng (2010), Coupled deformation–flow analysis for methane hydrate extraction, *Geotechnique*, *60*(10), 765-776.

Lade, PV., Trads, N., 2014. The role of cementation in the behaviour of cemented soils. Geotech. Res. 14, 00011.

Lei, L., and J. Santamarina (2018), Laboratory strategies for hydrate formation in fine-grained

sediments, *J. Geophys. Res. Solid Earth*, *123*(4), 2583-2596.

Lei, L., and J. C. Santamarina (2019), Physical properties of fine-grained sediments with segregated hydrate lenses, *Mar. Pet. Geol.*, *109*, 899-911.

Lijith, K., B. R. Malagar, and D. N. Singh (2019), A comprehensive review on the geomechanical properties of gas hydrate bearing sediments, *Mar. Pet. Geol.*

Lin, J. S., Y. Seol, and J. H. Choi (2015), An SMP critical state model for methane hydrate-bearing sands, *International Journal for Numerical and Analytical Methods in Geomechanics*, *39*(9), 969-987.

Miyazaki, K., A. Masui, H. Haneda, Y. Ogata, K. Aoki, and T. Yamaguchi (2008), Variable-compliance-type constitutive model for methane hydrate bearing sediment, paper presented at Proceedings of the 6th international conference on gas hydrates.

Miyazaki, K., N. Tenma, K. Aoki, and T. Yamaguchi (2012), A nonlinear elastic model for triaxial compressive properties of artificial methane-hydrate-bearing sediment samples, *Energies*, *5*(10), 4057-4075.

Miyazaki, K., N. Tenma, and T. Yamaguchi (2017), Relationship between creep property and loading-rate dependence of strength of artificial methane-hydrate-bearing toyoura sand under triaxial compression, *Energies*, *10*(10), doi:10.3390/en10101466.

Miyazaki, K., T. Yamaguchi, Y. Sakamoto, and K. Aoki (2011), Time-dependent behaviors of methane-hydrate bearing sediments in triaxial compression test, *International Journal of the JCRM*, *7*(1), 43-48.

Moridis, G. J., et al. (2011), Challenges, uncertainties, and issues facing gas production from gas-hydrate deposits, *SPE Reservoir Evaluation and Engineering*, *14*(1), 76-112, doi:10.2118/131792-PA.

Parameswaran, V. (1980). "Deformation behaviour and strength of frozen sand." *Can. Geotech.*

J., 17(1), 74-88

Roscoe, K. H. (1970). "The influence of strains in soil mechanics." *Geotechnique*, 20(2), 129-170

Schofield, A., and P. Wroth (1968), *Critical state soil mechanics*, McGraw-hill.

Soga, K., S. Lee, M. Ng, and A. Klar (2006), Characterisation and engineering properties of methane hydrate soils, *Characterisation and engineering properties of natural soils*, *4*, 2591-1642.

Stafford, J., and Tanner, D. (1983). "Effect of rate on soil shear strength and soil-metal friction I. Shear strength." *Soil and tillage research*, 3(3), 245-260

Vaid, Y. P., P. Byrne, and J. Hughes (1981), Dilation angle and liquefaction potential.

Waite, W. F., J. C. Santamarina, D. D. Cortes, B. Dugan, D. N. Espinoza, J. Germaine, J. Jang, J. Jung, T. J. Kneafsey, and H. Shin (2009), Physical properties of hydrate-bearing sediments, *Reviews of geophysics*, *47*(4).

Wu, Q., Yoshimoto, N., Nakano, N., Kajiyama, S., Xu, J., and Nakata, Y. "Shear Rate-Dependent Behaviors on Natural Gas Hydrate-Bearing Sediments Under Plane Strain Shear Test." Proc., The 30th International Ocean and Polar Engineering Conference, *International Society of Offshore and Polar Engineers*.

Yoneda, J., M. Hyodo, Y. Nakata, and N. Yoshimoto (2008), Time-dependent elasto-plastic constitutive equation for sedimentary sands supported by methane hydrate, paper presented at the 12th Japan Symposium on Rock Mechanics and the 29th Western Japan Symposium on Rock Engineering, *Jpn. Comm. for Rock Mech., Ube, Japan*, 2-4.

Yoneda, J., M. Hyodo, N. Yoshimoto, Y. Nakata, and A. Kato (2013), Development of high-pressure low-temperature plane strain testing apparatus for methane hydrate-bearing sand, *Soils Found.*, *53*(5), 774-783.

Yoneda, J., Y. Jin, J. Katagiri, and N. Tenma (2016), Strengthening mechanism of cemented

hydrate-bearing sand at microscales, *Geophysical Research Letters*, *43*(14), 7442-7450.

Yoneda, J., A. Masui, Y. Konno, Y. Jin, M. Kida, J. Katagiri, J. Nagao, and N. Tenma (2017), Pressure-core-based reservoir characterization for geomechanics: Insights from gas hydrate drilling during 2012–2013 at the eastern Nankai Trough, *Mar. Pet. Geol.*, *86*, 1-16, doi:10.1016/j.marpetgeo.2017.05.024.

Yoneda, J., M. Oshima, M. Kida, A. Kato, Y. Konno, Y. Jin, J. Jang, W. F. Waite, P. Kumar, and N. Tenma (2018), Pressure core based onshore laboratory analysis on mechanical properties of hydrate-bearing sediments recovered during India's National Gas Hydrate Program Expedition (NGHP) 02, *Mar. Pet. Geol.*, doi:10.1016/j.marpetgeo.2018.09.005.

Chapter 4. Decomposition of hydrate in sands

1. Introduction

Previous studies have shown that depressurization is an economically feasible method of natural gas hydrate (NGH) exploitation [*Kurihara, M et al*., 2009; *Moridis, G. J et al*., 2009]. However, the production efficiency of depressurization is limited by the permeability of the reservoir and the regeneration of hydrates. Especially for areas with high fine particle content, the gas production efficiency in the later stage of depressurization decreases sharply [*Moridis, G. J et al*., 2011; *Walsh, M. R et al*., 2009]. Although the application of horizontal production wells has greatly increased the efficiency of depressurization, the gas production rate still cannot meet commercial exploitation needs [*Jianliang, Y et al*., 2020; *Yu, T* et al., 2019; *Feng, Y et al.*, 2019]. Moreover, horizontal wells are more affected by the mechanical behavior of reservoir sediments, and it is impossible to increase gas production efficiency by further increasing the magnitude of depressurization [*Jin, G et al*., 2018;].

Thermal stimulation is necessary as an auxiliary exploitation method to improve the gas production efficiency of NGH [*Falser, S et al*., 2012; *Liu, Y et al*., 2018;]. Considering the different fine particle content of the reservoir, this chapter first studied the influence of fine particle content on the hydrate decomposition characteristics in hydrate-bearing sediments under local thermal stimulation conditions. On the other hand, sediments located at different locations in the reservoir are in different stress states due to the early construction of the wellbore.

Thermal stimulation and depressurization operations will cause the decomposition of hydrates, which will affect the stress-strain behavior of sediments, and the deformation of sediments will also affect the decomposition characteristics of hydrates at the same time. Understanding the mechanic behavior of hydrate-bearing sediments and the decomposition characteristics of hydrates under different stress states is also very important to accurately predict the mechanical behavior of the NGH reservoir during the exploitation process. In the second part of this chapter, under different stress conditions, the stress-strain relationship of hydrate-bearing sediments and the decomposition characteristics of hydrates during local thermal stimulation and depressurization have been studied.

2. Decomposition of hydrates in sands

2.1 Local thermal stimulation

2.1.1 The experimental instrument

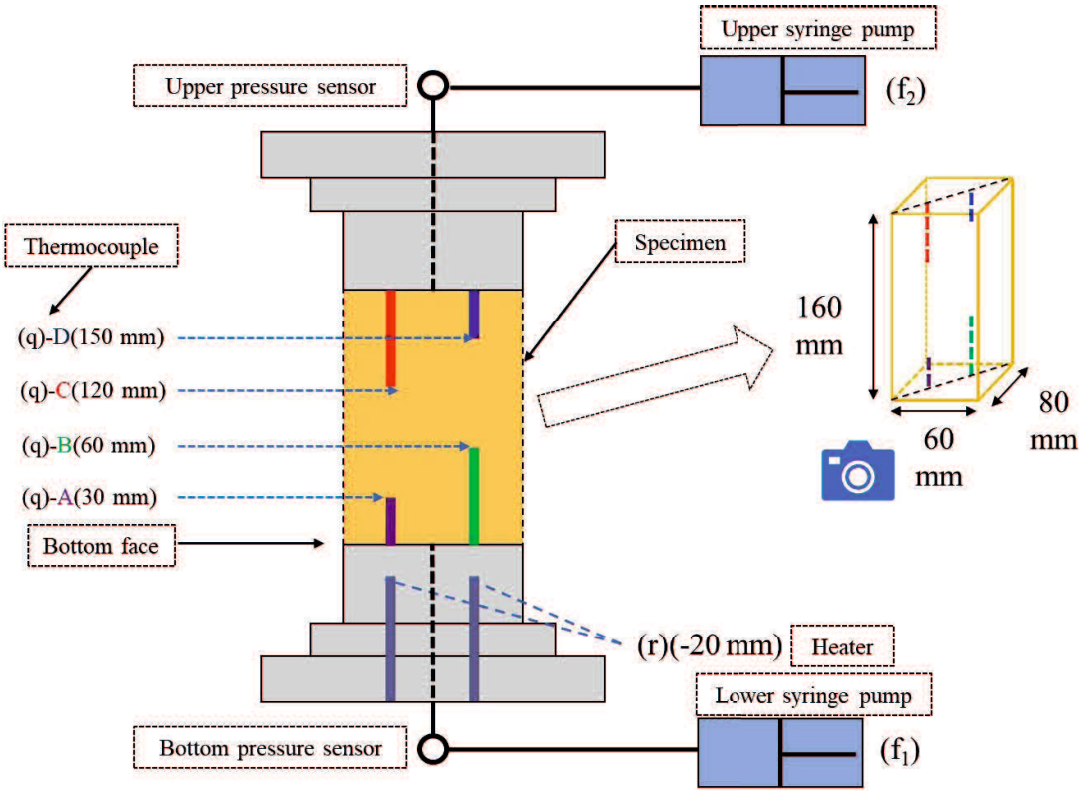

Figure 4-1. The schematic diagram of the sample part.

Figure 4-1 shows the schematic diagram of the sample part in this chapter. Four thermocouples located on the diagonal inside the sample and distance the bottom surface of the sample are 30, 60, 120, and 150 mm respectively. The heating device is 20 mm away from the bottom surface of the sample. There are two pressure sensors on the top and bottom of the sample to measure the pore pressure of the sample during the experiment. A detailed introduction of the instrument can be found in Chapter 2.

2.1.2 Experimental procedure and conditions

Toyoura, Tb, and Tc were adopted as the host sediment. The percentage of fines contained (Fc) in Toyoura, Tb and Tc were 0%, 8.9%, and 22.9%, respectively.

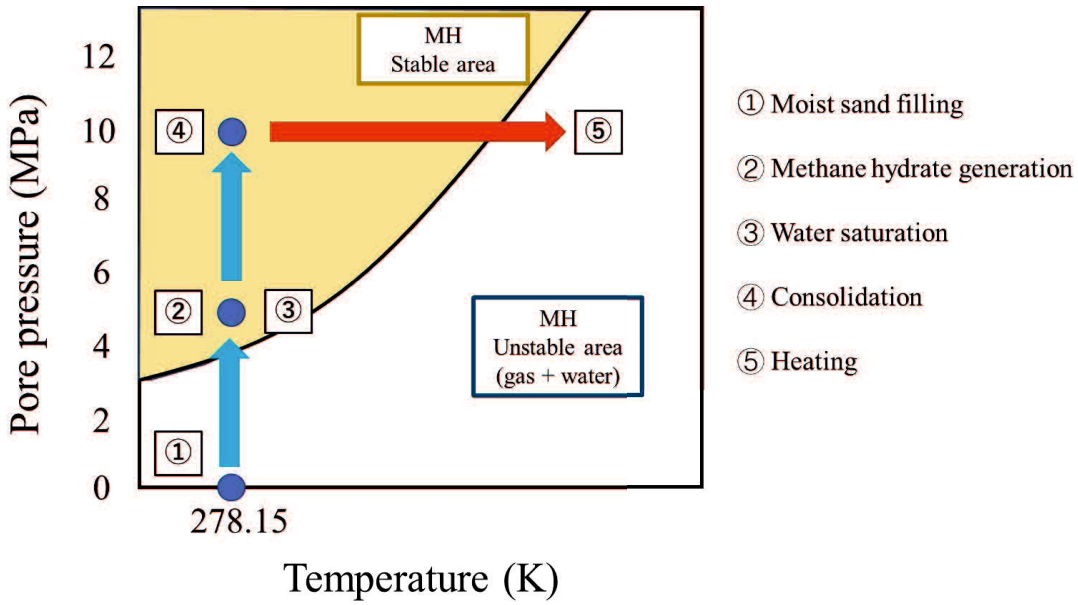

Figure 4-2. The schematic diagram of the experimental process.

The experimental procedure as follows:

(1) Methane hydrate-bearing sediment preparation

A certain amount of water and dry host sand was mixed to obtain predetermined hydrate saturation. After the membrane with a grid attached was installed to the mold, the moist sand was divided into 12 layers and filled into the mold. Filter papers were applied to the upper and bottom surfaces of the sample. Two acrylic confining plates were fixed on the opposite side of the sample to maintain plane strain conditions. A vacuum pump was used to remove free air from the inside of the sample and then water was filled within the confining chamber after the cell was fixed. Syringe pumps were adopted to inject water and gas into the apparatus and to measure the changes in specimen volume simultaneously. Methane gas could be injected into the sample from both the top and the bottom with the two syringe pumps. During the methane gas injection, the pore

pressure and the cell pressure were increased to 5.0 MPa and 5.2 MPa gradually. The confining pressure was kept 0.2 MPa higher than the pore pressure at all times at this step. The methane hydrate-bearing sediment was formed at 278.15 K and under 5.0 MPa (pore pressure) for 3 days.

(2) Water saturation and consolidation

Water would be injected from the bottom of the sample to replace the excess methane gas in the sample after the generation of methane hydrate, making the sample saturated with water. After that, the pore pressure and confining pressure were increased to 10 MPa and 13 MPa respectively for consolidation.

(3) Thermal stimulation

Thermal stimulation was performed after the consolidation. As shown in **Figure 4-1**, the lower syringe pump (f_1) was closed during this period. The upper syringe pump (f_2) was used to keep the pore pressure within 10.0 MPa. Decomposed gas and water were collected and recorded at the same time. The thermal stimulation condition was provided by the heater (r), which was kept at 353.15 K during this process. And the laboratory environment temperature was kept at 278.15 K at all times. The temperature at the top position of the sample was considered to be consistent with the ambient temperature and maintained at 283.15 K. The principal stress difference was maintained at 0 MPa during the thermal stimulation test. The entire thermal stimulation process lasted about 15 h. At the end of the heating experiment, the hydrate was heated to complete dissociation and the total amount of the methane gas collected was recorded. The schematic diagram of the experimental process is shown in **Figure 4.2**. **Table 4-1** listed the experimental parameters and conditions in this section.

Table 4-1. Experimental parameters and conditions.

Test name	Sand	Porosity (%)	Hydrate saturation (%)	Confining pressure (MPa)	Pore pressure (MPa)	Initial temperature (K)	Heating temperature (K)
S1	Toyoura	39.2	31.9	13.0	10.0	283.15	353.15
S2	Toyoura	39.9	0	13.0	10.0	283.15	353.15
Tb1	Tb	40.2	36.7	13.0	10.0	283.15	353.15
Tb2	Tb	40.5	0	13.0	10.0	283.15	353.15
Tc1	Tc	39.7	37.7	13.0	10.0	283.15	353.15
Tc2	Tc	40.2	0	13.0	10.0	283.15	353.15

2.1.3 Thermal stimulation results in sands

- Temperature variation of the host sand samples

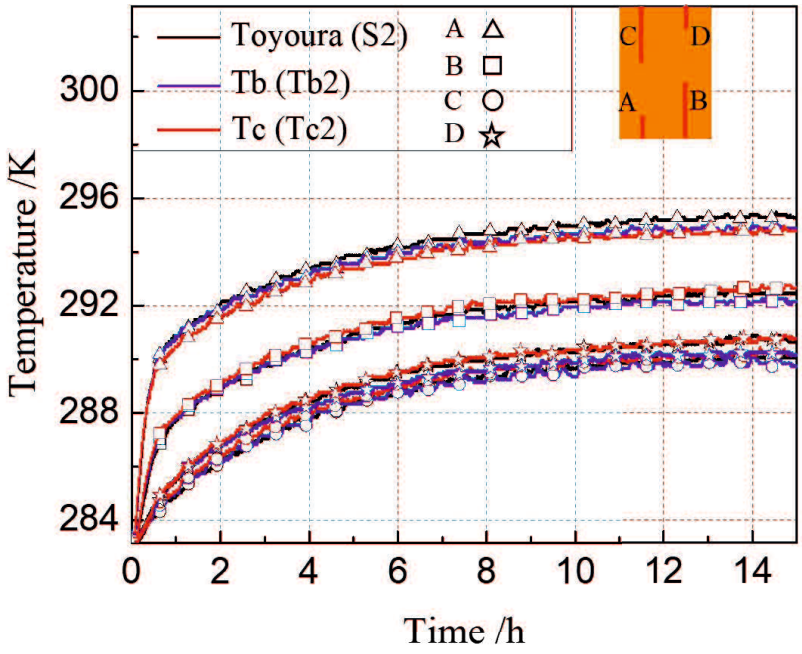

Figure 4-3. Temperature variation with time for different host sand samples.

As for the thermal stimulation experiment of host sand samples under the water saturation conditions, the process of the temperature transfer inside the sample is simpler than that of hydrate-bearing sediments. **Figure 4-3** shows the temperature variation with time for different host sand samples. It can be found that the temperature in the region (A and B) that is close to the

heating surface increased significantly in the earlier time. Notably, the variation in temperature of the different samples appeared to be consistent and there is no obvious difference observed. This implies that the heat transfer characteristics of the different sediments used in this experiment were similar under the water saturation conditions, despite having different particle size distributions and mineral compositions.

- Thermal stimulation results of hydrate-bearing sediments

For thermal stimulation experiments, the decomposition methane gas was gathered by the upper syringe pump (f_2 in **Figure 4-1**). As the hydrate saturation of the hydrate-bearing sediments was similar, here the gas recovery factor was used to compare the decomposition efficiency of the methane hydrate in the different sands. The gas recovery factor at time *t* was calculated according to Formula (4-1):

$$GPF = \frac{V_t}{V_{tc}} \times 100\% \tag{4-1}$$

where GPF is the gas recovery factor, V_t and V_{tc} are the volumes of decomposition gas accumulated at time *t* and total cumulative volume, respectively.

Figure 4-4 shows the varied history of the temperature, pore pressure, and *GPF* of hydrate-bearing sediment (Toyoura) during the thermal stimulation process. The decomposition process of hydrate-bearing sediment (Toyoura) can be divided into four different stages according to the variation of pore pressure, temperature, and GPF.

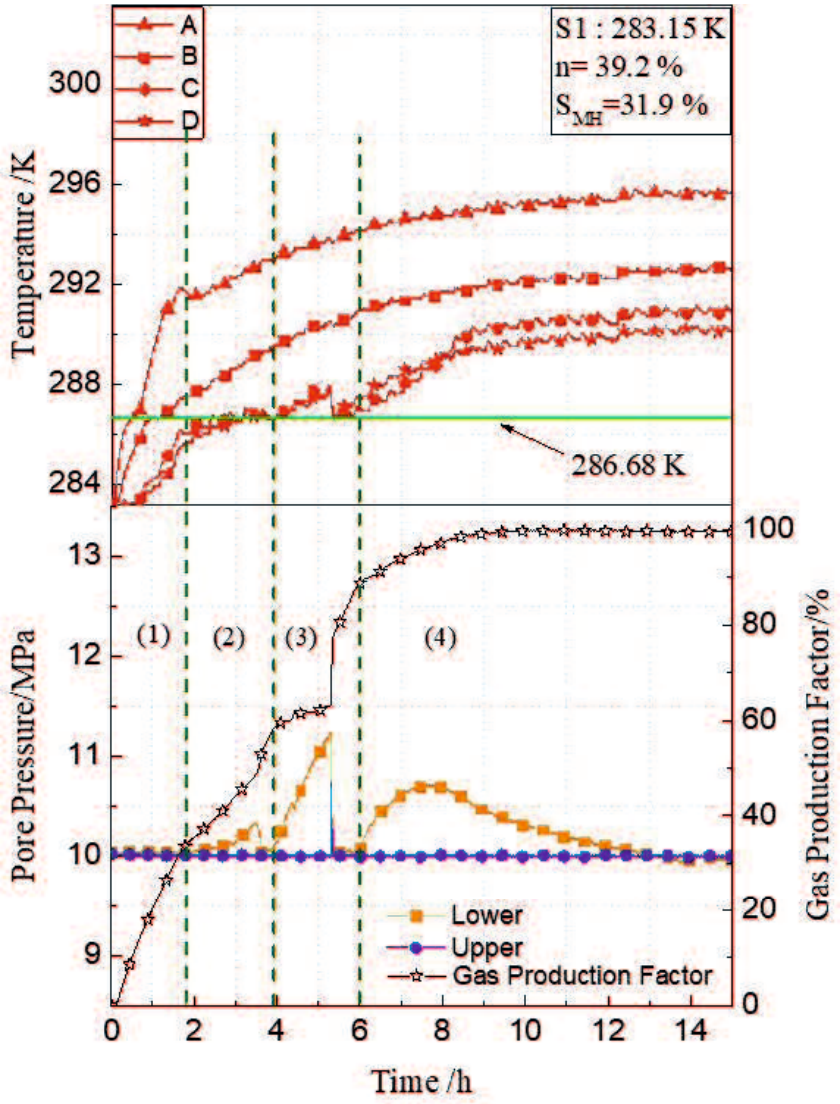

Figure 4-4. The variation history of the temperature, pore pressure, and *GPF* of hydrate-bearing sediment (Toyoura) during the thermal stimulation process.

In stage (1), it was observed that as the temperature gradually increased, the lower and upper pore pressure remained constant, and the *GPF* was approximately linear over time. At this stage, only a small amount of hydrate close to the heating surface was decomposed.

In stage (2), while the upper pore pressure of the sample was kept constant, the measured pore pressure in the lower part first gradually increased, and then quickly decreased to a level equal to the upper pore pressure. The temperature at C and D, which was relatively far away from the

heating surface, was kept constant around 286.68 K (phase equilibrium temperature of methane hydrate at 10 MPa). This may be caused by the balance between the heat transfer effect and the endothermic effect generated by the dissociation of the hydrate. The *GPF* first increased slowly, and then rose rapidly when the lower pore pressure decreased. This indicated that the gas/water movement path inside the sample was not completely blocked. The slight increase of the pore pressure in the lower part was probably caused by the large amount of decomposition gas accumulating inside the sample due to the hindered migration of the gas/water. When the part that blocks the gas/water passage is penetrated due to the increase in pressure difference and the decomposition of hydrate, the lower pore pressure decreased and the *GPF* increased rapidly.

The change in pore pressure at stage (3) is like stage (2). However, the temperature at C and D increased slightly at first, and then decreased to about 286.13 K. Further, the *GPF* first remained unchanged, and then rapidly increased with a decrease of the lower pore pressure. The migration of the decomposition gas was hindered, which led to the increase in the local pore pressure of the sample and the decrease in gas production. The temperature variation implies that the gas generated by the previous hydrate decomposition was likely to reform the hydrate on the upper part of the sample, and blocked the gas/water migration channel again. Finally, in the same way, when the area that blocked the gas/water passage was penetrated due to the increase in pressure difference and the decomposition of the hydrate, the lower pore pressure decreased and the *GPF* increased rapidly.

At the last stage, the measured pore pressure at the lower part first increased slowly and then gradually decreased. The temperature changes at A and B were almost kept consent, and the temperatures at C and D gradually increased and then kept consent. The gas production factor rose slowly. During this stage, the hydrate might undergo the process of slow decomposition at

the top position of the sample. Due to the lower temperature, the hydrate decomposes slowly, and the regeneration of the hydrate also makes the decomposition gas transport difficult, raising the local pore pressure. Unlike stages (2) and (3), in the final stage of hydrate decomposition, the decrease of lower pore pressure was a slow process.

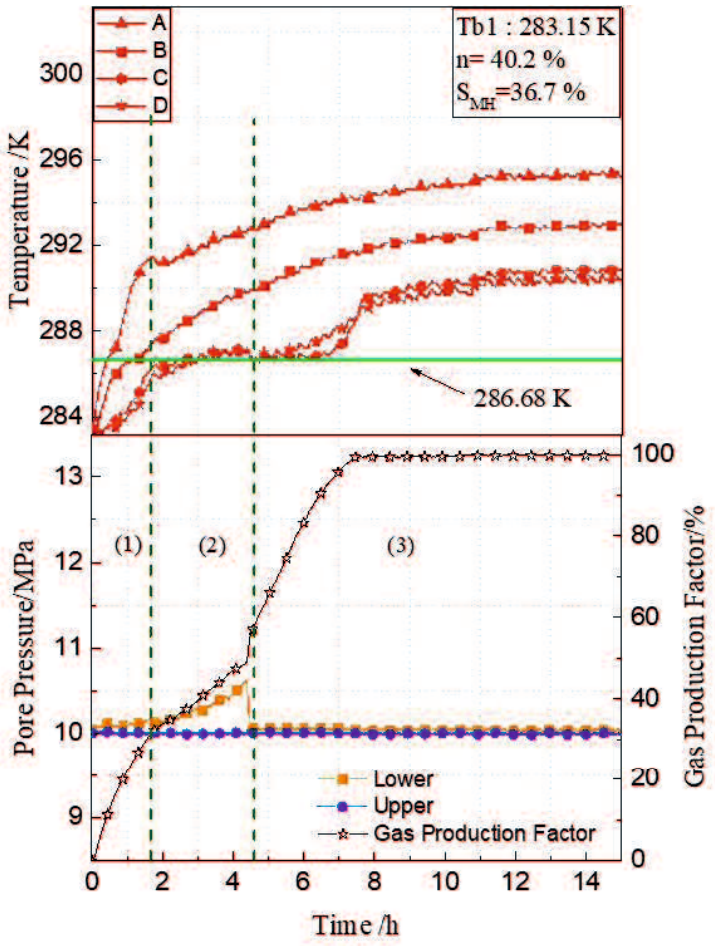

Figure 4-5. The variation history of the temperature, pore pressure, and *GPF* of hydrate-bearing sediment (Tb) during the thermal stimulation process.

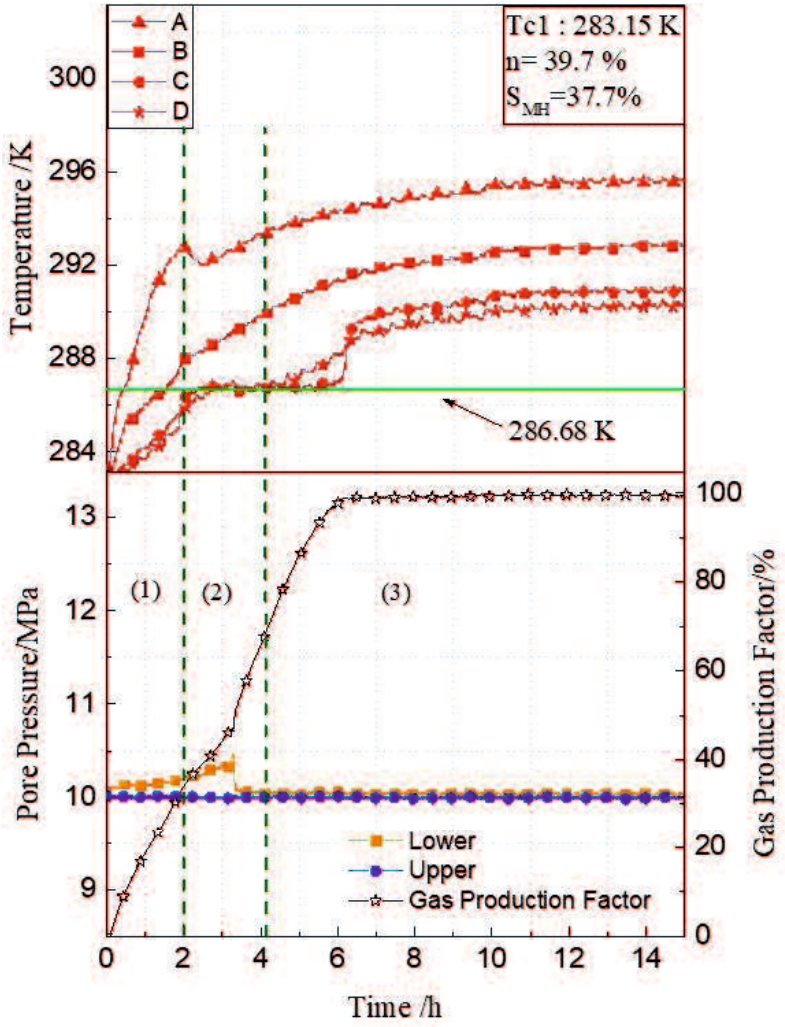

Figure 4-6. The variation history of the temperature, pore pressure, and *GPF* of hydrate-bearing sediment (Tc) during the thermal stimulation process.

Figures 4-5 and **4-6** show the varied history of the temperature, pore pressure, and *GPF* of hydrate-bearing sediment (Tb and Tc) during the thermal stimulation process, respectively. Compared with hydrate-bearing sediment (Toyoura), the variation of the pore pressure of hydrate-bearing sediments (Tb and Tc) was less complicated. The lower pore pressure of hydrate-bearing sediments (Tb and Tc) gradually increased and then decreased to 10 MPa during the thermal stimulation experiment. The experiment results of GPF in hydrate-bearing sediments (Tb and Tc) imply that the gas/water path had not been completely blocked throughout the heating process.

The decomposition process of hydrates in Tb and Tc can be described similarly to the situations of stages 1, 2, and 4 in hydrate-bearing sediment (Toyoura).

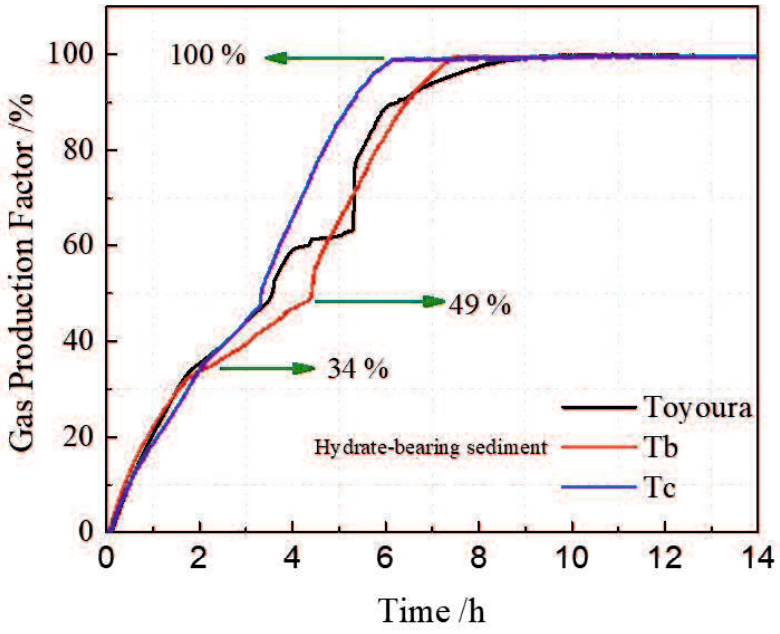

Figure 4-7. The change of gas production factor to time for hydrate-bearing sediments (Toyoura, Tb, and Tc).

The *GPF* changes of the three different hydrate-bearing sediments (Toyoura, Tb, and Tc) are shown in **Figure 4-7**. It can be observed that before the *GPF* reached 34%, the GPF of the three different samples increased similarly over time and then reduced by varying degrees when the GPF was between 34% and 49%. Following that, the *GPF* of hydrate-bearing sediments (Tb and Tc) had the same behavior over time, while MHBS (Toyoura) was more complicated. The total gas production efficiency ratio was calculated according to Formula (4-2):

$$R_{total} = \frac{V_{total}}{t_{total}} \tag{4-2}$$

where R_{total} is the total gas production efficiency ratio, V_{total} is the total volume of decomposition gas, and t_{total} is the time required for the complete decomposition of hydrates. The resultant values

of R_{total} for MHBS (Toyoura) / MHBS (Tb) / MHBS (Tc) were 0.89/1.07/1.30 (10^{-4} m^3/h) , respectively.

As can be seen from the above results, the process of hydrate decomposition of hydrate-bearing sediment (Toyoura) is more complex compared to hydrate-bearing sediments (Tb and Tc). A comprehensive analysis of the characteristics of gas production and pore pressure variation, a possible explanation can be proposed. Compared with the hydrate-bearing sediments (Tb and Tc), the hydrate-bearing sediment (Toyoura) has a larger pore size between the sand particles. Such, there is a greater chance of forming a larger hydrate mass in the pores of Toyoura sand. In the initial stage of heating, the hydrate close to the heating surface was preferentially decomposed. Due to the high temperature of the heating surface, the heat required for hydrate decomposition can be immediately supplemented. Therefore, the initial hydrate decomposition rates were almost the same in the three different samples. The hydrates far away from the heating surface were affected by heat transfer and the self-protection effect of the hydrates [*Belosludov et al.*, 2007], making it difficult to decompose. These problems were more significant for the large hydrate mass in the Toyoura sand. Besides, the regeneration of hydrates may also occur, resulting in the discontinuity of gas production. As for hydrate-bearing sediments (Tb and Tc), the hydrated mass in the pores of these samples was smaller and dispersed. These hydrate masses were easier to decompose. Although hydrate-bearing sediments (Tb and Tc) also encountered blockage of the gas transmission channel caused by hydrate regeneration, the overall continuity of the gas production process was better than hydrate-bearing sediment (Toyoura). This is a possible explanation of the experimental results, and other experiments need to be done to verify these results.

2.2 Shear test with local thermal stimulation

Considering that under different stress conditions, the decomposition of hydrate and the deformation of the hydrate-bearing sediment will affect each other, in this section, the local thermal stimulation experiments of hydrate-bearing sediment (Tc) under different axial stress conditions was carried out.

2.2.1 Experimental procedure and conditions

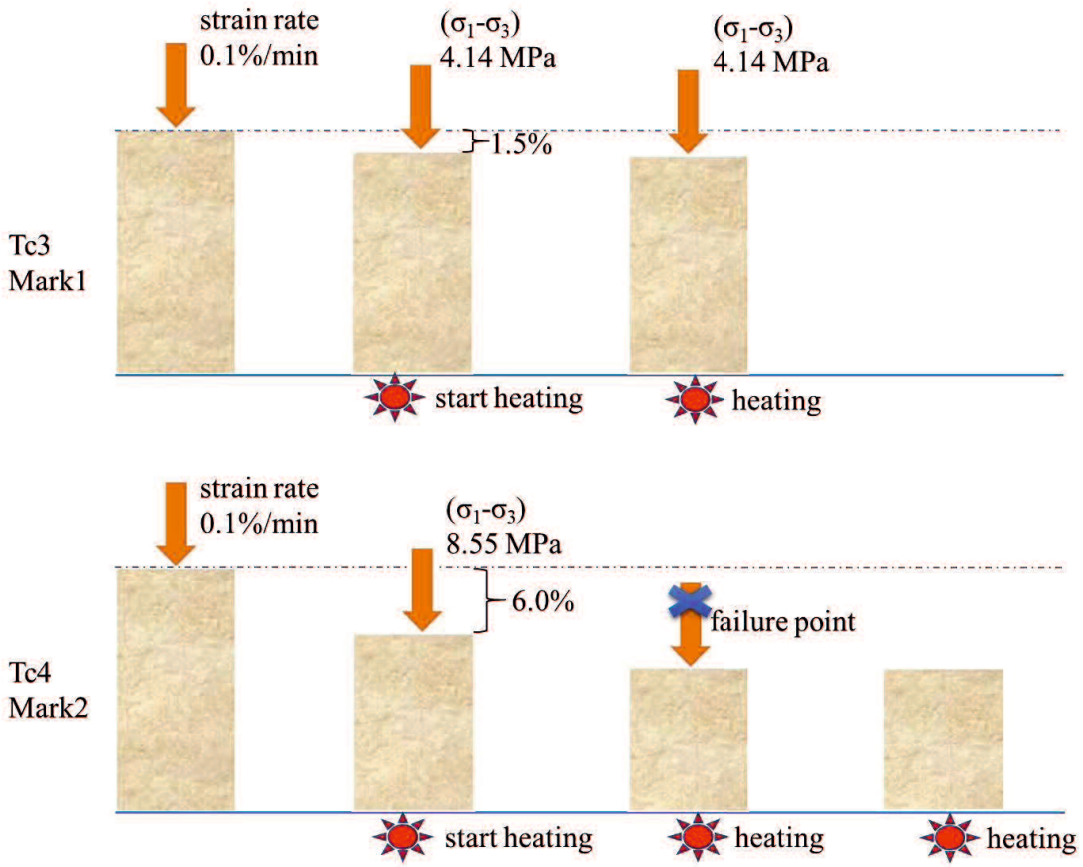

Figure 4-8. The schematic diagram of local thermal stimulation with axial loading.

The experiment method of Tc1 and Tc2 is already introduced in the previous section. In this section, two different kinds of experiments were carried out. Firstly, the plane strain shear experiment. The axial loading was carried out after the consolidation and the loading rate was set to 0.1 %/min.

Table 4-2. Experimental conditions.

Test name	Sand	Porosity (%)	MH saturation (%)	Shear process	Cell pressure (MPa)	Pore pressure (MPa)	Initial temperature (K)	Heating temperature (K)
Tc1	Tc	39.7	37.7	-	13.0	10.0	283.15	353.15
Tc2	Tc	40.2	0	-	13.0	10.0	283.15	353.15
Tc3	Tc	39.8	37.7	Mark1*	13.0	10.0	283.15	353.15
Tc4	Tc	39.5	32.3	Mark2*	13.0	10.0	283.15	353.15
Tc5	Tc	39.8	41.3	Mark3*	13.0	10.0	283.15	-
Tc6	Tc	39.6	0	Mark3*	13.0	10.0	283.15	-

* Mark1: loading (1.5%) → fixed value loading under heating
Mark2: loading (6%) → fixed value loading under heating until the specimen was destroyed→ heating without loading
Mark3: loading without heating

As for the local thermal stimulation tests with axial loading, the axial loading was also carried out after the consolidation and the loading rate was also set to 0.1 %/min. The schematic diagram of this experimental method is shown in **Figure 4-8**. As for Tc3, the specimen was first sheared to 1.5% of the axial strain, at this time the specimen had not yet reached the state of failure stress of the host sand sample (Tc) under the same conditions. Then, while maintaining a constant axial load, the thermal stimulus was applied simultaneously. The principal stress difference of Tc3 was maintained constant throughout the entire heating process. In the case of Tc4, the sample was firstly sheared to an axial strain of 6.0%. In this situation, the sample already passed the failure point of the host sand (Tc), but not reached the failure point of hydrate-bearing sediment (Tc). Similarly, the principal stress difference at this point was maintained and the heating process was carried out. To protect the instrument from damage, the loading system was shut down when significant cracks were observed in the specimen and the shear strength of the specimen was completely lost. Although, the heating was continued until the end of the experiment. The detailed experimental conditions are listed in **Table 4-2**.

2.2.2 Stress-strain and hydrate decomposition characteristics

Figure 4-9 shows the Stress-strain relationship of host sand (Tc) and hydrate-bearing sediments

(Tc) under different experimental conditions. Tc5 and Tc6 were the shear tests of hydrate-baring sediment (Tc) and host sand (Tc) without heating. It can be found that the hydrate-bearing sediment (Tc) has higher initial shear stiffness and shear strength. As for Tc3, after the initial shearing stage (red line), the axial strain of Tc3 reached about 1.5%, and the principal stress difference of Tc3 has not reached the peak strength of the pure sand sample (Tc6) under the same conditions. The green line represents the stress-strain results of Tc3 during heating. The initial shear test of Tc4 reached about 6% of the axial strain. At this time, the principal stress difference of Tc4 was higher than the peak strength of the pure sand sample (Tc6) and lower than that of the hydrate-bearing sediment (Tc5) under the same conditions. The orange line represents the stress-strain results of Tc4 during the heating process. When the axial strain of Tc4 reached about 12%, the principal stress difference of Tc4 suddenly dropped, which was caused by the failure of the sample. And then the axial loading system was turned off. During the heating process, the samples were in a drained and unsaturated condition due to the decomposition of hydrate. The instrument cannot measure accurate sample volume variations under this condition. Therefore, **Figure 4-9** do not show the volumetric strain of Tc3 and Tc4 during the heating process.

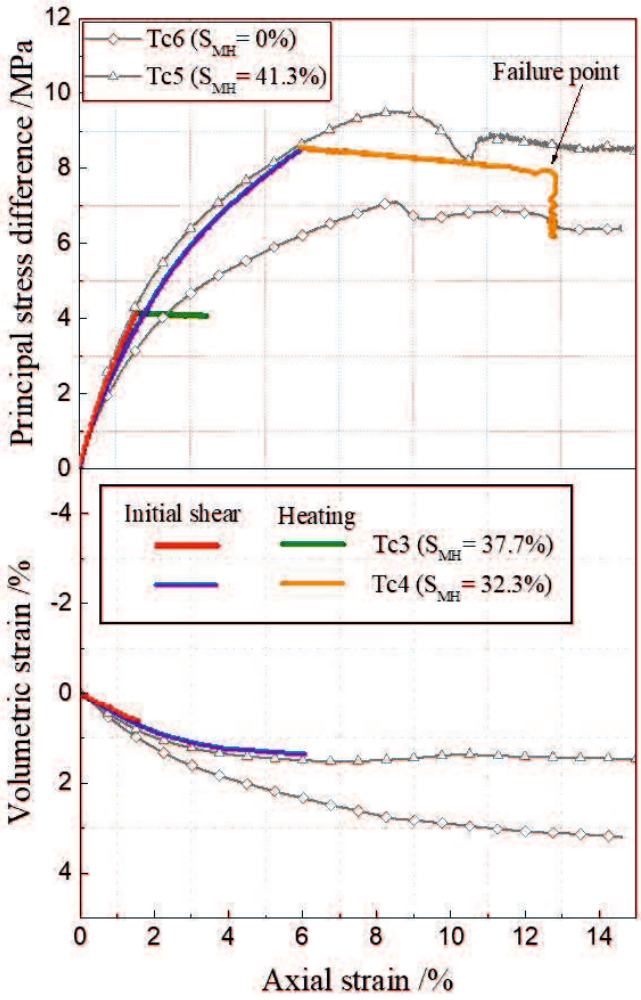

Figure 4-9. Stress-strain relationship of host sand (Tc) and hydrate-bearing sediments (Tc) under different experimental conditions.

Figure 4-10 shows the variation of the gas production factor (*GPR*) to time under local thermal stimulation without principal stress difference (Tc1), with a small principal stress difference (Tc3), and with a large principal stress difference (Tc4). It can be found that when the sample (Tc3) was only subjected to a small principal stress difference, the gas production efficiency was similar to the sample without a principal stress difference. Although the axial strain of the samples was different at the beginning of the heating test, the initial gas production factor is not affected by the previous shear process. For Tc4, the gas production factor a little decreased after the failure

of the sample. But for Tc1, when the gas production factor reached the same position (about 35%), the gas production factor also a little decreased, so it cannot be confirmed that the gas production factor was reduced here only due to the failure of the sample. When the gas production factor of Tc4 reached about 50%, a long plateau appeared, while Tc1 and Tc3 also have a slight plateau at the same position. The plateau duration of Tc3 was longer than Tc1, and Tc4 was the longest. It is hard to explain the reason for the long plateau of gas production factor in Tc4. But the initial gas production factor was not affected by the initial shear process can be confirmed. And during the heat process, the sample was damaged by high axial loading, the gas production factor was not be greatly reduced immediately.

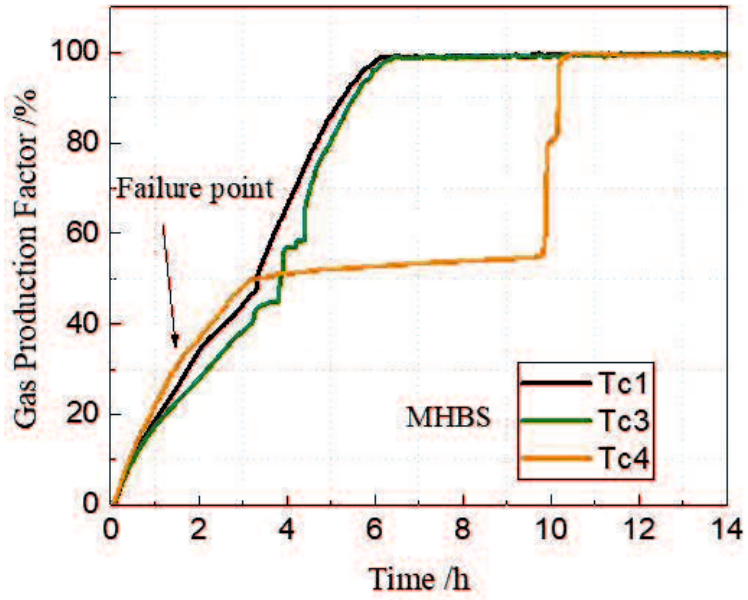

Figure 4-10. The *GPR* of hydrate-bearing sediments (Tc) under different axial loading conditions.

Figure 4-11 shows the changes in axial strain with the time of Tc3 and Tc4 during the heating process. Since Tc4 had a greater axial loading during heating, its axial strain increased faster than that of Tc3. Tc4 failed after the heating experiment was carried out for about 1.4 hours, and the axial strain increased sharply. On the contrary, the axial strain of Tc3 only increased a little during

the heating process.

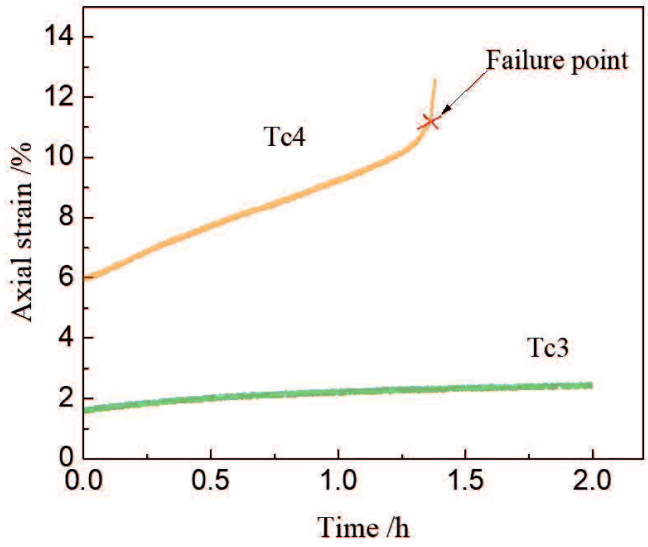

Figure 4-11. The changes in axial strain with the time of hydrate-bearing sediments (Tc) during the heating process.

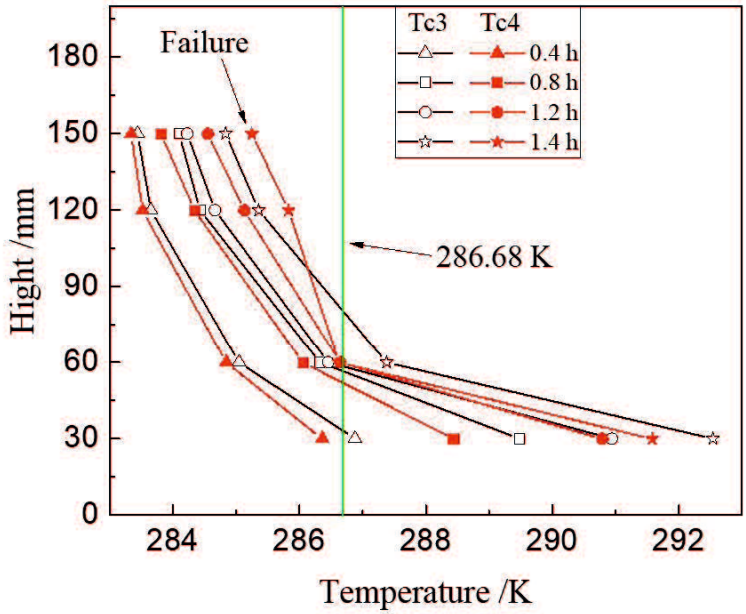

Figure 4-12. The *GPR* of hydrate-bearing sediments (Tc) under different axial loading conditions.

Figure 4-12 shows the temperature distribution inside Tc3 and Tc4 at different times during the

heating experiment. Tc4 was destroyed after being heated for 1.4 h. It was observed that the temperature at the lower part of Tc4 was much higher than 286.68 K, while the temperatures in the upper regions are smaller than 286.68 K after 1.4 h of the heating experiment. This implies that in this condition when the sample Tc4 was destroyed, only the hydrate in the lower part (about 40%) of the sample decomposed completely.

2.2.3 Local deformation characteristics

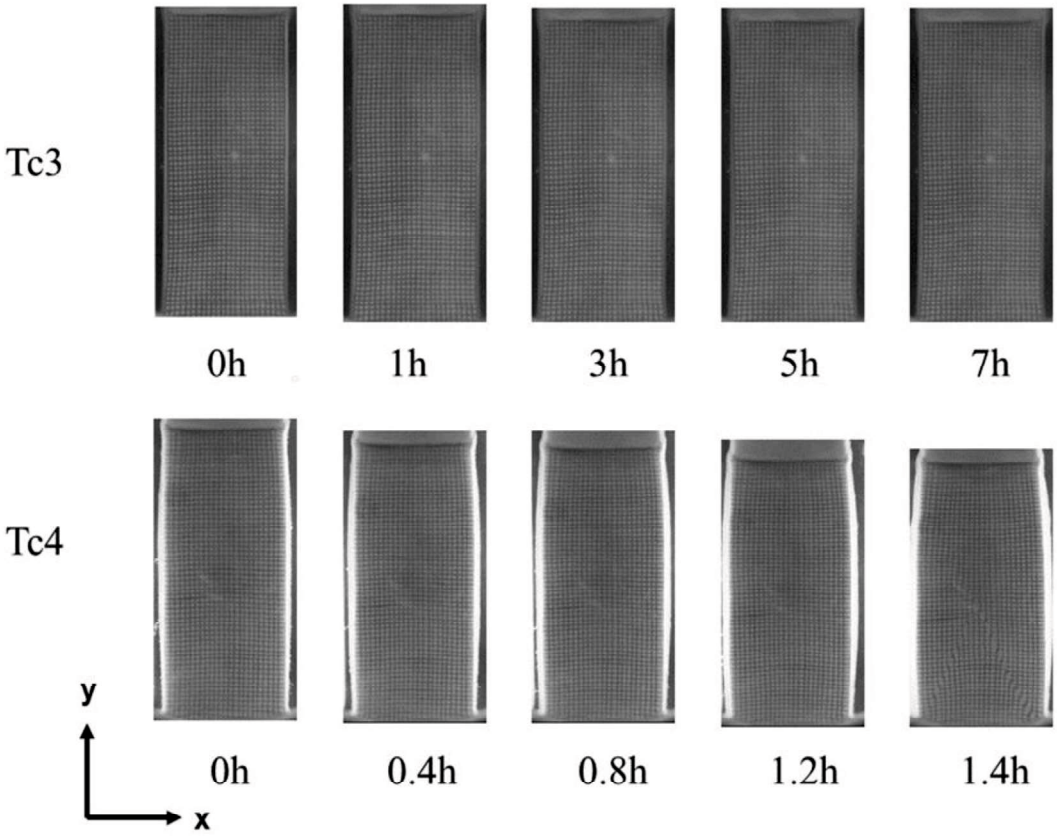

Figure 4-13. The appearance of deformation in samples Tc3 and Tc4 at different time points during the heat test.

The appearance of deformation in samples Tc3 and Tc4 at different time points during heating are shown in **Figure 4-13**. As for Tc3, no obvious local deformation was observed during the process of thermal stimulation. This is consistent with the fact that the axial deformation of Tc3 is very

small during the heating experiment. As for Tc4, after 1.4 hours of heating, obvious local deformation appeared in the middle and lower parts of the sample, and this implies that the sample was destroyed.

Figure 4-14 shows the contours of maximum shear strain and the volumetric strain of hydrate-bearing sediments (Tc3 and Tc4) during the thermal stimulation process. These results were based on PTV analysis. As the PTV analysis focused on the heat process, at the beginning of the analysis, the axial strains of Tc3 and Tc4 were about 1.5% and 6%, respectively. From **Figure 4-14** (a), in the case of Tc3, the maximum shear strain increment of the sample was small during the entire experiment due to the small principal stress difference. The decomposition of the hydrate did not cause concentrations of obvious local strain. The maximum shear strain of the Tc4 sample gradually increased with the decomposition of the hydrate as it withstood a larger principal stress difference. After 1.2 h of heating, the maximum shear strain at the lower and upper parts of the sample did not show any differences. With the further decomposition of the hydrate and the increase of the axial shear strain, the local shear strain concentration of Tc4 was significant, forming obvious shear bands. At this time, the gas production factor of Tc4 was about 35%, which implies that only the lower part of the hydrate was decomposed in Tc4. From **Figure 4-14** (b), the local volumetric expansion of Tc3 was not observable. On the contrary, the trend of local volumetric expansion of Tc4 gradually appeared. In summary, when the axial loading was large, preferential decomposition of the hydrate at the bottom of the sample occurred which caused a significant local concentration of the maximum shear strain and volume strain, destroying the sample.

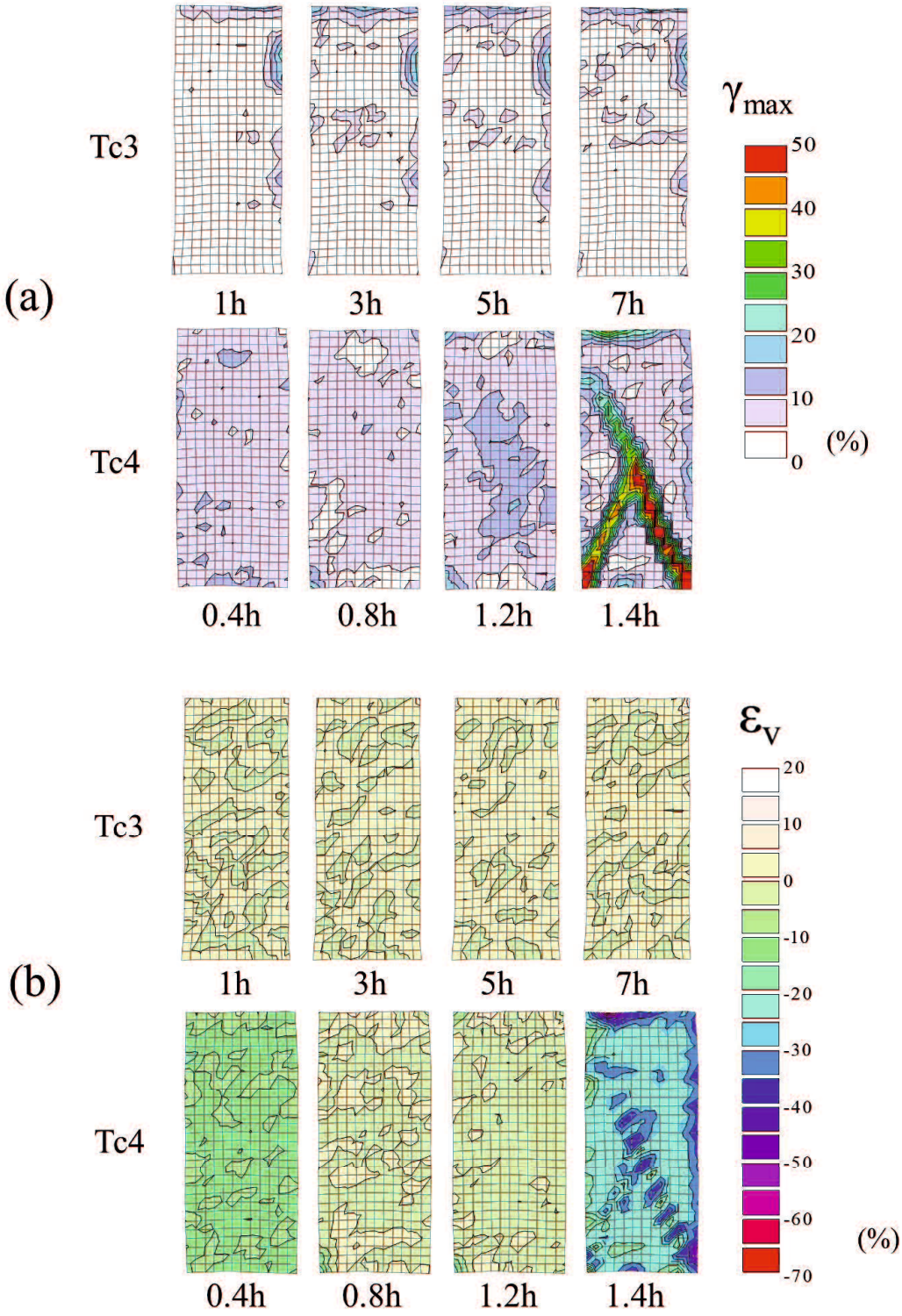

Figure 4-14. The appearance of deformation in samples Tc3 and Tc4 at different time points during thermal stimulation test.

2.3 Shear test with depressurization

2.3.1 Experimental apparatus

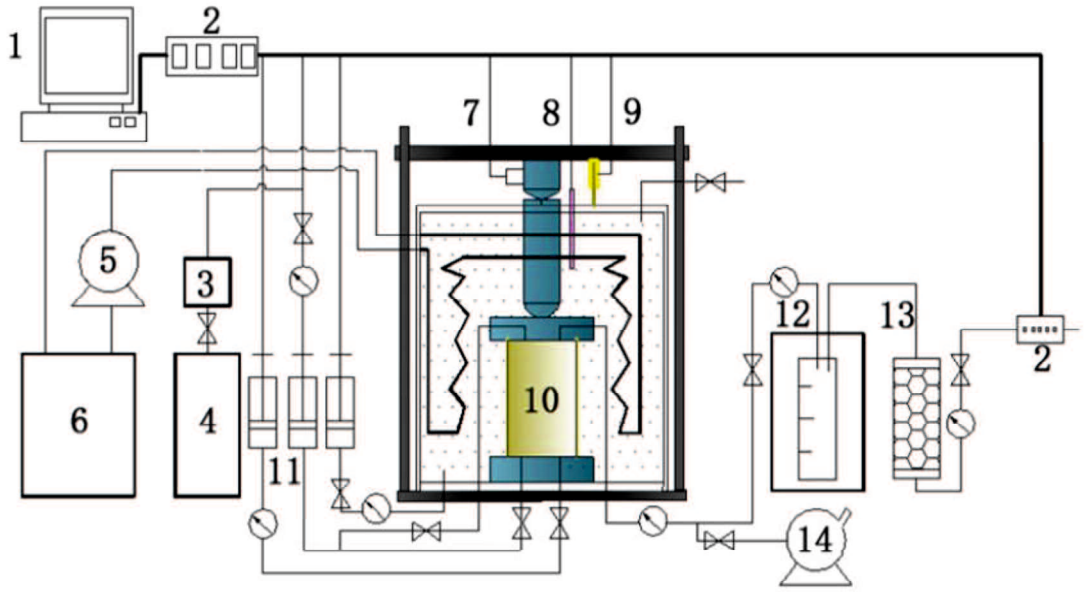

Figure 4-15. Schematic diagram of the experimental apparatus. (1) computer; (2) data acquisition; (3) buffer tank; (4) methane gas bottle; (5) water pump; (6) thermal control pump; (7) stress transducer; (8) temperature sensor; (9) displacement transducer; (10) specimen; (11) syringe pump; (12) gas-liquid separator; (13) desiccant; (14) vacuum pump.

A high-pressure and temperature-controlled triaxial shear test apparatus was used in this part to study the hydrate decomposition characteristics in sands during depressurization. The size of the specimen was 50 mm (diameter) × 100 mm (height). The loading system can supply a loading capacity of 250 kN. The pore pressure and cell pressure can be controlled up to 30 MPa with an accuracy of ±0.1 MPa by the syringe pump. The temperature was controlled by the liquid bath circulation system (Ethylene glycol as the medium) within 243.15 K–323.15 K, with an accuracy of ±0.5 K.

2.3.2 Experimental process and conditions.

Sands from the cores of the South China Sea were used here as the host sediments. **Figure 4-16** shows the grain size distribution of the sands from the South China Sea core and Tc. It can be found that the particle size distributions of these two host sands are very similar.

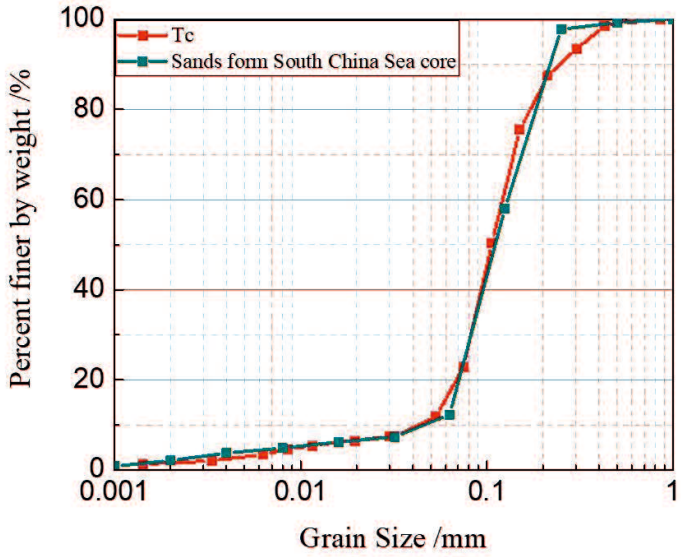

Figure 4-16. the grain size distribution of the sands from South China Sea core and Tc.

The preparation method of the methane hydrate-bearing sediments is the same as that described previously, and only the different shearing methods are introduced here.

As for the samples P1, P2, and M1, the shear tests were applied after the consolidation and the shear rate was 0.2%/min. During the shear test, the pore pressure was kept constant (drain test). The samples M2 and M3 were the shear tests with depressurization. **Figure 4-17** shows the schematic diagram of the shear test with depressurization. As for M2 and M3, after the consolidation, the sample was shear to 0.5% and 1.0% (axial strain) respectively with a shear rate of 0.2%/min and then reduced the pore pressure from 10 MPa to 3 MPa with a rate of about 0.5 MPa/min. After the pore pressure reached 3 MPa, kept the current pore pressure until the end of

the test. Throughout the shear test process, the shear rate of the sample was always maintained at 0.2 %/min. The detailed experimental conditions are shown in **Table 4-3**.

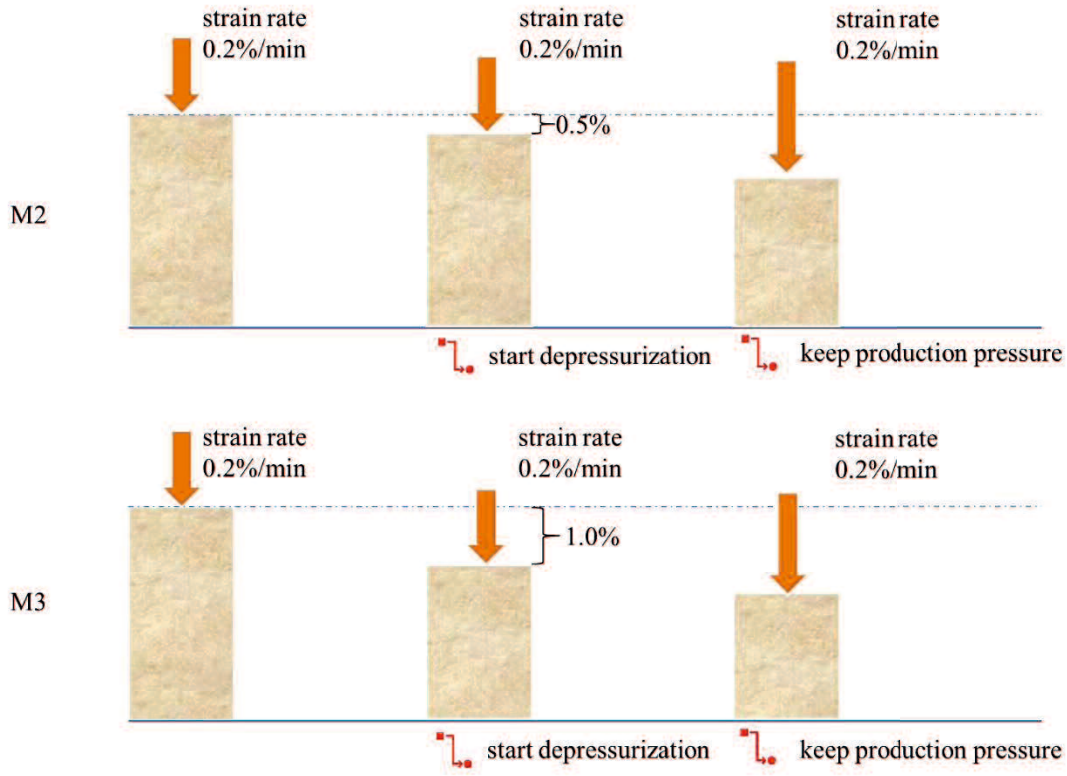

Figure 4-17. The schematic diagram of the shear test with depressurization.

Table 4-3. Experimental conditions.

Test name	Confining pressure (MPa)	Pore pressure (MPa)	Hydrate saturation (%)	Shear process	Temperature (K)	Shear rate (%/min)
P1	12	10	0	-	279.15	0.2
P2	12	3	0	-	279.15	0.2
M1	12	10	35.2	-	279.15	0.2
M2	12	10→3	33.8	Shear 0.5%→shear under dissociation	279.15	0.2
M3	12	10→3	33.8	Shear 1%→shear under dissociation	279.15	0.2

2.3.3 Experimental results.

Figure 4-18 shows the stress-strain, pore pressure, and hydrate saturation relationship of different samples during the shear test. Compared with host sand (P1), hydrate-bearing sediment (M1) has

higher stiffness and strength, which is consistent with the results of previous studies [Hyodo et al., 2013]. For the hydrate-bearing sediment (M1), when the axial strain rate reached about 2%, the principal stress difference of the sample reached the highest value and no longer changed. Since no obvious peak strength can be observed, the principal stress difference at which the axial strain rate of the specimen reaches 15% is taken as the peak strength $(\sigma_1-\sigma_3)_{max}$. For M2 and M3, through the initial shear stage, the samples reached different stress states. At the beginning of the depressurization, the principal stress difference of M2 was between the peak strength of host sand and hydrate-bearing sediment, while the principal stress difference of M3 is lower than the peak strength of host sand. The depressurization was carried out by reducing the pore pressure of the M2 and M3. It can be found that after the decrease of the pore pressure, the principal stress difference $(\sigma_1-\sigma_3)$ of M2 and M3 decreased immediately and then increased gradually until the end of the shear test. P2 was the host sand with N_2, under the high effective confining pressure, the stress-strain of P2 showed a significant strain hardening phenomenon. And the stress-strain behavior of M2 and M3 in the later stage of the shear process was similar to that of P2. The hydrate saturation of M2 and M3 was decreased the fastest in the initial stage of depressurization, and then the decrease rate gradually slowed down. Similarly, the volumetric compression of M2 and M3 were also the most significant in the initial stage of depressurization. Although the stress states of M2 and M3 were different during the depressurization, they exhibited the same ultimate volumetric strain. This means that under different stress states, the depressurization does not affect the ultimate volumetric strain of the sample. Previous studies have also found that in the initial stage of depressurization, the gas production rate and subsidence of the reservor were both the most significant [*Jin, G et al*., 2018].

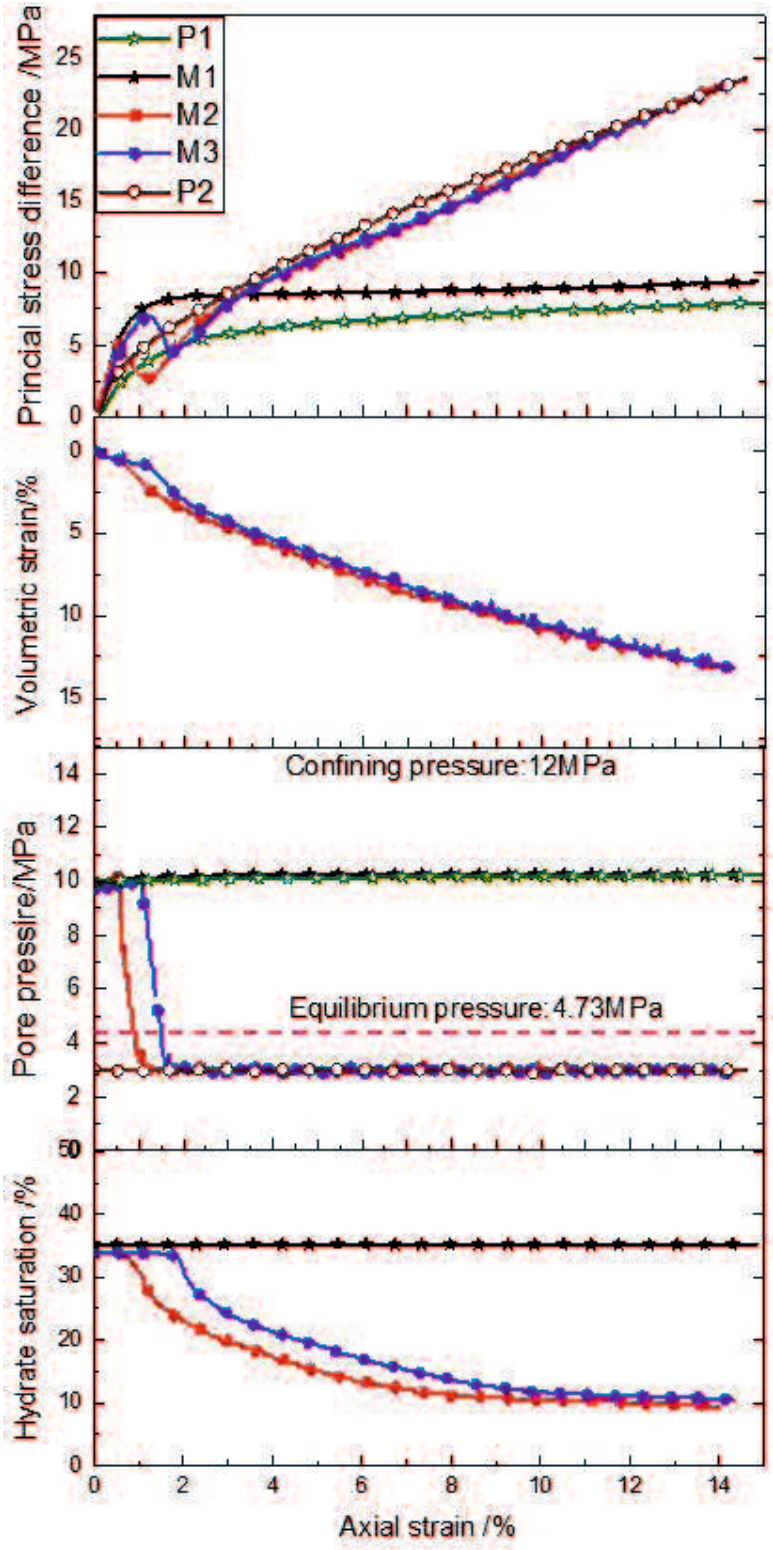

Figure 4-18. The stress-strain, pore pressure, and hydrate saturation relationship of different samples during the shear test.

The mechanism of the effect of hydrate decomposition on the stress-strain behavior of the hydrate-bearing sediment is shown in **Figure 4-19**. In the initial stage of shearing, the sand particles gradually became compact, and the hydrate in the pores was squeezed by the sand particles, which carried a part of the stress. When the hydrate was decomposed, due to the disappearance of the hydrate particles, the cementation between the sand particles and the bearing effect of the hydrate was quickly destroyed, resulting in a decrease in the principal stress difference and significant volumetric compression of the sample. After the sand particles have completed their rearrangement, the sample exhibited strain hardening behavior under high effective confining pressure. At this stage, the stress-strain behavior of hydrate-bearing sediments was the same as that of host sand under the same experimental conditions. This implies that the influence of hydrates on the stress-strain behavior of sediments can be ignored at this stage.

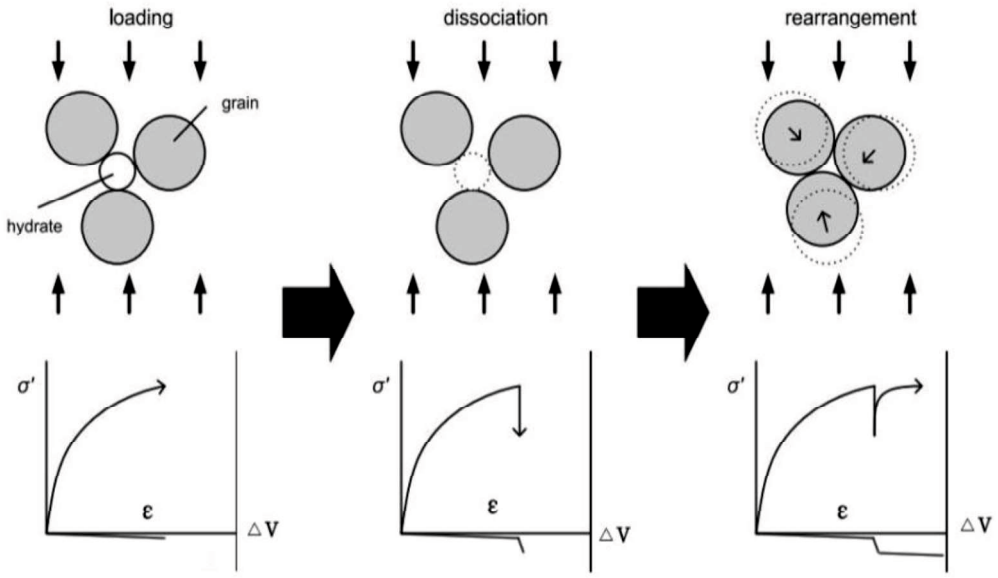

Figure 4-19. Mechanism of the effect of hydrate decomposition on the stress-strain behavior of the hydrate-bearing sediment [Uchida ., 2013; *Li et al*., 2018].

3. Conclusion

Chapter 4 firstly shown the decomposition characteristics of hydrate-bearing sediments with different fine particle contents under local thermal stimulation conditions. And then the decomposition and mechanical behavior of hydrate-bearing sediments under local thermal stimulation and depressurization has also been studied. Based on the experimental results, the following conclusions can be get:

(1) The heat transfer characteristics of the different host sands were similar under the water saturation conditions, despite having different particle size distributions and mineral compositions.

(2) Compared with the hydrate-bearing sediments containing fine particles (Tb and Tc), the hydrate-bearing sediments (Toyoura) had a more complicated hydrate decomposition process and lower overall gas production efficiency under local surface heating conditions.

(3) Different degrees of pre-shearing was not affected the initial gas production efficiency in hydrate-bearing sediments. Under the condition of high axial loading, the decomposition of hydrate caused the failure of hydrate-bearing sediments, but this was not immediately caused the decrease of gas production efficiency.

(4) When the axial loading was large, preferential decomposition of the hydrate at the bottom of the specimen occurred which caused a significant local concentration of the maximum shear strain and volume strain, destroying the specimen.

(5) In the initial stage of depressurization, the principal stress difference of the sample drops sharply due to the decomposition of the hydrate that cemented or carried the sand particles. The sample volumetric compression and gas production efficiency is the highest at this stage. After

the rearrangement of the sand particles, the sample exhibited significant strain hardening under high effective confining pressure. At this stage, the stress-strain behavior of the sample was similar to that of the host sand. Under different stress states, the gas production behavior and ultimate volumetric strain of the hydrate-bearing sediments are similar by depressurization.

4. Reference

Belosludov, V. R., Subbotin, O. S., Krupskii, D. S., Belosludov, R. V., Kawazoe, Y., and Kudoh, J. I. (2007). "Physical and chemical properties of gas hydrates: Theoretical aspects of energy storage application." *Materials Transactions*, 48(4), 704-710.doi:10.2320/matertrans.48.704

Falser, S., Uchida, S., Palmer, A. C., Soga, K., and Tan, T. S. (2012). "Increased gas production from hydrates by combining depressurization with heating of the wellbore." *Energy Fuels*, 26(10), 6259-6267.

Feng, Y., Chen, L., Suzuki, A., Kogawa, T., Okajima, J., Komiya, A., and Maruyama, S. (2019). "Numerical analysis of gas production from layered methane hydrate reservoirs by depressurization." *Energy*, 166, 1106-1119.

Jin, G., Lei, H., Xu, T., Xin, X., Yuan, Y., Xia, Y., and Juo, J. (2018). "Simulated geomechanical responses to marine methane hydrate recovery using horizontal wells in the Shenhu area, South China Sea." *Mar. Pet. Geol.*, 92, 424-436.

Jianliang, Y. (2020). "Main progress of the second gas hydrate trial production in the South China Sea." *Geology in China*, 47(3), 557-568

Kurihara, M., Sato, A., Ouchi, H., Narita, H., Masuda, Y., Saeki, T., and Fujii, T. (2009). "Prediction of gas productivity from eastern Nankai trough methane-hydrate reservoirs." *SPE Reservoir Evaluation and Engineering*, 12(3), 477-499.

Li, D., Wu, Q., Wang, Z., Lu, J., Liang, D., and Li, X. (2018). "Tri-axial shear tests on hydrate-bearing sediments during hydrate dissociation with depressurization." *Energies*, 11(7).

Liu, Y., Bai, Y., Xia, Z., and Hou, J. (2018). "Parameter optimization of Depressurization−to−Hot−Water−Flooding in heterogeneous hydrate bearing layers based on the particle swarm optimization algorithm." *Journal of Natural Gas Science and Engineering*, 53, 403-415.

Moridis, G. J., Collett, T. S., Boswell, R., Kurihara, M., Reagan, M. T., Koh, C., and Sloan, E. D. (2009). "Toward production from gas hydrates: Current status, assessment of resources, and simulation-based evaluation of technology and potential." *SPE Reservoir Evaluation and Engineering*, 12(5), 745-771.

Moridis, G. J., Collett, T. S., Pooladi-Darvish, M., Hancock, S., Santamarina, C., Boswel, R., Kneafsey, T., Rutqvist, J., Kowalsky, M. B., Reagan, M. T., Sloan, E. D., Sum, A. K., and Koh, C. A. (2011). "Challenges, uncertainties, and issues facing gas production from gas-hydrate deposits." *SPE Reservoir Evaluation and Engineering*, 14(1), 76-112.

Shun, U. Numerical Investigation of Geomechanical Behaviour of Hydrate-Bearing Sediments. Ph.D. Thesis, University of Cambridge, Cambridge, UK, 2013.

Walsh, M. R., Hancock, S. H., Wilson, S. J., Patil, S. L., Moridis, G. J., Boswell, R., Collett, T. S., Koh, C. A., and Sloan, E. D. (2009). "Preliminary report on the commercial viability of gas production from natural gas hydrates." *Energy Economics*, 31(5), 815-823.

Yu, T., Guan, G., Abudula, A., Yoshida, A., Wang, D., and Song, Y. (2019). "Heat-assisted production strategy for oceanic methane hydrate development in the Nankai Trough, Japan." *J. Pet. Sci. Eng.*, 174, 649-662.

Chapter 5 Summary and Future work

1. Summary of thesis

Natural gas hydrate (NGH) is a promising energy resource. The ultimate goal of this thesis is to provide an experimental basis for the realization of safe and efficient exploitation of NGH.

Firstly, before realizing the safe and efficient exploitation of NGH, it is necessary to study the influence mechanism of different factors on the mechanical properties of hydrate-bearing sediments by laboratory mechanical experiments. And then establish the constitutive model of the stress-strain relationship of hydrate-bearing sediments. Finally, according to different exploitation conditions, predict the changes in the mechanical properties of the NGH reservoir during the exploitation process to ensure the safety of exploitation. Sufficient laboratory research is the foundation to ensure the safe exploitation of NGH. Sediments have various stress conditions in the NGH reservoir. However, most of the current studies about the mechanical properties of hydrate-bearing sediments under general stress conditions and then established corresponding constitutive models. The failure of hydrate-bearing sediments under plane strain conditions is always accompanied by significant local strain and eventually formed a clear shear band. Even under the same experimental conditions, the stress-strain relationship of hydrate-bearing sediments is different in the triaxial shear and plane strain shear experiments. Therefore, studying the development characteristics of the shear band is helpful to understand the failure mode of hydrate-bearing sediments under plane strain conditions.

In chapter 2, through Particle Tracking Velocimetry (PTV) technology, a method of measuring

the angle and thickness of the shear band has been applied. The experiment measured the development process of the angle and thickness of the shear band of hydrate-bearing sediments at different shear stages. Experimental results show that clear shear bands gradually formed after the sample reached its peak strength. The shear angle first increased, then remained constant when the sample reached the residual strength, and finally decreased slightly. The thickness of the shear band narrowed first and slightly widened when the sample reached the residual strength. The change of the angle and thickness of the shear band is related to the fact that the specimen is not completely rigid during the shearing process.

Secondly, it is also necessary to study some important factors under plane strain conditions, which can significantly influence the mechanical properties of hydrate-bearing sediment. Shear rate dependence is a time-dependent property of materials. Introducing the time parameter into the study of the mechanical properties of hydrate-bearing sediments, on the one hand, is conducive to accurately predicting the long-term stress-strain behavior of the reservoir, on the other hand, it can establish the contraction between the mechanical properties of hydrate sediments and the decomposition rate of hydrates in the future. However, there are only a few related studies focused on general stress conditions have been reported. It is necessary to study the shear rate dependence of hydrate sediments under plane strain conditions.

In chapter 3, the shear rate-dependent characteristics of hydrate-bearing sediments have been studied. After confirming that hydrate-bearing sediment also has shear rate-dependent characteristics under plane strain conditions, three different shear rates have been selected to study the effects of hydrate saturation and fines content on shear rate dependence. The research results will help to introduce time parameters into the constitutive model of hydrate sediments in the future, and then achieve long-term accurate prediction of the mechanical characteristics of the

NGH reservoir.

Finally, understanding the decomposition characteristics of hydrates in the sand is the basis for developing methods to improve gas production efficiency.

In Chapter 4, due to the differences in the content of fine particles in different reservoirs, the effect of the content of fine particles on the decomposition characteristics of hydrates in the sand under local thermal stimulation conditions has been studied firstly. On the other hand, sediments located in different positions of the reservoir may be in different stress states due to the early wellbore construction. Thermal stimulation and depressurization operations cause the decomposition of hydrates, which will also affect the stress-strain behavior of sediments, and the deformation of sediments will in turn affect the decomposition characteristics of hydrates. In other words, the mechanical properties of the reservoir are closely related to the decomposition properties of hydrates. Understanding the mechanics of hydrate-bearing sediments and the decomposition characteristics of hydrates under different stress states is also very important to accurately predict the mechanical behavior of the reservoir during the exploitation process. In the second part of Chapter 4, under different stress conditions, the stress-strain relationship of hydrate-bearing sediments and the decomposition characteristics of hydrates during local thermal stimulation and depressurization have been studied. The experimental results are helpful to understand the interaction mechanism between the decomposition of hydrates and the stress-strain behavior of sediments under different conditions.

In general, the results of this study are of great significance for establishing or calibrating a constitutive model that can accurately predict the geological behavior of NGH reservoirs during exploitation, and ultimately ensure the safety of hydrate exploitation.

2. Future work

The experimental results in this thesis will provide original reference data for establishing a constitutive model with time dependence and hydrate decomposition characteristics suitable for plane strain conditions. As the shear rate dependence and creep characteristics (under constant axial stress, the strain characteristics of the sample) are essentially the performance of the material's time dependence properties. The stress-strain relationship of hydrate-bearing sediments and the decomposition characteristics of hydrates can be unified by time parameters. Under plane strain conditions, the stress-strain relationship after the sample reaches the peak strength can be linked to the development of the sample's shear band. In this way, the prediction of the residual strength and volumetric strain of the specimen can be optimized by the constitutive model. Due to the inability to observe the distribution and the movement of hydrates within the samples during shearing or decomposition experiments, the reasons for many experimental results cannot be determined, which makes it difficult to understand the impact of hydrates on the mechanical behavior of sediments. In the future, related microscopic experiments should be done to study the essential reasons for the influence of hydrates on the mechanical behavior of sediments.

Acknowledgment

During the preparation of this thesis, I received enthusiastic help from many people. I would like to express my sincere thanks for all of them. I also want to thank the China Scholarship Council (CSC 201804910603) for the scholarship provided, which relieved me of the financial pressure of studying abroad.

First of all, I would like to thank my Ph.D. supervisor Associate Professor Yoshimoto. Whether it is the topic selection of the thesis, the operation of the experiment, or the revision of the dissertation manuscript, he has provided me with great help. He is always smiling and enthusiastic to help me deal with the difficulties in life and study. So even though I am abroad, I never feel alone in Japan. In every discussion of experimental results, he could always make meaningful suggestions, which greatly improved the efficiency of my experimental research. When I encountered difficulties, he always actively helped me find solutions and encouraged me to treat all failures with optimism. I could not finish this thesis without his patient and kind help.

Secondly, I want to express my heartfelt thanks to Professors Hyodo and Nakata. They are always willing to spend time listening to my conditions, and then give me a lot of comments and suggestions. They have made brilliant achievements in their fields, but they are still willing to patiently guide my research. They have greatly broadened my horizon and enriched my knowledge in my study. The same thanks to Associate Professors Mori, Md.Azizul Moqsud and Assistant Professor Kajiyama. They can always point out the problems in my research and give very good suggestions every time. The smooth progress of the research is inseparable from their selfless help.

Also, I would like to express my sincere gratitude to Professors Aso, Suzuki, Nakata, and Associate Professor Nakashima. Thank them for taking the time to read my graduation thesis and give professional guidance during their busy hours. It is with their guidance that my doctoral dissertation can better show the results of my research.

And then I also want to thank the friends in the research team for their enthusiasm and kindness, which made my life extremely happy in Japan. My gratitude would be expressed to Nakashima, Jialin Xu, Shuyang Guo, Pengyu Tian, Taue, Endo, Komatubara, Fujita, Nakano, Koga, and Bat-ochir Tumurdulam.

Finally, I would like to express my thanks to my beloved family, especially my parents, who always give me the greatest support and understanding. Their love and care are the greatest fortunes of my life.

Thanks again for everyone's help.

WU QI

2021.09